AN ABSTRACT OF THE THESIS OF

Dong-Kyu Lee for the Doctor of Philosophy

in Oceanography presented on May 4, 1987

Title: The Linear and Non-linear Baroclinic Instability in the Eastern North Pacific

Redacted for privacy

Abstract approved : P. P. Niiler

Using a linear quasi-geostrophic model of large scale spiraling flow and vertical density gradient in the eastern North Pacific, we evaluate the complex dispersion relationships for quasi-geostrophic waves. Our calculations indicate that the geostrophic circulation of the eastern North Pacific can locally convert potential energy to mesoscale kinetic energy on a scale comparable to the observed space and time scale and should be a source of eddy energy, distant from the eddies spawned by the Kuroshio and near the topographic features. But the local growth rates by linear stability analysis do not relate to the observed features of eddy kinetic energy in the eastern ocean; eddy kinetic energy increases to the south and has a maximum in the subtropical region.

The non-linear baroclinic instability is analyzed using a three-layer quasi-geostrophic numerical model. Three experiments with different idealized initial mean flow are performed. Local energetics are calculated to highlight the difference between the southward return flow and westward return flow regions. It is found that the boundary flux of mean to eddy kinetic energy conversion is the main differences between two regions: it is large in the westward return flow region but is small in the southward return flow region. Two waves with different characteristics are found: the short waves (periods of 120 days), that propagate to the west and form several wave trains parallel to the southern boundary, and the long waves (periods of 200 days), that propagate to the south-west. These two waves are remarkably similar to the

measurements of open ocean eddies at 28° N and 152° W. It is shown that there are high eddy activities in the southward return flow regions by influxes of eddies from other areas, but the southward return flow region is vacant in eddies by outflows of the westward and south-westward propagating waves.

The Linear and Non-linear Baroclinic Instability in the Eastern North Pacific

by

Dong-Kyu Lee

A THESIS

submitted to

Oregon State University

in partial fulfillment of
the requirements for the
degree of

Doctor of Philosophy

completed May 4, 1987

commencement June 1987

APPROVED:

Redacted for privacy

Professor of Oceanography
in charge of major

Redacted for privacy

Dean of School of Oceanography

Redacted for privacy

Dean of Graduate School

Date thesis is presented May 4, 1987

ACKNOWLEDGEMENT

I thank my major professor, Dr. Peter Niiler, for giving me the novel ideas and continuous encouragements during my uneven graduate school years. He supported me well enough that I was able to survive despite of the costly living in La Jolla.

In-Kyeong has been a lovely and faithfull wife throughout my ordeal. Without her love and trust I would never have been able to maintain my strength.

I always feel my mother's warmth and love behind me. She taught me love of God and positive thinking. My mother-in-law always pray for me and my wife, and she visited us from Korea to help the first three months of our two little girls in spite of her poor health.

I thank to Anne White and Judy Illeman for helping my English. Bob and Shirley Kingsbury provided me a warmth of home away from my home country in my first year in the United State.

Table of Contents

List of Figures

Chapter II

Chapter III

List of Tables

Chapter II

Chapter III

The Linear and Non-linear Baroclinic instability in the Eastern North Pacific

Chapter I

Introduction

1. Introduction

It was shown by many investigators (for example, Gill *et al.*, 1974, Haidvogel and Holland, 1978) that the eddies are generated by the baroclinic instability in the regions of strong mean vertical shear. But the recent direct measurements (McNally *et al.*, 1983, Niiler and Reynolds, 1984 and Niiler *et al.*, 1987) reveal that eddies are flourishing in the regions of weak mean current, i.e. in the eastern ocean basin. And they also show that the eddy kinetic energy increases to the south and has maximum in the subtropical area.

A theoretical approaches toward understanding the spawning of mid-ocean eddies were attempted by Schulman (1967), Robinson *et al.* (1974), Gill *et al.* (1974) and Kang *et al.* (1982). They amply demonstrated the possibility of converting potential energy into kinetic energy by mid-ocean baroclinic instability. But they did not show as much detail for the realism of observed large scale flows for a particular ocean basin as to allow comparison with observations of eddy fields.

In Chapter II, the complex dispersion relation of a linear three-level quasi-geostrophic model with a non-zonal flow and lateral friction is computed and the properties of these waves are examined. The linear stability analyses of the continuous model (34-level model) are also presented for comparison with the three-level results. After examining the relationships between three-level and 34-level model results, it is found that while a three-level model can realistically model two gravest stable baroclinic Rossby waves over a broad area of the eastern ocean basin, the wave characteristics are quite different from each other.

But the linear growth rates computed from the linear stability analysis do not match with the observed eddy kinetic energy distribution. For example the local growth rate of the subpolar regions is the same as that of subtropical region, but the eddy kinetic energy of the subpolar region is only one-third of that of subtropical region at depth of 180 m (Niiler *et al.*, 1987).

The non-linear stability analysis is examined in Chapter III using a three-layer eddy resolving general circulation model (EGCM). The EGCMs by Holland and Lin (1975), Holland (1978) and Robinson *et al.* (1977) are only focused on the eddies generated by the western boundary current because of the limits of the model size. The first numerical study which shows a band of high eddy kinetic energy on the westward return flow of the subtropical gyre was done by Cox (1985) using a 18-level primitive equation model. The characteristics of the subtropical eddies generated by his model agree well with observation except that the periods are shorter than the observed periods due to the large model mean flow (4.1 cm/s) compared to the observed mean flow (1 - 2 cm/s).

In this thesis, the three-layer quasi-geostrophic model focused on the eastern basin which is far from the strong western boundary current is studied using a strong western viscosity area. Each layer except the bottom layer is forced to maintain a devised initial mean circulation in the absence of meso-scale motion. The waves are generated by adding a small perturbation to the initial stream function. Thus the forcing function is for maintaining the basic circulation rather than for spinning up the gyre from a motionless ocean.

Three experiments are performed. The first experiment uses the mean flow of 1 - 2 cm/s and the second experiment uses the strong mean flow (3 - 4 cm/s) for examining the effects of the growth rates. To show the effects of the south-westward propagating waves more qualitatively, two long and thin box (north-southward and east-westward) experiments are presented.

Chapter II

The Local Baroclinic Instability of Geostrophic Spirals in the Eastern North Pacific.

by

Dong-Kyu Lee
College of Oceanography
Oregon State University
Corvallis, OR 97331

Pearn P. Niiler
Scripps Institution of Oceanography
La Jolla, CA 92093

1. Introduction

Using satellite tracked drifting buoys, McNally *et al.* (1983) showed that the kinetic energy of the eastern north Pacific is about one half to one third of the western basins; the weakest field is found in the subpolar Northeast Pacific. Niiler and Reynolds (1984) also showed, using drifting buoy data, that there is an increase of eddy kinetic energy from subpolar to subtropical areas in the Northeast Pacific, especially west of 160°W. Recently acquired two year-long moored current meter data in the eastern North Pacific at 28°N, 152° W and 40°N, 152°W reveal a similar picture throughout the water column from 100m to 4000m. For example, the eddy kinetic energy per unit volume which has a period of 1-100 days is 78.5 cm^2/s^2 at a depth of 69m at 28°N, however it is 15.6 cm^2/s^2 at 80m in the same period band at 42°N and the time scale of eddies are 10 - 15 days. The above three direct kinetic energy measurements are shown on Figure 1.

Several questions about observed mid-ocean eddies now arise. Why is the mid-ocean eddy field quite different in various regions? What are the dynamics which generate these eddies and how do they grow to finite amplitude? Are vertical structures also different? Are the different mean geostrophic flows also reflected in eddy fields?

A theoretical approach toward understanding the spawning of mid-ocean eddies was first attempted by Schulman (1967) who computed the stability of a meridionally overturning cell in a constant density gradient fluid with typical ocean parameters of mean flow; he found unstable waves with a one year growth rate and wave length of several hundred kilometers. But these waves (periods of 2-3 years) are of much longer time scale compared with observed ocean mesoscale time scales. Robinson and McWilliams (1974) computed the complex dispersion diagram of a two-layer quasi-geostrophic shear including bottom topography and β-effects. When they evaluated this diagram in a shear of 5 cm/s (observed eastern north Pacific shear are 1 - 2 cm/s), they found instabilities characterized by a two month growth rate and a 200 - 300 Km wave length. Gill, Green and Simmons (1974) used

continuous vertical profiles of density and zonal velocity, typical of the North-Equatorial Current area in the Atlantic, to compute the quasi-geostrophic unstable wave parameters. They found most unstable waves with growth rates of a few months and wave lengths of a few hundred kilometers. Their computations, however, ignore the fact that the north equatorial current shear in the Atlantic has a strong meridional component above 200m (Keffer and Niiler, 1982). Kang and Magaard (1979) solved quasi-geostrophic vorticity equations using the observed continuous density profile and corresponding models of geostrophic zonal shear of several Western North Pacific regions. They found the most unstable waves with a 1.1 year growth rate (periods of 395 days and 157 Km wave length) at $30°N$ latitude, near the gyre center. Kang, Price and Magaard (1982) were the first to compute waves on a spiraling shear instead of a zonal shear, and applied their limited analysis to the California Current region ($35°\mathrm{N}, 132.5°\mathrm{W}$). They only discussed a single stable wave mode. In summary, a variety of linear instability computations have been done for mid-ocean circulation patterns, but not with as much detail for the realism of observed large scale flows for a particular ocean basin as to allow comparison with observations of eddy fields in detail. However, the possibility of converting potential energy to kinetic energy by mid-ocean baroclinic instability has already been amply demonstrated.

Holland and Lin (1975) and Holland (1978) demonstrated how these eddies can be generated and grow to finite amplitude, and they have constructed equilibrium energetics using a two-layer eddy-resolving numerical model. However, their two-layer model was not sufficient to resolve the important spiraling nature of the mid-ocean, and the small basin size made their model more applicable to the western boundary current eddy problem. Numerical experiments with higher vertical resolution by Robinson *et al.* (1977) also used a small basin size which was not sufficient to model the eastern north Pacific, but did reveal instabilities in the analogue to the North Equatorial Current. Schmitz and Holland (1982) successfully compared the observed eddy kinetic energy in the bottom layers of Gulf stream

area (near the western boundary) with that calculated from the numerical model done by Holland (1978), but they were unsuccessful in reproducing the eddy kinetic energy patterns observed south of 20°N or in the upper layers. Using a primitive equation numerical model, Cox (1985) showed the development of eddies with a 400 km wavelength and 50 days period in the North Equatorial Current region. But their wave period is too short compared to the observation (100 days), and also the horizontal resolution (44 km zonally) and model size (6600 km from the western boundary) are not sufficient to describe the eastern North Pacific eddies with wave lengths of 50 - 200 km. All above numerical models have lateral friction for computational stability.

In this paper, we first compute the complex dispersion relationship of a three-level quasi-geostrophic model with a non-zonal flow and lateral friction ($A_H = 5 \times 10^6 cm^2/s^2$) and examine the properities of these waves with a three-level shear model of the northeast Pacific. The reasons for initially selecting a three-level model are: i) According to the computed geostrophic mean flow, meridional velocities are of the same magnitude as zonal velocities, so we cannot simply ignore the spiraling mean flow. A three-level model is the simplest one which can represent a spiral. ii) Schmitz and Holland (1982) showed in their comparison study of observed and modeled Gulf Stream mesoscale energetics that a two-layer model was not sufficient to obtain appropriate observed shear parameters (for example, to obtain a sufficient large Rossby number, defined by Holland (1978), $R_o = \pi\tau_o/H_1\beta^2L^3$, a very small upper layer depth is required). iii) We wish to compare the vertical resolution criterion of resolving equivalent depths or Rossby radii suggested by Flierl(1978) by computing complex diagrams of three-level vs 34-level model of eastern Pacific. In both models the instabilities associated with meridional shear should be manifest. iv) Three-level results are presented here because coarse vertical resolution numerical models are often used for studying the mid-ocean eddy field and this calculation will form the basis of comparison

of the linear instabilities in the realistic three-level setting. After the examining the relationships between three-level and 34-level models, we found that while a three-level model can realistically model two gravest stable baroclinic Rossby waves over a broad area of the eastern Pacific, at least a six-level model is required for resolving the spiraling shear.

The baroclinic instability problem we discuss is not new in principle, but should be applicable for mimicking the reality of the Northeast Pacific.

2. Equations

2.1 Governing equations

The equations for quasi-geostrophic perturbations on a two dimensional flow pattern are found in Pedlosky (1979) and Kang *et al.* (1982). Following their derivation, the linearized quasi-geostrophic potential vorticity equation and their boundary conditions are,

$$(\vec{U}\cdot\vec{K}-\sigma)\left\{\frac{d}{dz}\left(\frac{f^2}{N^2}\frac{d\phi}{dz}\right)-K^2\phi\right\}+\left\{\beta k-k\frac{d}{dz}\left(\frac{f^2}{N^2}\frac{d\bar{U}}{dz}\right)-l\frac{d}{dz}\left(\frac{f^2}{N^2}\frac{d\bar{V}}{dz}\right)\right\}\phi=-iA_HK^4\phi, \tag{2.1}$$

$$(\vec{U}\cdot\vec{K}-\sigma)\frac{d\phi}{dz}-\left(k\frac{d\bar{U}}{dz}+l\frac{d\bar{V}}{dz}\right)\phi=0 \text{ at } z=0 \text{ and } z=-H. \tag{2.2}$$

where the mean horizontal velocity vector $\vec{U}=(\bar{U},\bar{V})$, the wave number vector $\vec{K}=(k,l)$, N is the Brünt-Väisälä frequency, f is the Coriolis parameter, $\beta=\partial f/\partial y$ and A_H is the horizontal eddy viscosity coefficient. The perturbation pressure from the basic state is

$$\varphi'(x,y,z,t)=Re\left\{\phi(z)exp(i(kx+ly-\sigma t))\right\}, \tag{2.3}$$

and H is the bottom depth. Using variables

$$\left.\begin{aligned}\tilde{\beta}&=\frac{\beta k}{K},\\ \tilde{U}&=\frac{k\bar{U}+l\bar{V}}{K},\\ c&=\frac{\sigma}{K}.\end{aligned}\right\} \tag{2.4}$$

We can rewrite Eqs.(2.1) and (2.2) as

$$(\tilde{U}-c)\left\{\frac{d}{dz}(\frac{f^2}{N^2}\frac{d\phi}{dz})-K^2\phi\right\} + \left\{\tilde{\beta}-\frac{d}{dz}(\frac{f^2}{N^2}\frac{d\tilde{U}}{dz})\right\}\phi = -iA_H K^3\phi \qquad (2.5)$$

and

$$(\tilde{U}-c)\frac{d\phi}{dz}-\frac{d\tilde{U}}{dz}\phi = 0 \quad \text{at} \quad z=0 \quad \text{and} \quad z=-H. \qquad (2.6)$$

There are certain range of allowable phase speeds and growth rates for the spiral flow. An estimate for the semi-circle in the complex c plane for inviscid flow can be obtained directly using Pedlosky's (1979, pp447 - 451) formulation simply by substituting $\tilde{U}$ for U and $\tilde{\beta}$ for β defined by Equation (2.4) and integrate from bottom to surface.

$$\left(\frac{\tilde{U}_{max}-\tilde{U}_{min}}{2}\right)^2+\frac{|\tilde{\beta}|}{K^2+(\frac{f\pi}{NH})^2}\left(\frac{\tilde{U}_{max}-\tilde{U}_{min}}{2}\right)\geq\left(c_r-\frac{\tilde{U}_{max}+\tilde{U}_{min}}{2}\right)^2+c_i^2. \qquad (2.7)$$

Here we use $|\tilde{\beta}|$ because $\tilde{\beta}$ can be a negative value depending upon wave numbers. If c is real, then

$$c_r < \tilde{U}_{min} \quad \text{or} \quad c_r > \tilde{U}_{max} \qquad (2.8)$$

Expressions (2.7) and (2.8) will be used to distinguish physically realizable solutions from numerical solutions in Section 7. Condition (2.8) is strictly applicable only for continuous models. In any specific level model, it is usually possible to find a C_r where for a specific resolution, i, condition (2.8) is violated and $(\tilde{U}(z_i)-c_r)$ does not vanish. However, as the number of levels is increased, such solutions can become increasingly singular. Therefore, as we have not found a case where $(\tilde{U}(z_i)-c_r)$ vanishes together with $\left\{\tilde{\beta}-\frac{d}{dz}(\frac{f^2}{N^2}\frac{d\tilde{U}}{dz})\right\}_i$ at some level, i, we consider all level solutions unphysical where c_r lies within the range of $\tilde{U}(z_i)$. (See Pedlosky, 1979, for an analytical exception). Eady's model, which has two analytical solutions, was used in testing this selection criterion with n-level model and comparing n-numerical solutions with the two analytical solutions. A very effective screening of the correct physical solutions resulted.

2.2 N-level model equations

The finite-difference approximations of terms in Equation (2.2) are

$$\frac{d}{dz}\left(\frac{f^2}{N^2}\frac{d\phi}{dz}\right) = \frac{f^2\rho_o}{gd_i}\left(\frac{\phi_{i+1}-\phi_i}{\rho_{i+1}-\rho_i} - \frac{\phi_i-\phi_{i-1}}{\rho_i-\rho_{i-1}}\right), \tag{2.9}$$

and

$$\frac{d}{dz}\left(\frac{f^2}{N^2}\frac{d\tilde{U}}{dz}\right) = \frac{f^2\rho_o}{gd_i}\left(\frac{\tilde{U}_{i+1}-\tilde{U}_i}{\rho_{i+1}-\rho_i} - \frac{\tilde{U}_i-\tilde{U}_{i-1}}{\rho_i-\rho_{i-1}}\right), \tag{2.10}$$

where ρ_o is the average density and d_i is the level depth. Substitutions of (2.9) and (2.10) into (2.5) produce a N-level equation. Then for $i \neq 1, n$

$$\tilde{U}_i F_i \phi_{i-1} + \{-\tilde{U}_i(F_i+G_i+K^2) + \tilde{\beta} + F_i(\tilde{U}_i - \tilde{U}_{i-1}) - G_i(\tilde{U}_{i+1}-\tilde{U}_i)\}\phi_i + \tilde{U}_i G_i \phi_{i+1}$$
$$-c\{F_i\phi_{i-1} - (F_i+G_i+K^2)\phi_i + G_i\phi_{i+1}\} = -iA_H K^3 \phi_i, \tag{2.11}$$

where

$$\left.\begin{aligned} F_i &= \frac{f^2\rho_o}{gd_i(\rho_i-\rho_{i-1})}, \\ G_i &= \frac{f^2\rho_o}{gd_i(\rho_{i+1}-\rho_i)}, \\ d_i &= \frac{z_{i+1}-z_{i-1}}{2}. \end{aligned}\right\} \tag{2.12}$$

The boundary conditions are

$$(\tilde{U}_1 - c)\left(\frac{\phi_1-\phi_o}{z_1-z_o}\right) - \frac{\tilde{U}_1-\tilde{U}_o}{z_1-z_o}\phi_1 = 0 \tag{2.13}$$

and

$$(\tilde{U}_n - c)\left(\frac{\phi_{n+1}-\phi_n}{z_{n+1}-z_n}\right) - \frac{\tilde{U}_{n-1}-\tilde{U}_n}{z_{n+1}-z_n}\phi_n = 0. \tag{2.14}$$

Substituting (2.13) and (2.14) into (2.5) and (2.6), we obtain, for $i = 1$

$$\{-\tilde{U}_1(G_1+K^2) + \tilde{\beta} + G_1(\tilde{U}_1 - \tilde{U}_2)\}\phi_1 + \tilde{U}_1 G_1 \phi_2 - c\{-(G_1+K^2)\phi_1 + G_1\phi_2\} = -iA_H K^3 \phi_1 \tag{2.15}$$

and for $i = n$,

$$\{\tilde{U}_n(F_n+K^2) + \tilde{\beta} - F_n(\tilde{U}_n - \tilde{U}_{n-1})\}\phi_n + \tilde{U}_n F_n \phi_{n-1} - c\{-(F_n+K^2)\phi_n + F_n\phi_{n-1}\} = -iA_H K^3 \phi_n \tag{2.16}$$

where

$$G_1 = \frac{f^2\rho_o}{gd_1(\rho_2 - \rho_1)} \quad \text{and} \quad F_n = \frac{f^2\rho_o}{gd_n(\rho_n - \rho_{n-1})}. \tag{2.17}$$

3. Numerical method

The N-level equations (2.11), (2.15) and (2.16) can be solved numerically using matrix eigenvalue methods. We can write those three equations as a matrix form,

$$\Big(A\Big)\begin{pmatrix}\phi_1\\ \vdots\\ \vdots\\ \phi_n\end{pmatrix} - c\Big(B\Big)\begin{pmatrix}\phi_1\\ \vdots\\ \vdots\\ \phi_n\end{pmatrix} = 0, \tag{3.1}$$

where

$$\left.\begin{aligned} &A_{i,i-1} = \tilde{U}_i F_i,\\ &A_{i,i} = -\tilde{U}_i(F_i + G_i + K^2) + \tilde{\beta} + F_i(\tilde{U}_i - \tilde{U}_{i-1}) - G_i(\tilde{U}_{i+1} - \tilde{U}_i) + iA_H K^3\\ &A_{i,i+1} = \tilde{U}_i G_i,\\ &A_{i,j\neq i-1} = A_{i,j\neq i} = A_{i,j\neq i+1} = 0,\\ &G_n = 0,\\ &F_1 = 0. \end{aligned}\right\} \tag{3.2}$$

and

$$\left.\begin{aligned} &B_{i,i-1} = F_i,\\ &B_{i,i} = -(F_i + G_i + K^2),\\ &B_{i,i+1} = G_i,\\ &B_{i,j\neq i-1} = B_{i,j\neq i} = B_{i,j\neq i+1} = 0,\\ &F_1 = 0,\\ &G_n = 0. \end{aligned}\right\} \tag{3.3}$$

Using the IMSL mathematical computer library, we can obtain complex eigenvalues by the iteration method.

Computing the eigenvalues by iteration takes considerable computer time but it is preferable to the shooting method, especially when there are more than one eigenvalue and approximate solutions cannot be obtained analytically. The velocity and density distributions of the mean state as a function of depth are derived from the hydrographic data and these do not lend to simple analytical equations.

4. Mean field.

According to the governing equations (2.11), the instability only depends upon the velocity difference $(\tilde{U}_i - \tilde{U}_{i-1})$, so computation of the complex phase speed can be done using relative geostrophic velocities.

The geostrophic velocity at depth z is expressed in terms of the specific volume anomaly as,

$$u - u_o = \frac{g}{f}\int_{-z_o}^{-z} \frac{\partial \delta}{\partial y} dz', \tag{4.1}$$

$$v - v_o = -\frac{g}{f}\int_{-z_o}^{-z} \frac{\partial \delta}{\partial x} dz', \tag{4.2}$$

where z_o is the reference level and

$$\delta = \alpha_{s,t,p} - \alpha_{35,0,p}, \tag{4.3}$$

where α is a specific volume of sea water. The geostrophic velocities were computed using gradients of specific volume anomalies from NODC hydrographic data compiled from 1950 to 1976, in the area of 130° W - 165° W and $20°N - 50°N$.

The computation procedure is as follows : 1) Calculate the specific volume anomalies at the standard depth of each station. 2) Divide the Northeast Pacific into 5° × 5° grids, and calculate the gradients of specific volume anomalies at the standard depth using the first order surface fitting method. 3) Integrate the gradients in depth and calculate the geostrophic velocity with respect to 1500 m. 4) Based on the similarity of each grid's hodographs with depth, combine the 5° × 5° grids into 7 typical regions. 5) Calculate

geostrophic velocities of 7 typical regions with respect to 3000 m, using the same procedure as described above. The geostrophic spirals for 7 regions are shown on Figure 2.

5. Choice of $(\Delta\rho d)_i$ for the three-layer model

The only mathematical difference between small amplitude perturbation equations in a layer and level model is the method used to evaluate ρ_i and $\tilde{U}_i$. In the level model, these are evaluated at the level heights, $z = z_i$, but in the layer model they are averaged over the layer depth and have discontinuities across layer interfaces. Here we choose the level model for evaluating those values.

To examine the real ocean instability problem using a layer model, the density step $\Delta\rho$ and/or layer depth D have to be specified. One logical choice for determining these might be to make the linear complex dispersion relation of a three-layer model the same as that of the continuous model. But we found it impossible to obtain the same range of unstable wave lengths and growth rates simultaneously from both models. Thus we follow Flierl's (1978) suggestion to select parameters by matching the linear dispersion relation for baroclinic Rossby waves of the continuous model with that of a three-layer model without shear. Dispersion relations of a continuous model are calculated numerically from Equations (2.11), (2.15) and (2.16) with $\tilde{U} = 0$ and one hundred levels between 0 and 5000 m. Matching the dispersion curves of the first two baroclinic modes and equating the net heat and salt contents of layers gives the layer depths and the corresponding density steps. This is equivalent to adjusting the layer depths until the two gravest Rossby radii of the layer model equal that of a continuous model. As baroclinic instability of zonal flow occurs at these radii scale, it is as our anticipation that such a dynamic constraint would also lead to a realistic model of the spiraling flows. The vertical structure function and dispersion diagram of region III for Rossby waves without shear are shown on Figure 3 as an example.

After dividing the eastern North Pacific into three layers by the above criterion, we can now compute the relative geostrophic currents in each layer. We found that in such a three-layer model of the North Pacific the horizontal gradients of vertically averaged density contribute more to the baroclinic shear than tha layer depth gradients (Table 1). The relative geostrophic velocities in each level are shown on Figure 2.

6. 3-level solutions.

Computations of the growth rates for a three-level model with and without Laplacian lateral friction as a function of wave number were done and are shown on Figures 4 - 10. We use $5 \times 10^5 cm^2/s$ as a horizontal eddy viscosity. Estimates of the eddy diffusion coefficient relate to the large scale motion which includes both the baroclinic eddy motions and other small scale features had been made in the subtropical Atalantic by Armi and Stommel (1983). They found the value of $5 \times 10^6 cm^2/s$. Estimates of this coefficient which should be used for scales smaller than the baroclinic eddies, 10 Km or less, are not available in the subtropical oceans (see Csanady, 1982, for estimates in coastal areas). We surmise that smaller scales have smaller eddy diffusivities because the diffusion coefficient is presumably related to the mixing length (Tennekes and Lumley, 1972). Therefore there is a degree of unrealism in our growth rate computaions, because there is an uncertainty that is related to an assumption that sub-eddy scales have a momentum diffusion coefficient of $5 \times 10^5 cm^2/s$. Presently, theory can do no better.

However, general circulation models do employ a minimum frictions for numerical stability and we wish to know how low levels of this a priori assigned viscosity would affect the linear wave properties. Thus frictional computation serves for us as a diagnostic tool to understand the growth of waves in general circulation models of the eastern North Pacific. No specific realism aside from the requirements of numerical stability and potentially small enstropy destruction is assigned to our choice of A_H.

Growth rates of the most unstable waves are tabulated in Table 2 with their wave lengths and periods. The most slowly growing waves are found in the subpolar area (region II) and have a period of more than 14 years. The fastest growing waves are located in the southward return flow region (region V), and these grow three times faster than the slowest growing waves (note that the California Current is east of region V). In the eastern North Pacific three-level model, the propagation direction of the most unstable waves is nearly southward, except for a north-eastward direction in region I which only has a northward component mean shear.

As found by other investigators, the time and length scales of the most unstable waves in a few layer model are too large when compared with observed mesoscale motions. In the southern regions, instabilities occur only with a nearly northward wave orientation because the strong β-effect and large Rossby deformation radius, compared to the magnitude of the mean shear, tend to stabilize all other directed waves (note that β-effect vanishes near the wave direction of 90°). In the northern regions, the maximum growth rates are between the shear direction and 90° because the β-effect and Rossby deformation radius are smaller in the high latitudes . In regions II and III, there is a second growth rate maximum at a higher wave number. The amplitude functions of these second maxima are surface trapped compared to the relatively large intermediate and bottom amplitudes in the case of the first maximum near 90° (see Fig. 7). At each horizontal wave number in a three-level model, two baroclinic modes are possible; one is a growing solution. The vertical structure functions of both modes changes with wave number.

In these velocity spirals lateral friction narrows the range of wave numbers for unstable waves and dissipates short unstable waves in all regions except in region I; there the lateral friction broadens the range of unstable meridional wave number. In this three-level ocean lateral friction of $A_H = 1.0 \times 10^8 cm^2/s$ would practically stabilize all regions except V and VII.

7. Continuous (multi-level) solution

Using the multi-level model, we compute the growth rates of unstable waves for selected regions. The level thicknesses are 100 m above 3000 m, and 500 m below 3000 m. Applying the semi-circle theorem of Section 2.1 to select the numerical solutions, we obtain only 2 - 4 stable solutions and four unstable solutions. Two of the four unstable solutions are bottom trapped mode (amplitude maximum below 3000 m), but because the bottom topography is not considered and there are few hydrographic data below 3000 m, we do not feel these are physically realizable and thus they are not presented. One of the unstable solutions is a surface trapped mode which has a maximum amplitude at the surface and a very small amplitude below 200 m. Because our model does not include the Ekman layer dynamics nor the seasonal thermocline, this mode is also not considered physically meaningful. The most robust unstable solution has a maximum amplitude at 200 - 1000 m, and as this mode can also be obtained from a three-level solution (although with quite different growth rates) a direct comparison can be done. The slowness curves of stable waves for region III are shown on Figure 11. The e-folding times of most unstable waves are tabulated on Table 2, with their wave lengths and periods for four regions. Compared to a three level model these show more realistic eddy growth time scales of 50 -200 days and wave lengths of 60 -200 km. In the northern regions, the most unstable waves are short waves and have a maximum wave amplitude at 200 m compared to the southern region with a maximum wave amplitude at 800 m (Fig. 13). The short waves are stabilized by lateral friction (Fig. 12). In a frictionless model, as the vertical resolution increases, the high wave number cut-offs move to higher wave number. So, when friction is added stabilization by friction is more effective on this high wave number band on a continuous model than on a three-level model.

The two general results from continuous model are the south-westward propagation of the most unstable waves and the subsurface amplitude maximum in the subtropical region

(Fig. 13). Cox (1985) showed a similar subsurface maximum of eddy kinetic energy at the core of the North Equatorial Current from his 18 level primitive equation numerical model.

8. Discussion.

Baroclinic Rossby waves in an environment without a mean shear can have an infinite number of vertical normal modes, but when mean shear exists only a limited number of stable or unstable normal modes are found because limitations on phase speed and growth rates are now imposed (see Eqn. (2.7)). Because the phase speed of high vertical mode waves can be slower than the mean flow, the mean flow does not allow for the existence of all the high vertical mode Rossby waves . Our calculations show that only very few stable Rossby waves can exist in the Northeast Pacific.

As noted by other investigators, a non-zonal shear makes the ocean more unstable than a strictly zonal shear because north-southward propagating waves feel little of the stabilizing β-effect. A rotating shear also makes the ocean more unstable than a non-rotating shear. Because instability depends upon the velocity difference of mean flow $(\tilde{U}_i - \tilde{U}_{i-1})$ and on the vector plane, the velocity difference is minimum for the non-rotating spirals.

It is quite clear that different mean geostrophic flows coupled with β-effect and the size of Rossby deformation radius are strongly reflected in the stability characteristics of both three-level solutions and continuous solutions. If every region had the same mean shear magnitude and direction, waves would be more unstable in the northern region than in the southern region because of the diminished β-effect. But from a 3 level solution, growth rates increase to the south except in region VI where the magnitude of shear is the smallest among all the regions. The subtropical gyre has progressively more southward shear with decreasing latitude and our computations show that this feature, at any level, is usually increasingly sufficient to destabilize the flow. To demonstrate the effect of latitudinally varying β and Rossby deformation radius in this ocean of small mean shear, we computed the growth rates at region VII using β value and Rossby deformation radius of region I. The

dramatic change is noted when Figure 14 is compared with Figure 4. Kang *et al.* (1982) showed from their two-level analytical solutions that the direction of shear is important to the unstable Rossby waves. According to their computation, the westward shear is more unstable than the eastward shear, and the meridional shear is more unstable than the zonal shear of equal magnitude. From our 3 level computation, the region VI, which has a southward shear, has almost the same growth rates as the region II, although it has the smallest shear magnitude and is at the low latitude.

The wave length of most unstable waves also vary significantly among regions. The wave length of the northern-most regions is only one third of that in the southern-most region. Because eddies prefer to have the length scale of the Rossby deformation radius L_D,

$$L_D = \frac{1}{f}\left(\frac{g\Delta\rho D}{\rho_o}\right)^{\frac{1}{2}}$$

where D is the vertical length scale of motion, and because the Coriolis parameter f is two times larger and $\Delta\rho$ is two times smaller in the northern region than in the southern region, the Rossby deformation radius is about two times smaller in the northern region (Table I). Therefore, the dissipation of growing waves by scale selective friction will play an important role in their growth in a spatially non-uniform fashion as seen on our three-level and continuous model computations.

In the continuous model analysis, we have only one physically meaningful unstable solution which has a subsurface amplitude maximum. Growth rates are much faster in the continuous model than in the three-level model and the wave directions of the unstable waves are near the shear directions of the upper levels. Growth rates and the wave directions are very sensitive to the mean shear.

The most general statement is, however, that aside from the existance of unstable waves in either a three-level or a continuous model of the northeast Pacific, there appears to be very little direct relationship between the unstable wave properties of the two models. As shown

in Figure 3, the linear Rossby waves can be made effectively equivalent, primarily because the vertical density gradient profiles have simple level model representations. Because the baroclinic unstable waves require the existence of both shear and vertical density gradients, the inadequacy of representing the spiraling shear by three layers (specially $d^2\tilde{U}/dz^2$) is evident. In Figure 15 we present the growth rate diagrams for a three-level, six-level and 34-level model of region VI, all in the same scale. Region VI is chosen for this dramatization because its shear characterizes those of all the other regions. And six levels were chosen to resolve the mean velocity spiral in nearly equal increments in both directions. It is obvious that the six-level model now shows both qualative and quantative close agreement with the 34-level computation. A 64 level computation does not change the 34-level results. The conclusion we draw is that in the Northeast Pacific, two and three-level (or layer) models of the linear instability process are not realistic in either space or time scale properties or vertical structure functions of the linear shear waves which extract energy from the spiraling observed mean shear across the thermocline. At least six-level model is required for realism.

We emphasize that our calculation applies only to linear shear waves and the detailed fashion in which energy is extracted from mean flow where waves are growing. At finite amplitude where there is other eddy transport process, as barotropization (Rhines, 1977), this can be represented by low resolution models. Our results are to be contrasted with those of Holland and Haidvogel (1979) who found that linear instability of a two-layer model in the Gulf Stream region was adequate to describe the vertical structure of growing waves as well as the finite amplitude equilibrium process.

9. Conclusion.

The computation of the complex phase speed of baroclinic waves is done by solving linear quasi-geostrophic level equations, and by using the eastern Pacific geostrophic non-zonal mean flow and density structure. It shows that the spiraling mean flow coupled with latitudinally varying β-effect and Rossby deformation radius can produce mid-ocean baroclinic

instability with significant space dependent properties. The most unstable waves have a wave length of 60 - 200 km, the smallest scale is in the northern region (47.5°N) and the largest scale is in the southern region (22.5°N). Because short waves can be dissipated by scale selective friction more easily than long waves, lateral friction may prevent growth of northern eddies very effectively (especially in numerical models). From continuous model computation the periods of 50 - 200 days are obtained for the most unstable waves and thus they are consistent with known eddy time scales. The waves e-fold within one period, and propagate eastward in the area north of the subpolar front and southwestward in the subpolar region. Vertical amplitude functions show a subsurface maximum of kinetic energy at 200 - 800 m, and vertical phase changes occur above 700 m depth.

Our linear analyses with fine vertical resolution demonstrate that the quasi-geostrophic waves produced by baroclinic instability can be a good candidate for explaining the observed eddy field at the Northeast Pacific, but can only show the birth and early growth of the eddies. The character of the growing instabilities will critically depend on the vertical resolution of the model. So, non-linear analysis with sufficient vertical resolution (at least six-level in the northeast Pacific) is required to realistically study the whole life cycle of the mid-ocean eddies.

	Layer Depth (m)			Density (σ_t)			East-west velocity (cm/s)			North-south velocity (cm/s)			Rossby radius (Km)
Area	D_1	D_2	D_3	σ_{t1}	σ_{t2}	σ_{t3}	U_1	U_2	U_3	V_1	V_2	V_3	
I	300	650	4050	26.42	27.18	27.74	1.76	0.51	0.0	0.45	0.15	0.0	22
II	300	600	4100	26.11	27.05	27.75	1.56	0.31	0.0	-0.33	-0.19	0.0	25
III	350	600	4050	25.99	26.93	27.75	1.01	-0.26	0.0	-0.49	-0.21	0.0	33
IV	350	600	4050	25.93	26.99	27.75	1.44	0.26	0.0	-0.57	-0.23	0.0	33
V	300	600	4100	25.48	27.00	27.74	1.33	0.19	0.0	-1.27	-0.39	0.0	35
VI	300	550	4150	25.26	26.80	27.75	0.31	-0.92	0.0	-0.62	-0.27	0.0	44
VII	250	500	4250	24.78	26.85	27.75	-1.92	-1.19	0.0	-1.34	-0.47	0.0	50

Table 1. The parameters and internal Rossby radius of deformation of seven regions used for three level model computation.

Area	Layer Depth (m)			Density (σ_t)			East-west velocity (cm/s)			North-south velocity (cm/s)			Rossby radius (Km)
	D_1	D_2	D_3	σ_{t1}	σ_{t2}	σ_{t3}	U_1	U_2	U_3	V_1	V_2	V_3	
I	300	650	4050	26.42	27.18	27.74	1.76	0.51	0.0	0.45	0.15	0.0	22
II	300	600	4100	26.11	27.05	27.75	1.56	0.31	0.0	-0.33	-0.19	0.0	25
III	350	600	4050	25.99	26.93	27.75	1.01	-0.26	0.0	-0.49	-0.21	0.0	33
IV	350	600	4050	25.93	26.99	27.75	1.44	0.26	0.0	-0.57	-0.23	0.0	33
V	300	600	4100	25.48	27.00	27.74	1.33	0.19	0.0	-1.27	-0.39	0.0	35
VI	300	550	4150	25.26	26.80	27.75	0.31	-0.92	0.0	-0.62	-0.27	0.0	44
VII	250	500	4250	24.78	26.85	27.75	-1.92	-1.19	0.0	-1.34	-0.47	0.0	50

Table 2. Growth rates and wave characteristics of the most unstable waves computed from three level and continuous model.

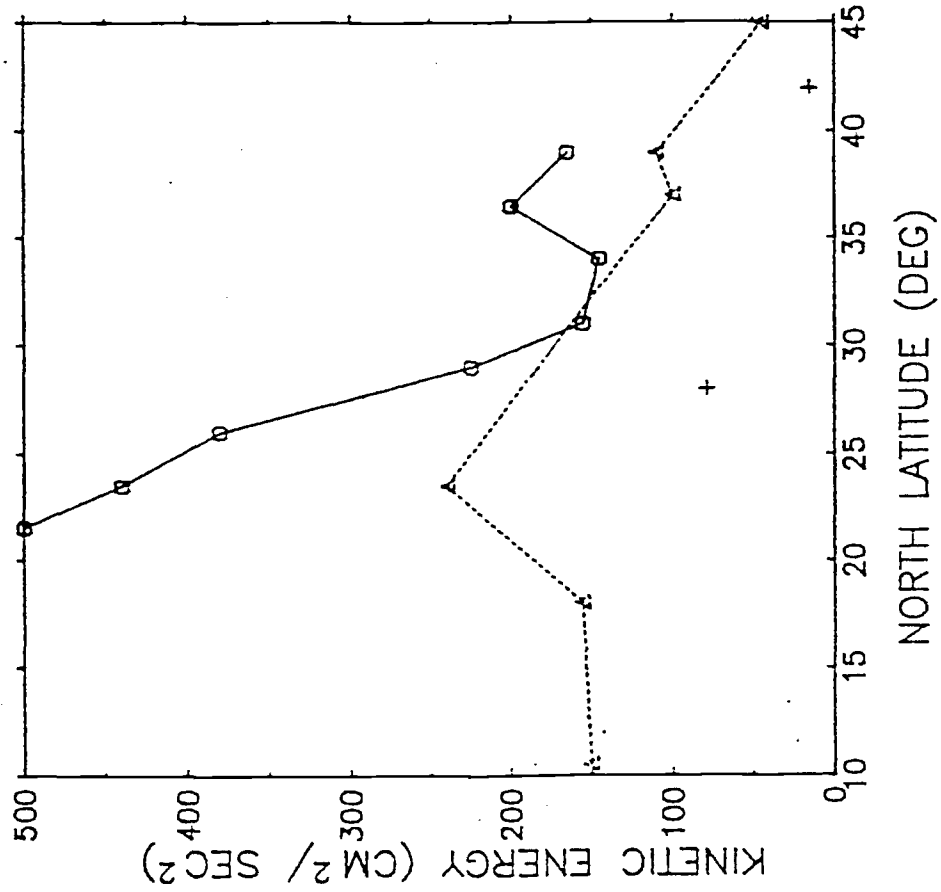

Fig. 1. Direct estimates of eddy kinetic energy between 138°W and 172°W as a function of latitude from Niiler and Reynolds (1984) (solid line with box), between 130°W and 170°W from McNally *et al.* (1983) (dotted line with triangle) using drifting buoy and at 152°W (1985) (+) using current meter data.

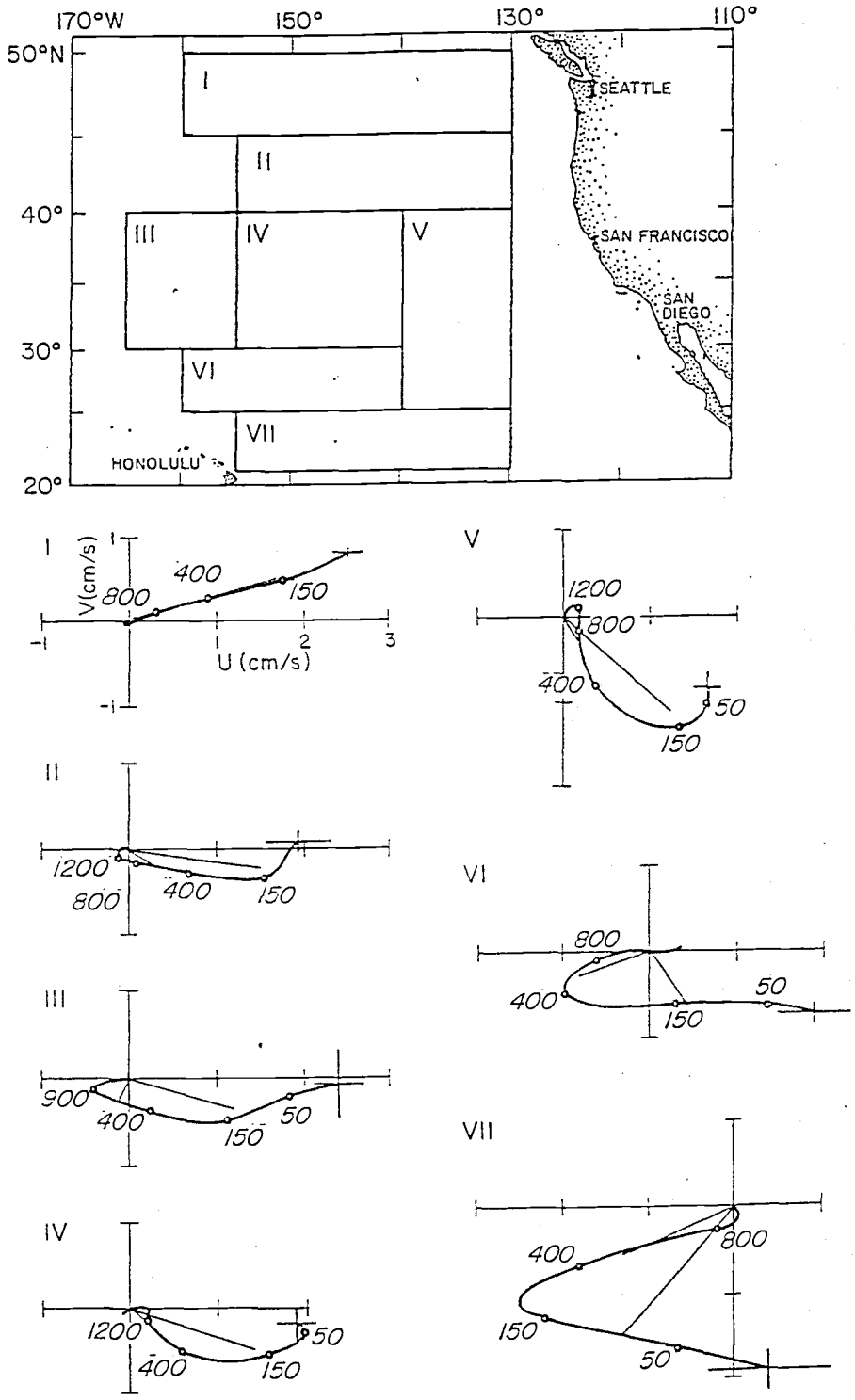

Fig. 2. Geostrophic hodograph with mean layer geostrophic currents of 7 regions (dotted line). The extents of these regions are in the Table 1. The estimated errors at 3000m (the greatest error) are shown with the surface points for convenience.

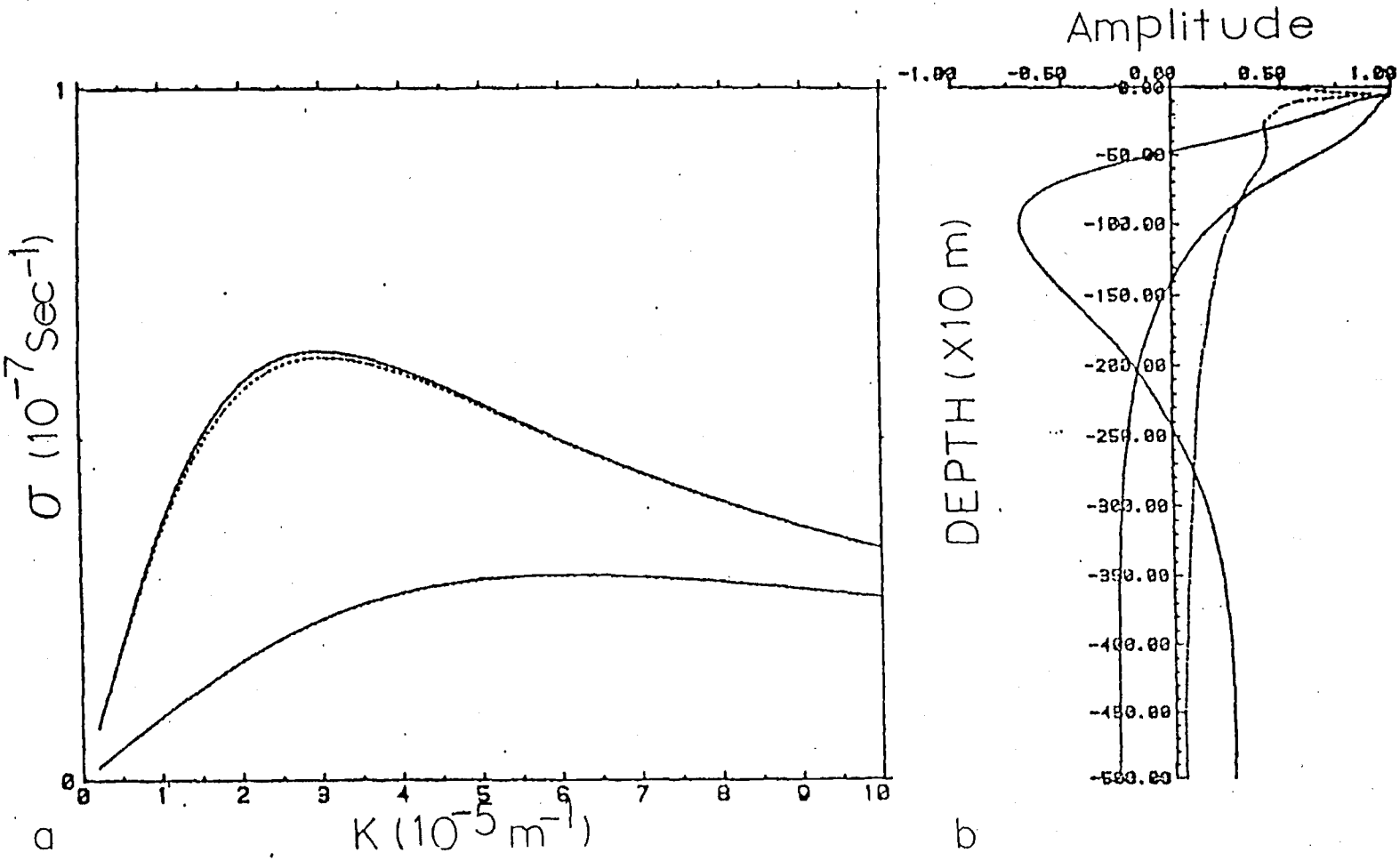

Fig. 3a. Dispersion relation for Rossby wave normal mode of Region III. The solid line is for the continuous model and dotted line is for the three-layer model after adjusting layer depth.

Fig. 3b. Vertical structure functions of the first and second baroclinic mode of continuous model in the Region III. The dotted line is the Brünt—Väisälä frequencies scaled from 0 to 5 c. p. h.

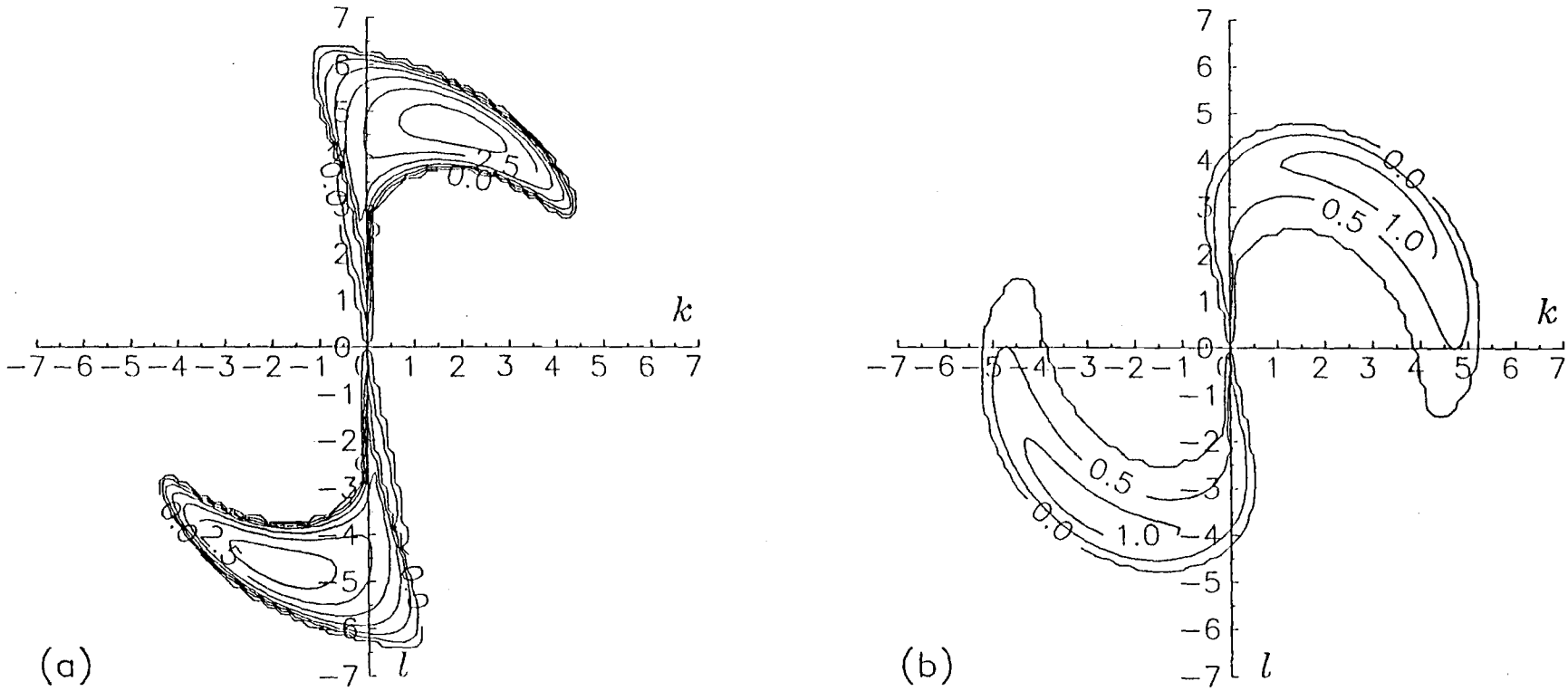

Fig. 4. Growth rate contours in unit of 10^{-8} s^{-1} for unstable Rossby wave for Region I (a) without lateral friction and (b) with lateral friction. The wave numbers have units of 10^{-5} m^{-1}.

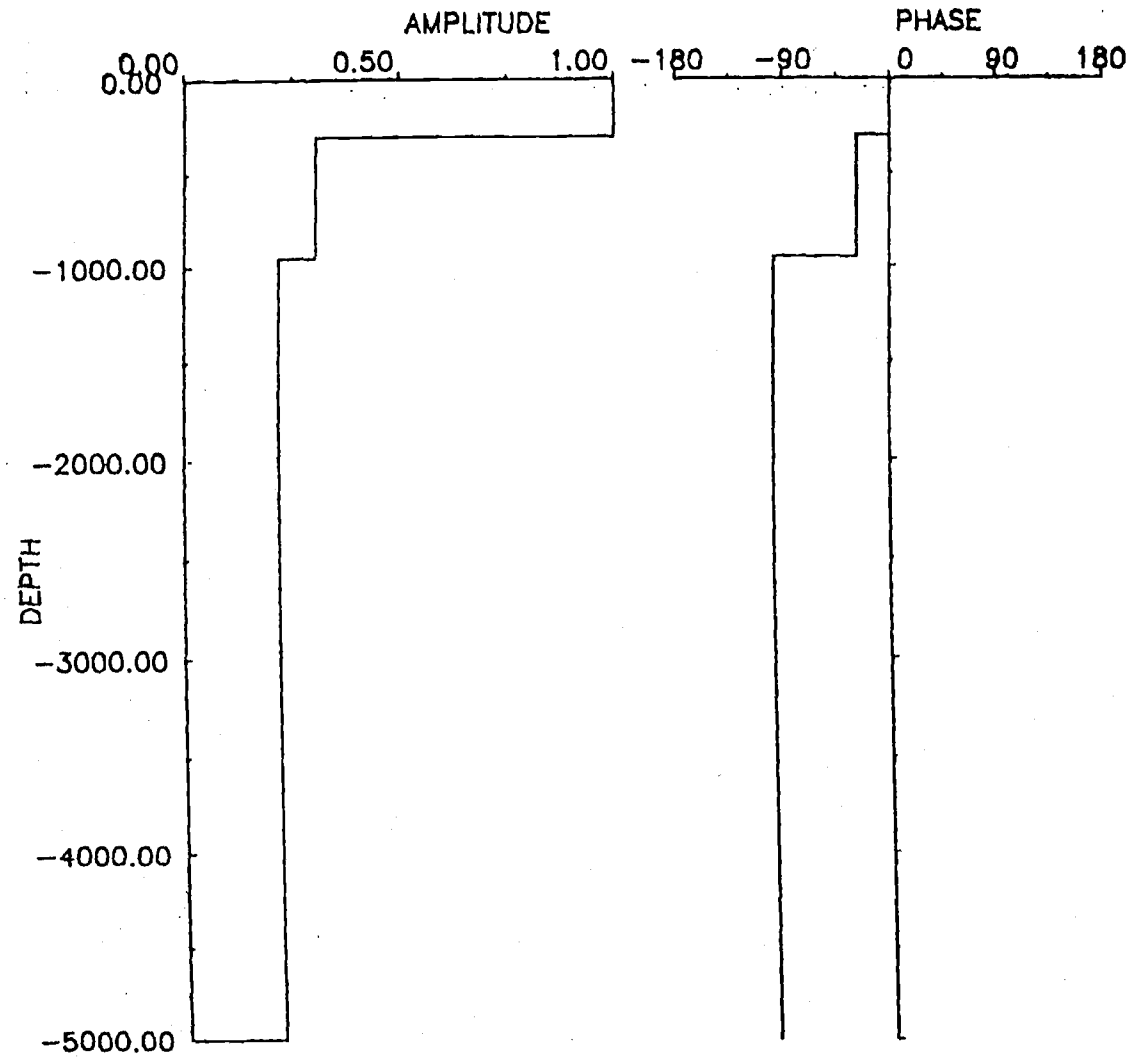

Fig. 5. Amplitude and phase of the most unstable waves in the Region I.

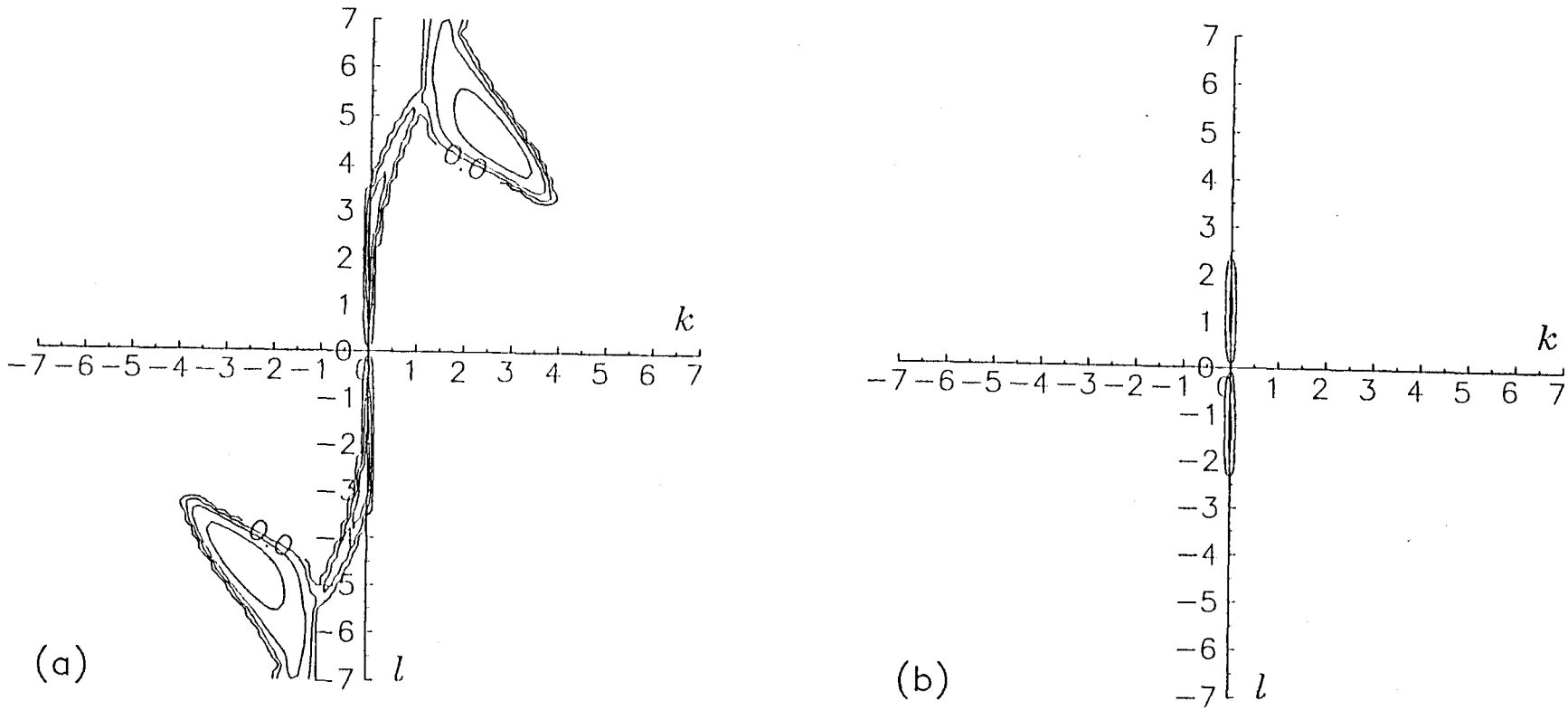

Fig. 6. Growth rate contours for unstable Rossby wave for Region II (a) without lateral friction and (b) with lateral friction (same units as in Fig 4).

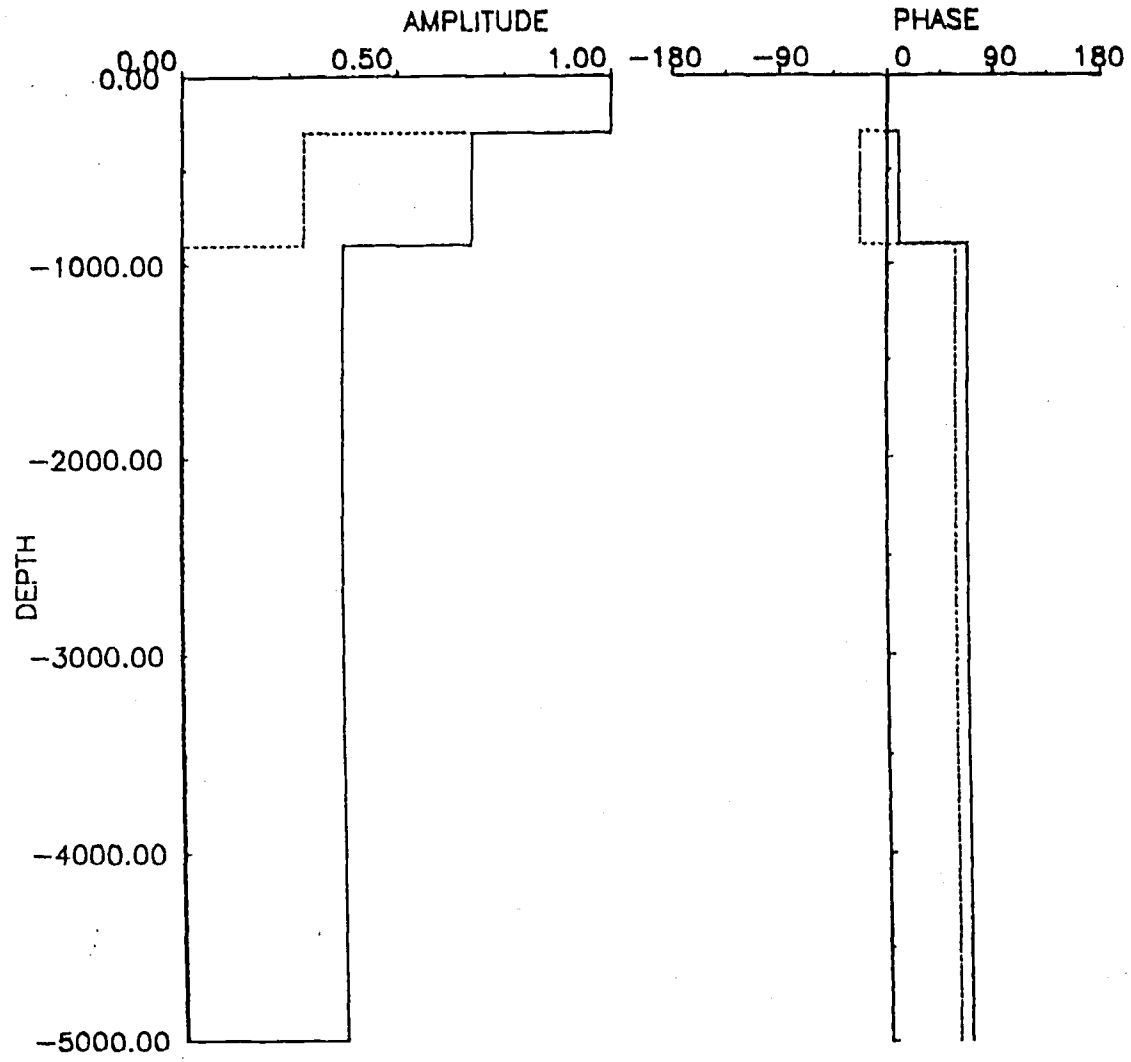

Fig. 7. Amplitude and phase of the most unstable waves in the Region II. Solid line is for first mode with friction and dotted line is for second mode with friction.

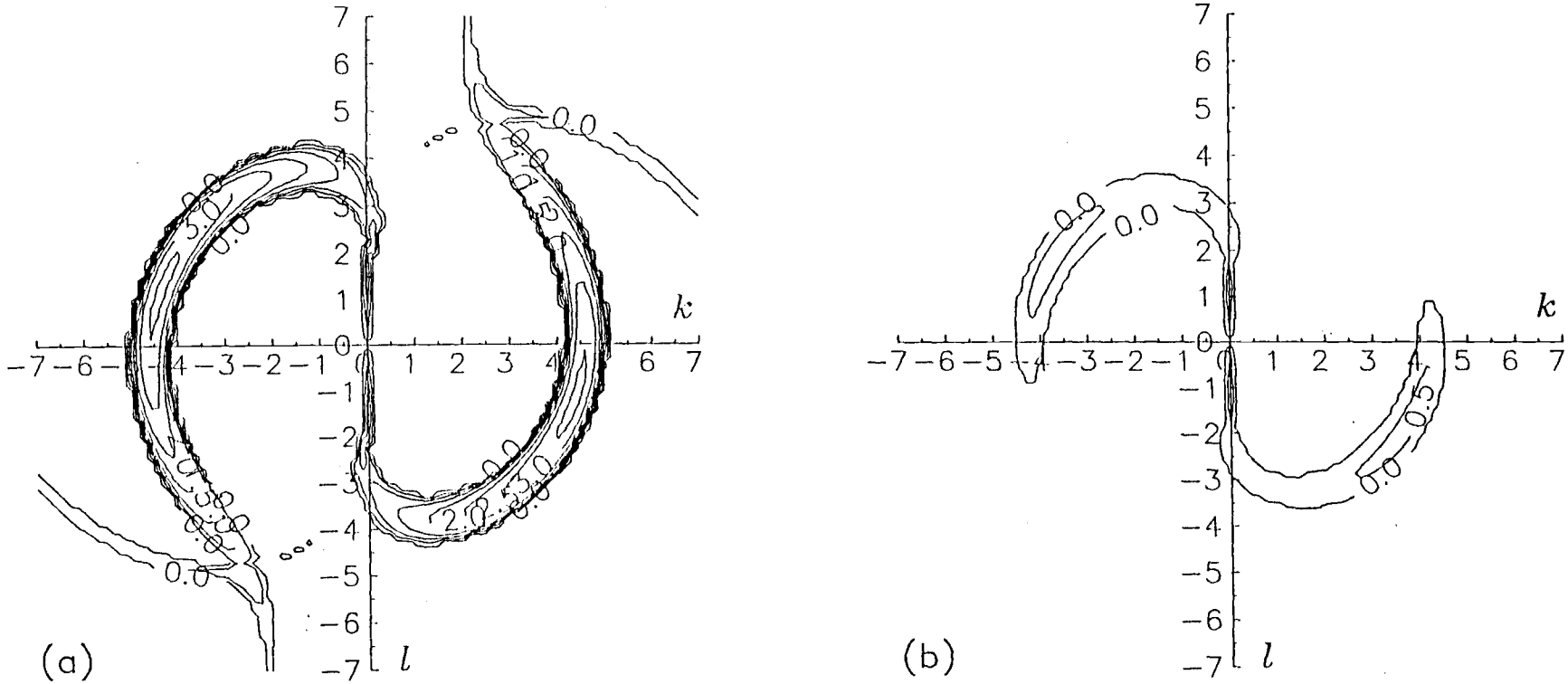

Fig. 8. Growth rate contours for unstable Rossby wave for Region III (a) without lateral friction and (b) with lateral friction (same units as in Fig 4).

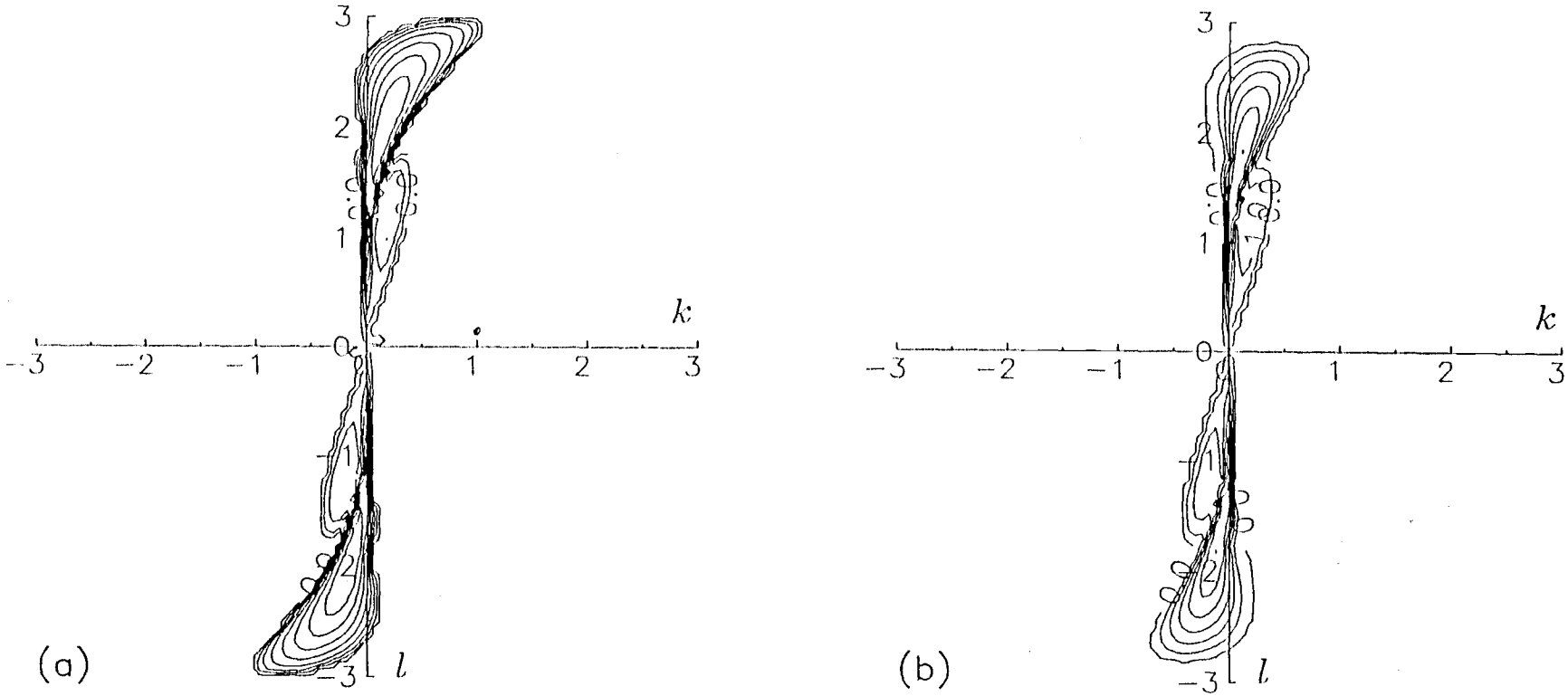

Fig. 9. Growth rate contours for unstable Rossby wave for Region V (a) without lateral friction and (b) with lateral friction (same units as in Fig 4).

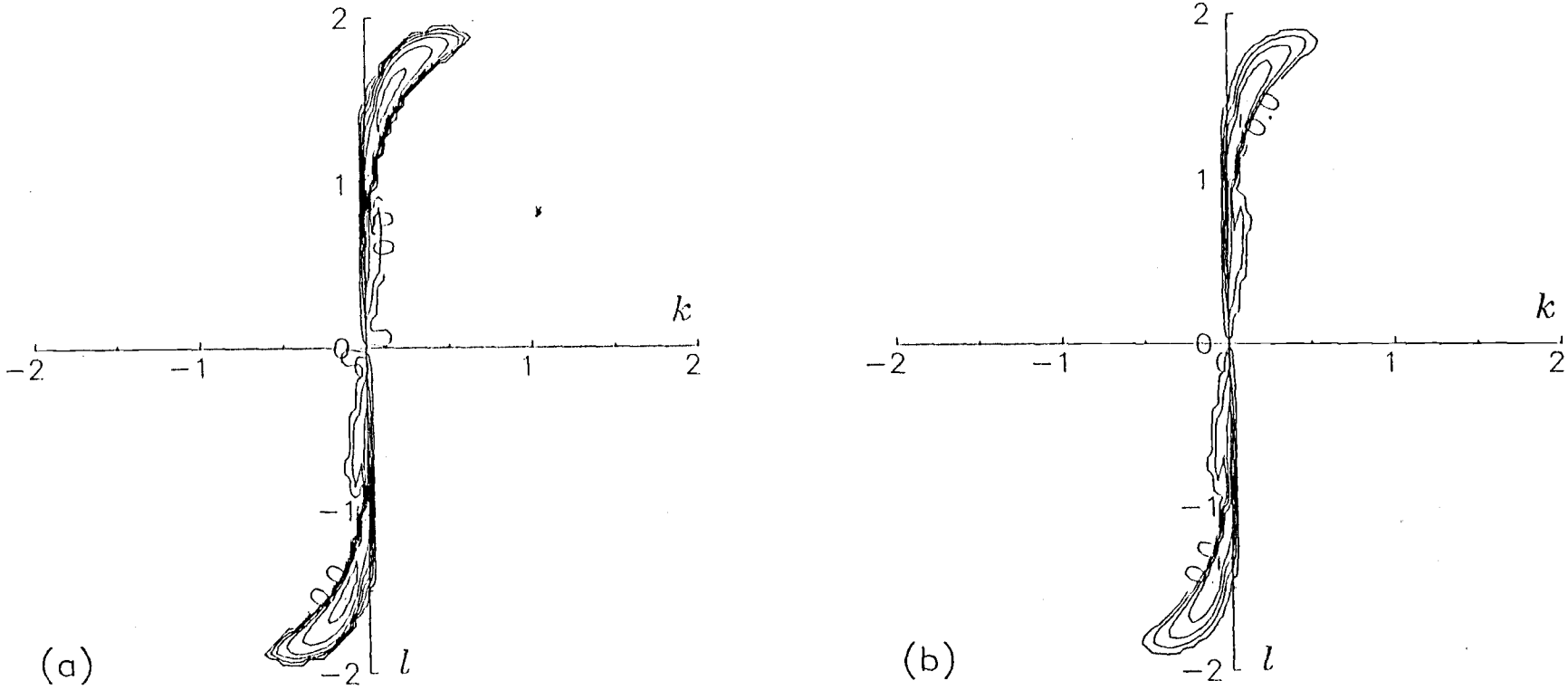

Fig. 10 Growth rate contours for unstable Rossby wave for Region VII (a) without lateral friction and (b) with lateral friction (same units as in Fig 4).

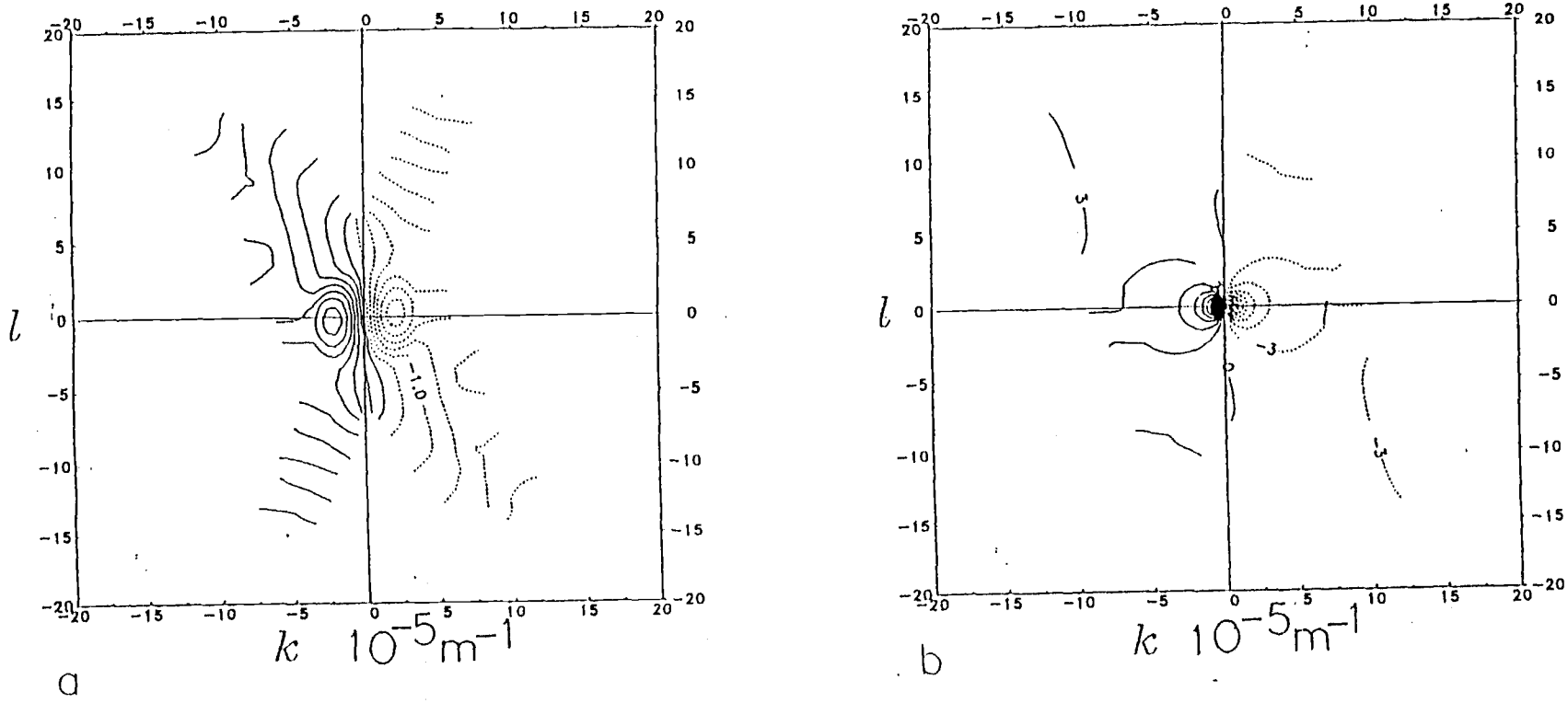

Fig. 11. Slowness curves of the stable Rossby waves in the Region III (a) for barotrophic mode and (b) first baroclinic mode.

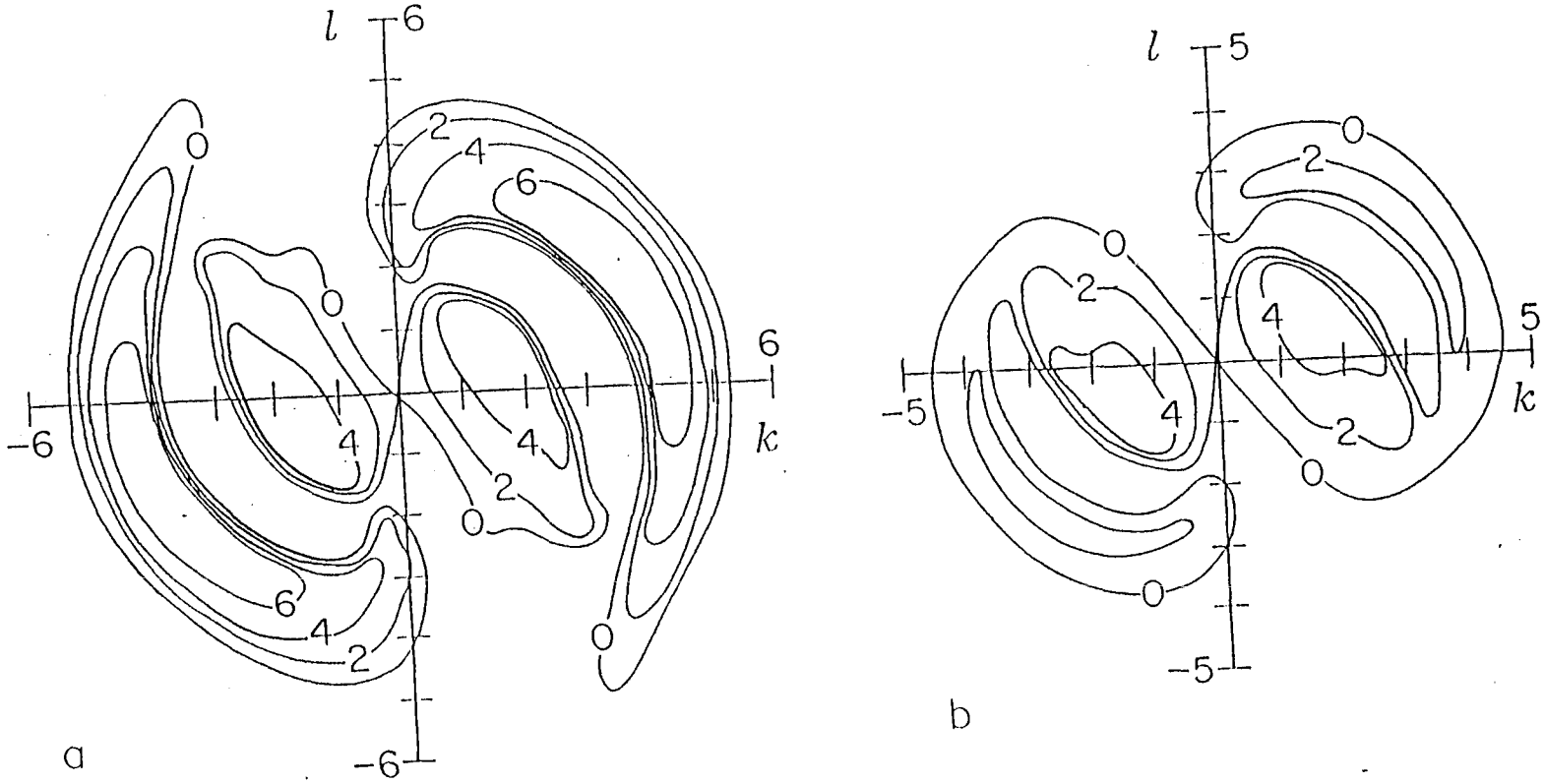

Fig. 12. Growth rate contours (in units of 10^{-8} s^{-1}) of unstable waves computed from continuous model for the intermediate mode which has the subsurface maximum amplitude (a) without friction and (b) with friction in the Region VII. The wave numbers have units of 10^{-5} m^{-1}.

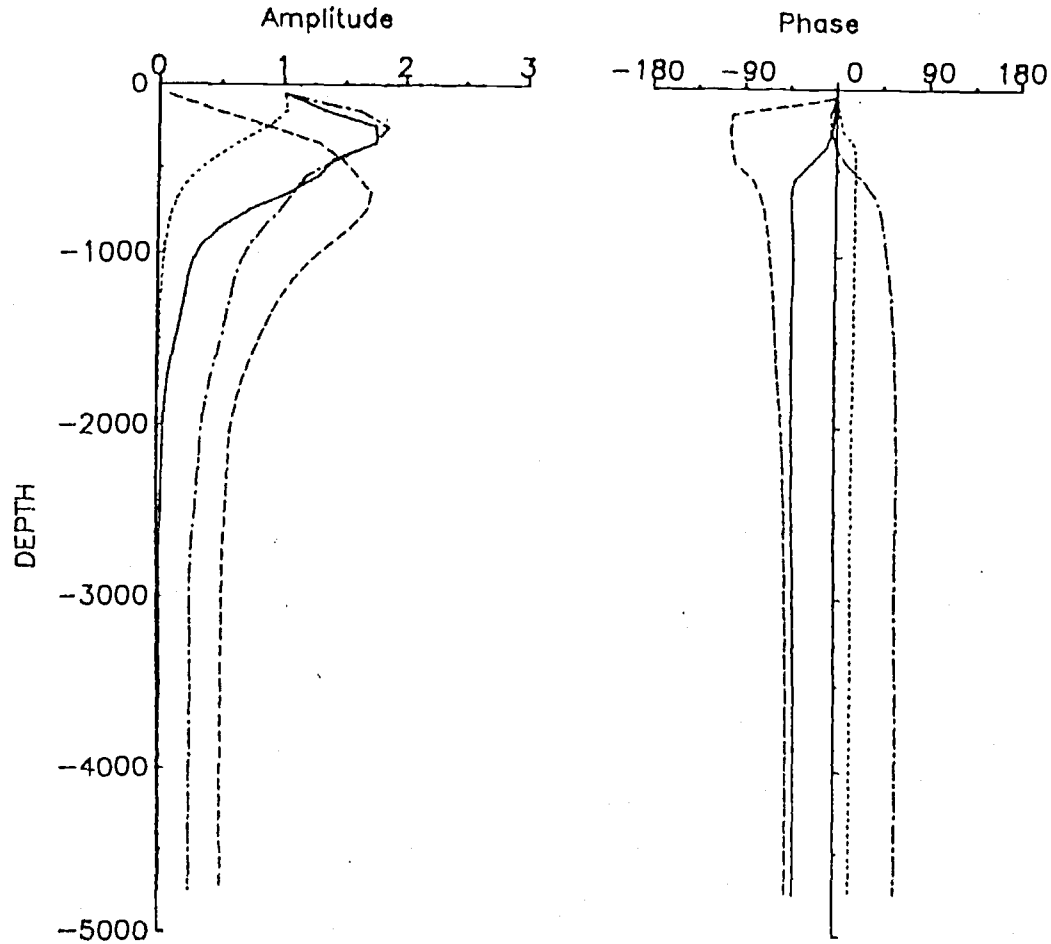

Fig. 13. Amplitudes and phases of the most unstable waves computed from continuous model in the region I (solid line), III (dotted line), V (dot-dashed line) and VII (dashed line).

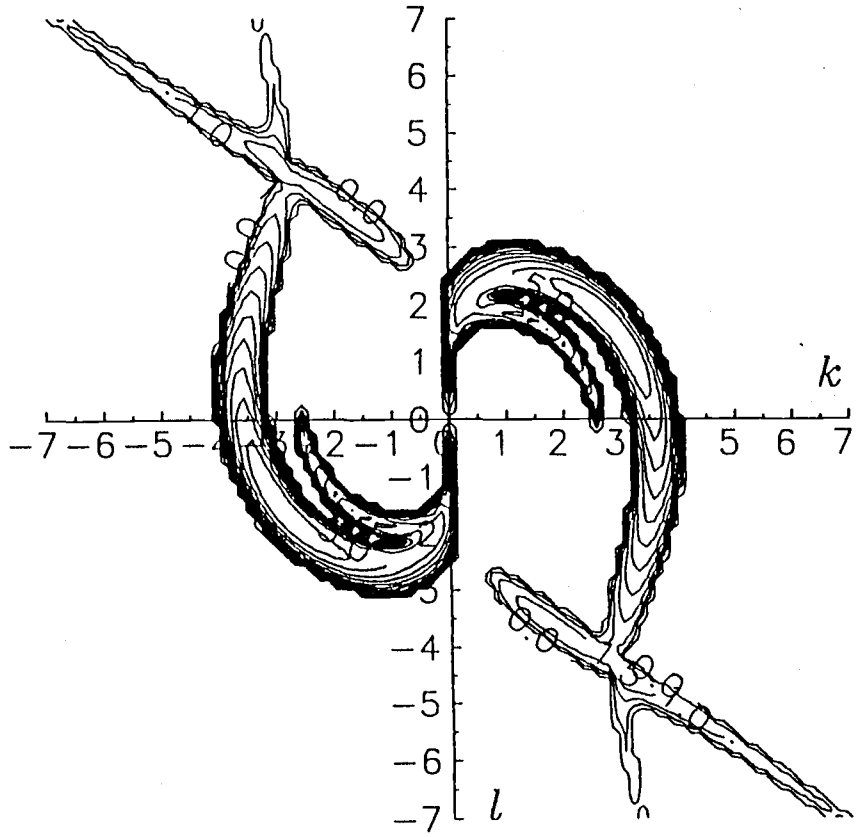

Fig. 14. Growth rate contours of unstable waves in the latitude of 47.5° N using mean shear of Region VII instead of Region I (in same units as Fig. 4).

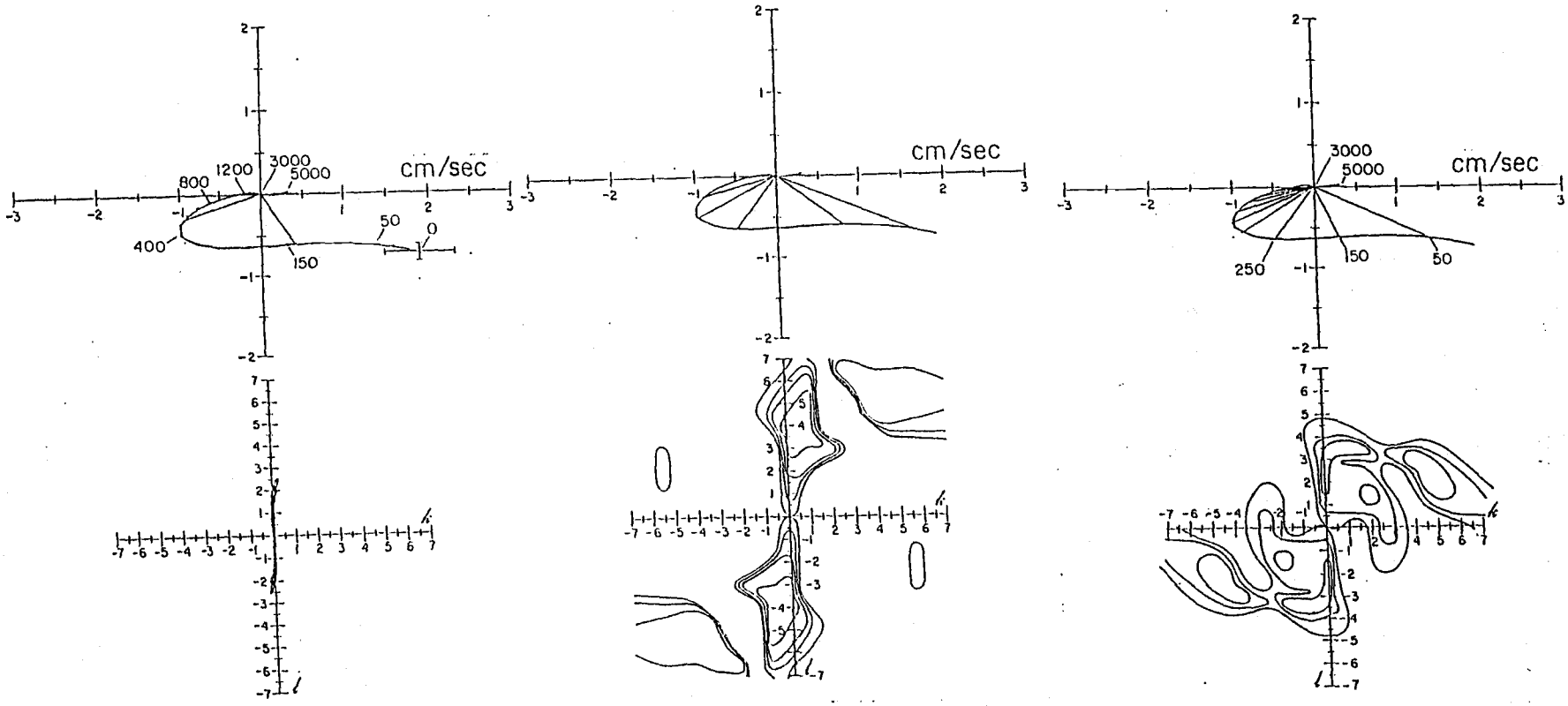

Fig. 15. Growth rate contours (in units of $10^{-8}s^{-1}$) of unstable waves (bottom) and the mean geostrophic velocity spirals with level velocities (top): The three-level (left), the six-level (middle), and the 34 level (right) model. The wave numbers have units of $10^{-5}m^{-1}$.

Chapter III

Characteristics of the Non-linear Unstable Waves in the Eastern Ocean Basin - Numerical Experiments Using a Three-layer Quasi-geostrophic Model

Dong-Kyu Lee

College of Oceanography
Oregon State University
Corvallis , OR 97331

ABSTRACT

Non-linear unstable waves in the eastern ocean basin are analyzed using a three-layer quasi-geostrophic numerical model. The numerical model in this study differs from the one used by Holland (1978), in two respects: i) each layer except the bottom layer is forced to maintain a devised initial mean circulation in the absence of meso-scale motion. The waves are produced by initial small perturbations added to the mean flow, and ii) a strong viscosity western boundary area (sponge layer) makes western boundary currents stable and absorbs all the waves entering into the area.

The first experiment is performed with 300 $\times$ 150 grids of 20 Km intervals using a mean flow of 1 - 2 cm/s. The initial mean stream function of the upper layer is an idealized, smooth and closed stream function. It is symmetric in both axes. The middle layer has a gyre center close to the northern boundary. The local growth rates by linear stability analysis in the southward return flow region near the eastern boundary are the same in the westward return flow region near the southern boundary. Local energetics are calculated to highlight the differences between the eastern and southern regions. The maximum eddy energy occurs near the center of the southern boundary, and is caused by the westward propagation of unstable waves. The second experiment uses a stronger mean field of 3 - 4 cm/s and eddies fill the southern half of the gyre. The total equilibrium eddy kinetic energy per unit area becomes 10 - 15 times bigger than the first experiment although the linear growth rates are only two times bigger. Two dominant waves are found that have the same periods as the two most unstable waves in the linear stability analysis. The short waves (periods of 120 days) propagate to the west and form several wave trains parallel to the southern boundary. The long waves (periods of 200 days) propagate to the south-west. These two waves are remarkably similar to measurements of open ocean eddies at 28°N, 152°W. There are high eddy activities in the southern region, but the eastern and northern regions are vacant

of eddies because of these westward and south-westward propagating unstable waves.

1. Introduction

Recent current measurements in the Northeast Pacific along 152°W (Niiler and Reynolds, 1984, Niiler *et al.*, 1987) showed that the eddy kinetic energy per unit volume increases to the south and reaches its maximum in the subtropical area. Lee and Niiler (1987, hereafter, LN), in their local linear baroclinic instability study, tried to explain these features by calculating growth rates in the various regions of the Northeast Pacific using the geostrophic mean current from historic hydrographical data. They found that the subtropical area has the same local growth rates as the subpolar area because of the south-westward shear, even though the Rossby radius of deformation is two times larger in the subtropical regions than in the subpolar regions. But they failed to relate the eddy energy distribution to the local growth rates. The linear local growth rates do not relate to the observed eddy energy level in the Northeast Pacific! The first numerical study which shows these eddy features in the mid-ocean was done by Cox (1985), using his 18 level primitive equation model. He identified a band of high eddy kinetic energy centered on the westward return flow of the subtropical gyre. The characteristics of these subtropical eddies (periods of 50 days and 400 Km wave lengths) agree reasonably well with observations by Fu *et al.* (1982) in the subtropical North Atlantic, except that the periods are shorter than the observed periods due to the large model mean flow (4.1 cm/s) compared to the observed mean flow (1 - 2 cm/s).

This paper is an extension of the linear stability analysis by LN to a non-linear baroclinic growth of unstable waves in the eastern ocean basin, using a three-layer quasi-geostrophic numerical model. Our model is the quasi-geostrophic (QG) three-layer model with a flat bottom described by Holland (1978), but it is different from his model; first, each layer except the bottom layer is forced to maintain its initial mean circulation in the absence of meso-scale motions. The waves are produced by adding a small perturbation to the initial stream function. Thus the forcing function is for

maintaining the basic circulation rather than for spinning up the gyre from a motionless ocean. Second, we concentrate our analysis on the eastern basin, which is far from the strong western boundary current effects, using a strong western viscosity area (sponge layer) to absorb the wave energy that propagates into the west. This sponge layer also makes western boundary currents stable. The intercomparison study of the QG model with the primitive equation (PE) model by Harrison and Semtner (1986) suggested that the quasi-geostrophic assumptions used in the QG model are not always valid, especially for the basin scale time average circulation as well as for the conditions in and near the western boundary currents. For this study, quasi-geostrophic assumptions are adequate to describe the evolution of mid-ocean eddies.

We will emphasize the geographical variation of eddy kinetic energy in the final equilibrium state and explain these differences by the characteristics of the fully developed meso-scale eddies and the calculation of local energetics of two regions: near the eastern and the southern boundaries of the gyre. After a description of the models and derivation of terms for local energetics in Section 2, two experiments of 300×150 grids (6000 Km zonal and 3000 Km meridional model size including the sponge layer) are analyzed in Section 3. To show the reasoning drawn from Section 3.1 and 3.2 more qualitatively, two additional long and thin (250×40 and 40×250 grids) box experiments are discussed in Section 3.3. A discussion of three model experiments will follow in Section 4.

2. Description of model

2.1. The governing equations

The model is one presented by Holland (1978), which is based on the quasi-geostrophic potential vorticity equations applied to the three-layer ocean of a constant depth in a closed basin. The potential vorticity equations for this three-layer

model are,

$$\frac{\partial}{\partial t}\nabla^2\psi_i = \mathbf{J}(f+\nabla^2\psi_i,\psi_i) - (\frac{f_o}{H_i})w_{i+1} + (\frac{f_o}{H_i})w_{i-1} + A_H\nabla^4\psi_i + F_i \tag{2.1}$$

for $i = 1, 3, 5$ and

$$\frac{\partial}{\partial t}(\psi_{j-1} - \psi_{j+1}) = \mathbf{J}(\psi_{j-1} - \psi_{j+1},\psi_j) - (\frac{g_j'}{f_o})w_j \tag{2.2}$$

for $j = 2, 4$. Throughout this paper the subscript j is used for the interface level: 2 and 4, and i is used for the level at the center of each layer: 1, 3 and 5 (see Fig. 16). In these equations,

$$\left.\begin{aligned} w_o &= w_6 = 0 \\ g_j' &= g\frac{\rho_{j-1}-\rho_{j+1}}{\rho_o} \\ f &= f_o + \beta(y - y_o) \\ \psi_j &= \frac{(H_{j-1}\psi_{j+1} + H_{j+1}\psi_{j-1})}{(H_{j-1} + H_{j+1})} \end{aligned}\right\} \tag{2.3}$$

where w_j is the vertical velocity at the interface, ψ_i is the stream function at the level Z_i, ψ_j is the stream function at the layer interface, g_j' is the reduced gravity, H_i is the layer depth, f is the Coriolis parameter, y_o is the mid latitude of the basin where f_o and β are calculated and $\mathbf{J}$ is the Jacobian operator. Laplacian lateral friction is used and A_H represents the horizontal eddy viscosity coefficient, which is 100 m^2s^{-2} in the eastern two thirds of the model.

The forcing function F_i is

$$F_i = -\mathbf{J}(f+\nabla^2\tilde{\psi}_i,\tilde{\psi}_i) + (\frac{f_o}{H_i})\tilde{w}_{i+1} - (\frac{f_o}{H_i})\tilde{w}_{i-1} - A_H\nabla^4\tilde{\psi}_i \tag{2.4}$$

for $i = 1, 3$ and

$$F_5 = 0 \tag{2.5}$$

where $\tilde{\psi}_i$ is the devised initial stream function at level i and $\tilde{w}_{i\pm1}$ are the initial vertical

velocities on the layer interfaces.

The boundary conditions are: i) ψ_i is constant along the boundary but a function of time (no normal flow through the boundary) and ii) slip boundary conditions, i.e., $\nabla^2\psi_i = 0$ along the boundary.

We start the model calculation with the devised smooth stream function plus a small random perturbation as an initial stream function. The vertical structure of the model is schematically presented in Fig. 16.

2.2. The western sponge layer

To model the Northeast Pacific eddy field far from the high eddy activity area caused by the strong baroclinic instabilities of the western boundary current, using an open western boundary becomes necessary. The sponge layer is used to overcome the dynamical or numerical difficulties that arise from using an open boundary. Chapman (1986) tested various numerical methods applied to the coastal wave model, and found that the sponge layer with an Orlansky (1976) radiation condition is the best method for dealing with an open boundary. Barnier (1986) tested the behavior of the sponge layer by the westward propagating barotropic Rossby waves in the box model and concluded that the sponge dampens the fast barotropic waves and non-linear eddies well.

The governing equations with the sponge layer are now different in the lateral friction term from Equation (2.1). The friction coefficient is constant in the eastern two thirds of the basin and then gradually increase as a cosine function to a maximum value of 75 times that of the constant value at the western boundary. The maximum value was decided numerically to be as large as possible for the desired time step (2 hours) to avoid numerical instability at the boundary between the interior and the sponge layer. The equations for the lateral friction are now

$$A_H \nabla^4 \psi = K_H \nabla^4 \psi + 2\frac{\partial K_H}{\partial x}\frac{\partial}{\partial x}\nabla^2\psi + \frac{\partial^2 K_H}{\partial x^2}\frac{\partial^2 \psi}{\partial x^2} \qquad (2.6)$$

where

$$K_H = A_I + \Pi(x-x_S)A_m(1 + \cos(\frac{\pi}{2}(\frac{x}{x_S} + 1)) \tag{2.7}$$

and the step function Π is

$$\Pi(x - x_S) = \begin{cases} 1 & \text{if } x_W \leq x \leq x_S \\ 0 & \text{if } x_S \leq x < x_E. \end{cases} \tag{2.8}$$

The variables x_E, x_S, andx_W are eastern, sponge and western boundaries, respectively, A_m is the maximum friction coefficient, $7500 m^2 s^{-2}$ and A_I is $100 m^2 s^{-2}$. The cosine function from $\pi/2$ to π is used to make the transition as smooth as possible near the interface.

2.3. Local energetics

Because we are interested in distinguishing the different distributions of eddy kinetic energy, it is useful to derive the local energetics for an arbitrary open region. Pinardi and Robinson (1986) derived such local energetics for quasi-geostrophic systems and applied them to the analysis of the Rossby wave, and normal mode barotropic and baroclinic instability processes. Hall (1986) derived the local energetics after separating the stream function into the mean and eddy components to examine the energy flux of the various regions near the Gulf Stream, using the data generated by the numerical model by Holland (1978).

After multiplying by $H_i \psi_i^*$, and integrating over the domain where $\psi_i^* = \psi_i - \psi_{boundary}$, (2.1) becomes

$$\begin{aligned} \frac{\partial}{\partial t}[\frac{H_i}{2}\int\int(\nabla\psi_i)^2 dxdy] &= H_i\int\int\nabla\cdot(\psi_i^*\frac{\partial}{\partial t}\nabla\psi_i)dxdy + H_i\int\int\psi_i^* J(\nabla^2\psi_i,\psi_i)dxdy + H_i\int\int\beta\psi_i^*\frac{\partial\psi_i}{\partial x}dxdy \\ &+ f_o\int\int w_{i+1}\psi_{i+1}^* dxdy - f_o\int\int w_{i-1}\psi_{i-1}^* dxdy + \frac{f_o H_i}{(H_i+H_{i+2})}\int\int w_{i+1}(\psi_i^* - \psi_{i+2}^*)dxdy \\ &- \frac{f_o H_i}{(H_i+H_{i-2})}\int\int w_{i-1}(\psi_i^* - \psi_{i-2}^*)dxdy - H_i\int\int\psi_i^* F_i\, dxdy - H_i\int\int\psi_i^* D_i\, dxdy, \end{aligned} \tag{2.9}$$

where D_i is lateral friction.

The potential energy equation of the system can be derived by multiplying (2.2) by $f_o^2(\psi^*_{j-1} - \psi^*_{j+1})/g'_j$ and integrating over the area,

$$\frac{\partial}{\partial t}[\frac{f_o^2}{2g'_j}\int\int(\psi_{j-1} - \psi_{j+1})^2 dxdy] = \frac{f_o^2}{g'_j}\int\int(\psi^*_{j-1} - \psi^*_{j+1})\mathbf{J}(\psi_{j-1} - \psi_{j+1}, \psi_j)dxdy$$
$$f_o\int\int w_j(\psi^*_{j-1} - \psi^*_{j+1})dxdy. \qquad (2.10)$$

After further separating the time-dependent variables into a time mean and perturbation part, the various terms for local energetics can be derived and are presented in Table 1. The boundary flux terms are not converted to the divergence form and are integrated using the term expressed in Table 1, because we want to minimize the error due to numerical integration and differentiation. Thus there is no directional information of the boundary terms and they only represent the total boundary flux or work terms. The complete derivations of these local energetics of the open region are found in Hall (1986).

As explained by McWilliams *et al.* (1978), there are the contributions of time trend terms to the energy budgets because the time average of a time derivative does not vanish. But these trend terms are relatively small and thus will not be included in the energy flux diagrams.

3. Results

Three numerical experiments are performed in this study to answer the following questions: How do unstable waves, which grow locally by a baroclinic instability process, interact in the mid-ocean? How do they propagate and in what directions? Do they have any particular wave numbers and periods after equilibrium? Do these waves differ in various areas? If so, how and why?

The first experiment is the basic experiment for this study and uses a mean current speed of 1-2 cm/s which is a typical mean current in the mid-ocean. The second

experiment uses a stronger mean current of 3-4 cm/s to examine the effects of the large growth rates (60 days) at the eastern and southern boundaries. Both experiments use a highly idealized initial mean circulation which gives the same growth rates in the southern return flow area near the eastern boundary and in the western return flow area near the southern boundary region. This closed initial stream function is symmetric in both axes for the surface layer. The gyre center of the middle layer is located close to the northern boundary after the computation of the geostrophic spirals by LN in the North-east Pacific.

It was shown by LN that a three-layer model is not adequate to resolve the spiraling shear in the eastern North Pacific and at least a six-layer model is required to model the realistic shear in the eastern ocean basin. In this paper we examine the three-layer model as one step preceding the costly six-layer model experiment toward the understanding of mid-ocean eddies.

The third experiment intends to show qualitatively the β-effects by comparing two long and thin boxes aligned in the east-westward and south-northward directions, respectively.

Table 4 gives the grid sizes, the parameters used and the initial mean current speeds with their local maximum growth rates. The characteristics of the most unstable waves in the westward return flow region by linear stability analysis are also tabulated.

3.1. Experiment I

This experiment's goal is to model the Northeast Pacific (15°–45° N and 130° – 170° W) for size and for the mean stream function. The initial mean stream functions of the surface and middle layers are shown in Figs. 17.a and 17.b, with the sponge layer indicated.

The maximum local growth rates and propagation directions of the fastest growing

waves by the linear baroclinic instability process are shown in Fig. 17.a with the upper layer initial mean stream function. The fastest growing waves basically propagate toward the mean flow direction of the upper layer, except for the five degrees westward deviation from southward direction at the eastern boundary. The linear growth rates as a function of wave number are presented in Figs. 18.a and 19.a for Point S and for Point E, respectively. The locations of those two points are marked in Fig. 17.b. There are two growth rate maxima on wave number space and these fastest growing waves have different wave characteristics (see Table 3). Figs. 18.b and 19.b. show the vertical structure functions and their vertical phase changes. The longer waves change phase 180 degrees from the surface to the bottom layer and have more baroclinic properties than shorter waves.

After five years of integration using two hours as a time step, the system equilibrates its total kinetic energy and starts to vacillate. Total kinetic energy and potential energy of 15 years as a function of time are shown on Fig. 20.a and 20.b, respectively. In year 3 the upper potential energy starts to release its energy and two years after that year, the kinetic energy reaches its the peak. But lower potential energy increases continuously until the 14th year. The upper two layers become more barotropic while the bottom layer becomes more baroclinic than the initial state.

Fig. 21 shows the stick time plots of eddies in three boundary areas. At Point S and Point E, after five years waves reach the finite amplitude but their characteristics are quite different. At Point S the meso-scale eddies are developed, but at Point E the waves have long periods (600 - 800 days) and the south-northward component is dominant. At Point N, amplitudes of the waves are small (the linear growth rates in this area are very small) and those waves do not show eddy characteristics. For detailed contour of the change between the initial stream function and the mean stream function of the final five years, the differences between those stream functions are presented in Figs. 22.a, 22.b and 22.c for the upper, middle and bottom layer,

respectively. Maximum eddy kinetic energy per unit volume of bottom layer occurs at the largest gradient of the difference field of the bottom layer (see Fig. 26). At the north of this maximum the upper layer is stretched, but at the south of this maximum the upper layer is squeezed.

At Point E, the energy of the north-south velocity is predominant and this shows that only long south-northward waves are generated in this area because there is a boundary condition (no normal flow) at the eastern wall. These long waves are also shown well in the y-t diagram of the eddy field(top figure in Fig. 24) of five years at 100 Km from the eastern boundary. The energy conserving kinetic energy spectra of the upper layer at Point S for the last five years are shown in Fig. 23. The energy of the east-west velocity is smaller than that of the north-south velocity at all frequencies except that with a 200 day period. There is a peak of north-south components of eddy kinetic energy having periods of 300 days and it indicates a westward propagation of eddies at this period. The westward propagation of eddies is well shown in the phase diagrams for the eddy field for the x, t plane (Fig. 25) and y, t plane at various locations along the x axis (Fig. 24). Fig. 24 (progressive y-t phase diagram) is made by following way: We calculate the average westward propagation speed of this wave from an x-t phase diagram (Fig. 25) at 400 Km from the southern boundary, and it is 1.1 Km/day. From this propagation speed we align the y-t phase diagram with a 360 day interval for a 400 Km longitudinal distance, and then we are able to see the evolution of the waves with time and space. These waves are growing during their propagation to the west. This progressive y-t diagram at various longitudes from 100 Km to 3000 Km from the eastern boundary shows that there is one predominant wave in the southern boundary area with a wave length of 375 Km and a period of 340 days which is similar to the second most unstable wave. The finally developed waves in both boundary regions are presented in linear stability diagrams (Fig. 18.a and 19.a).

The distribution of the five-year means of eddy kinetic energy per unit area for the

bottom layer is shown in Fig. 26. There is an eddy kinetic energy maximum at 330 Km from the southern boundary, near the center of the westward propagating wave train. The eddies grow until they reach 2000 Km from the eastern boundary and decay when they propagate further to the west. Eddy kinetic energies are concentrated around this maximum area, and there is hardly any eddy kinetic energy at the eastern boundary even though the linear growth rates for both regions are the same.

Figs. 27.a and 27.b show the energy flux diagram for the eastern boundary region and the southern boundary region marked by dotted areas in Fig. 26. In the eastern region the energy converted from the mean kinetic energy to mean potential energy goes out from the boundary and there is little conversion from mean potential energy to eddy potential energy (whose conversion process is the main baroclinic instability process). The main mean kinetic energy flux in this region is the pressure work done by the β-effect along the boundary. All the energy flux from the mean forcing goes out from the area by the pressure work done by the β-effect and by the outward boundary flux of mean potential energy by the mean flow on the interface. On the other hand, in the southern region the largest energy source for the region is the boundary influx of mean kinetic energy by the pressure work done by the β-effect and the boundary influx of the mean potential energy by mean flow. There is a large conversion from mean potential energy to eddy potential energy, and consequently a large conversion from eddy potential energy to eddy kinetic energy. Why are they different? We will discuss these differences in greater detail in Section 4.

3.2. Experiment II

This experiment is the same as Experiment I except that the maximum growth rates are two times as large as in Experiment I at the eastern and the southern boundary. The linear stability diagram for Point S and Point E with the vertical structure function and their phase for two growth rate maxima are presented in Figs. 28 and 29,

respectively. The wave characteristics of these two most unstable waves are tabulated in Table 2; their wave lengths and periods become shorter compared to those in Experiment I, but vertical structure functions and their phases remain unchanged.

Using the time step (two hours), the system reaches statistical equilibrium after three years of integration (see Figs. 30.a and 30.b). The upper potential energy is releasing its energy until the fifth year but lower potential energy is increasing. Fig. 31 shows the stick time plots for three regions and the eddy development at the eastern boundary region. The mean stream function of the final five years are shown in Fig. 32.a, 32.b and 32.c for the upper, middle and lower layers, respectively. In Fig.32.a the propagation directions and the growth rates of the most unstable waves using final five year mean flow are also presented. In the surface layer, there are significant mean flow changes in the southern half of the gyre; the zonal current becomes weaker ($\approx$ 1 cm/s) and meridional current becomes stronger ($\approx$ 0.5 cm/s) than the initial flow. The mean stream function of the middle layer is changed significantly in the southern half of the gyre. The long (3000 Km zoanlly) and thin (240 Km meridionally) counterclockwise mean circulation is formed in the bottom layer along the southern boundary. Two peak frequency bands which have different wave characteristics are found in the energy preserving eddy energy spectra at Point S for each layer (Figs. 36.a, b and c). In the southern region the eddy kinetic energy density of the east-west flow is larger in the longer period band (longer than 150 days) than that of the north-south flow. But it is smaller in the shorter period band (shorter than 150 days). This is from the waves of short periods only traveling westward as shown in the phase diagram in the y, t plane (Fig. 33.), which is band passed for periods between 115 days and 150 days. The waves of short period bands (80 - 100 days) have similar energy in all three layers and show more barotropic properties than the waves of longer period bands (longer than 200 days). At the eastern region there is only one peak at the period of 200 days and the east-west component of eddy kinetic energy is bigger than north-south component at all

frequencies (Fig. 37).

The short period waves (periods of 120 days) show similar periods to the first most unstable wave (103 days) from the linear stability analysis. They have an average phase speed of 2.1 Km/day and wave length of 285 Km which is much longer than that of the first most unstable waves, which is 192 Km. Long period waves (periods of 200 days) also have similar wave periods to the second most unstable waves which have the period of 225 days. The average phase speed of these long waves is 1.1 Km/day southward and 1.8 Km/day westward, and their wave lengths are 422 Km, which is much longer than the wave length of the second most unstable waves (324 Km). The finally developed waves in both boundary regions are presented in Fig. 28.a and 29.a. The difference between developed waves and waves predicted by linear analysis is partly due to the effects of the propagated waves from the eastern boundary areas. When locally generated short waves interact with propagating long waves, the phase speed of resulting waves becomes faster than that of locally generated waves if their periods are unchanged. These phase speed changes are well shown in the x-t diagram (Fig. 35). The progressive y-t diagrams of the long waves which have periods longer than 200 days are presented in Fig. 34 and propagate south-westward. All these waves are propagating and vacillating (growing and decaying) at the same time.

The distribution of the eddy kinetic energy per unit area for the bottom layer is shown in Fig. 38. Unlike Experiment, I the eddy kinetic energy per unit area is distributed all over the southern half of the basin except near the eastern boundary and the maxima occur near 100 Km from the southern boundary and 2000 Km from the eastern boundary. Because the eddies can grow and decay several times before they reach the sponge layer, there are several local eddy kinetic energy per unit area maxima. Near the eastern boundary the eddy kinetic energy per unit area is still much smaller than near the southern boundary.

The energy flux diagrams are found in Figs. 39.a and 39.b for the southern

boundary region and the eastern boundary region, respectively. In this experiment there is a baroclinic instability process at the eastern boundary, but this conversion from mean potential energy to eddy potential energy comes largely from the boundary process rather than internal conversion between mean and eddy potential energy as shown on following equations.

$$\bar{P}_j \rightarrow P_j' = -\frac{f_o^2}{g'}\int\int\Big(\frac{\partial}{\partial x}\overline{[u_j'(\bar{\psi}_{j-1}-\bar{\psi}_{j+1})(\psi_{j-1}'-\psi_{j+1}')]}+\frac{\partial}{\partial y}\overline{[v_j'(\bar{\psi}_{j-1}-\bar{\psi}_{j+1})(\psi_{j-1}'-\psi_{j+1}')]}\Big)\,dxdy$$

$$+\frac{f_o^2}{g'}\int\int\Big(\overline{u_j'(\psi_{j-1}'-\psi_{j+1}')}\frac{\partial}{\partial x}(\bar{\psi}_{j-1}-\bar{\psi}_{j+1})+\overline{v_j'(\psi_{j-1}'-\psi_{j+1}')}\frac{\partial}{\partial y}(\bar{\psi}_{j-1}-\bar{\psi}_{j+1})\Big)\,dxdy \qquad (3.1)$$

$$P_j' \rightarrow \bar{P}_j = -\frac{f_o^2}{g'}\int\int\Big(\overline{u_j'(\psi_{j-1}'-\psi_{j+1}')}\frac{\partial}{\partial x}(\bar{\psi}_{j-1}-\bar{\psi}_{j+1})+\overline{v_j'(\psi_{j-1}'-\psi_{j+1}')}\frac{\partial}{\partial y}(\bar{\psi}_{j-1}-\bar{\psi}_{j+1})\Big)\,dxdy \qquad (3.2)$$

The mean potential energy between the upper two layers fluxes out from the boundary all the energy converted from the mean kinetic energy of the upper two layers, the same as in Experiment I. In the southern region, however, there is large conversion locally from mean to eddy potential energy. The middle layer feeds the eddy kinetic energy to the upper layer and the bottom layer in the eastern boundary region, but at the southern boundary region there is a large eddy energy conversion from the middle layer to the bottom layer and from the upper layer to the middle layer. The eddy kinetic energy is dissipated mainly by lateral friction in the southern region, but the pressure work done by the β-effect at the boundary is nearly as important at the eastern boundary. In summary, it is less unstable in the eastern region than in the southern region even though the growth rates are the same in both regions, and the boundary fluxes in the conversion from mean to eddy potential energy play a very important role in the finite growth of the eddy field.

3.3. Experiment III

This experiment is performed to show the difference between the long north-south flow region and the east-west flow region. Because of the β-effect, the most unstable waves formed by the mean current propagate westward so that waves propagate out of the

north-south current system, i.e. to the less unstable regions. But in the east-west flow region the waves propagate with the flow direction and then to the more unstable region (i.e. at the center), therefore they grow. Fig. 40 shows the formation of eddies along the southern boundary for the east-westward long box experiment for three years. During the first year eddies are formed along the southern boundary and have similar amplitude in the western return flow region except near the eastern boundary. The amplitudes of eddies developed in this experiment is very small compared to Experiment I even though the maximum local growth rates are bigger than Experiment I (see Table 2). And also eddies are slowly decaying from the second year. This smaller eddy development indicates that the propagating waves from the eastern and northern areas are very important for the formation of the equilibrated eddy field.

On the other hand, all eddies are aligned along the interface between sponge layers and the southward return flow area in the north-south long box experiment (Fig. 41) in the first year of growth. In the third year eddies are nowhere to be found.

These two experiments clearly show the local growth rates are not related to the finite amplitude growth of eddies but the propagation of eddies, and consequently interaction of eddies between locally generated waves with non-local propagating waves are the most important dynamics for the equilibrated eddy field in the eastern ocean basin.

4. Discussion

Because of the β-effect, eddies grow in the westward mean flow region but in the southward mean flow region eddies are propagating out of the region and do not grow. The unstable waves generated in the Northeast Pacific generally propagate southwestward and the waves are growing during propagation. These wave properties make the southern region an eddy rich area but, in the eastern region, there is little eddy activity. In the northern region, not only are the local growth rates small for the east-

ward mean flow, but also the unstable waves propagate south-westward and these make the northern region the smallest eddy kinetic energy area.

The energy production rates by the energy conversion from mean to eddy potential energy, the energy fluxes by the pressure work and the eddy kinetic energy which are integrated over depth for Experiment II are shown in Fig. 42.a in the various region. As explained in Section 3.2, the production of energy by the baroclinic instability is mainly balanced by the boundary flux and the dissipation. In the north-eastern corner there is little conversion of mean potential energy to eddy potential energy and there is net energy leak by the pressure work. In the south-eastern corner, the energy production is large but half of that energy production fluxes out of the region by the pressure work. On the other hand, there is large influx of energy by the pressure work in the southern regions. These combined effect of large boundary influx and the energy production make the southern region the area of the largest eddy kinetic energy. Because the energy flux by the waves is expressed by the pressure work along the boundary it clearly shows the effect of the propagating waves quantitatively. Fig. 42.b shows the eddy kinetic energy as a function of the net energy production (energy conversion from mean to eddy potential energy plus boundary flux by the pressure work). The eddy kinetic energy has a linear relationship with the net energy production. These two figures well demonstrate that the local baroclinic instability, the boundary energy flux by the propagating waves and the dissipation play the major role in the eddy dynamics in the eastern ocean basin.

The linear stability analysis shows growth rates as a function of the wave number, but cannot show which particular waves ultimately develop because of the boundary conditions and wave energy input from outside the region. The north-south wave number (l) becomes very small by the boundary condition (no normal flow) and east-west wave number (k) is $0.75 \times 10^{-5} m^{-1}$ near the eastern boundary in the case of Experiment II. The $k = -0.75 \times 10^{-5} m^{-1}$ is the smallest possible wave number which is

determined by the mean flow, thus large portion of wave number band including the first local growth rate maximum at high wave number cannot be unstable (see Fig. 29). Near the southern boundary, however, it is quite unstable in the broad wave number band even though l is very small by the boundary condition (see Fig. 28).

There are two dominant waves with different characteristics in the southern regions. The periods of these waves match the two most unstable waves by the linear stability analysis; only the fastest growing waves dominate the eddy field in this area. But the wave lengths become longer than those predicted by the linear analysis partly because of the effects of the propagated waves from the eastern boundary region (the most unstable waves in the eastern boundary region have much longer wave lengths depending upon the distance from the boundary). Haidvogel and Holland (1978) showed that the linear stability analysis correctly identified the finally developed baroclinic waves in the numerical experiment by Holland (1978). But their analysis was focused on the strong eastward jet area and used an instantaneous field rather than a mean field. The three year-long current meter observations (Niiler and Hall, 1987) at 28°N and 152°W clearly show these two waves on their spectral analysis (Fig. 43). They have shorter periods than the result of Experiment II but when the vertical resolution of the model is increased, the most unstable waves become shorter period waves (see Fig. 15 in LN).

Is there a third wave to form resonant interaction for these two dominant unstable waves? A third wave should propagate north-eastward to form a resonant triad (Pedlosky, 1979). We were able to trace the northward propagating waves which have periods between 200 days and 160 days, but there are no eastward propagating waves and also these northward propagating waves exist only near the center of the southern gyre. These two waves are simply the most unstable waves by the baroclinic instability, and they do not form a resonant interaction as stable waves do.

The final mean fields are changed significantly in the high eddy activity area for both experiments. These alterations will ultimately change stability properties (see Fig.

32.a). In the case of Experiment II, $\bar{u}$ (-2.6 cm/s) becomes smaller than $\bar{u}[t=0]$ (3.8 cm/s) but $\bar{v}$ changes significantly from 0 cm/s to 0.6 cm/s at Point S. The maximum growth rates become smaller (from 61 days to 116 days) and the direction of the most unstable waves changes from 180° to 160° (Fig. 44.a). But there are no signs of northward propagating waves in the southern boundary area during the final five years. At Point E the stability properties are only slightly changed (Fig. 44.b). Because of the significant change of the zonal and meridional mean currents in the strong eddy activity area (southern region), the linear stability analysis using these final mean field quite depends upon the position where the mean flow is evaluated. The eigenvalue method, which was used by Haidvogel and Holland (1978), can be used for the mean field as a function of space but it is beyond the scope of this paper.

The zonally averaged eddy kinetic energy per unit volume is shown in Fig. 45, with the measured eddy kinetic energy in the Northeast Pacific by Niiler *et al.* (1987). There are several fluctuations because of the wave train being parallel to the southern boundary but generally the eddy kinetic energy per unit volume increases to the south - a phenomenon which agrees with the measurements.

The six-layer model with more realistic mean fields is planned for modelling the realistic mid-ocean eddy fields. This increase in vertical resolution in the numerical model will make the developed eddy field more realistic, i. e., the subsurface eddy kinetic energy maxima (Cox, 1986 and LN) and eddies of realistic time and length scale.

Symbol	Term	Physical Process
$\overline{K}_i \rightarrow F$	$-H_i \int\int \overline{\psi}_i^{\,*} F_i \; dxdy$	Work done by initial forcing
$\overline{K}_i \rightarrow \overline{u}_i \overline{K}_i$	$-H_i \int\int [\frac{\partial}{\partial x}\overline{u}_i \overline{K}_i + \frac{\partial}{\partial y}\overline{v}_i \overline{K}_i)] \; dxdy$	Mean flux of mean K. E.
$K_i' \rightarrow u_i' K_i'$	$-H_i \int\int [\frac{\partial}{\partial x}\overline{u_i' K_i'} + \frac{\partial}{\partial y}\overline{v_i' K_i'}] \; dxdy$	Eddy flux of eddy K. E.
$K_i' \rightarrow \overline{u}_i K_i'$	$-H_i \int\int [\frac{\partial}{\partial x}\overline{\overline{u}_i K_i'} + \frac{\partial}{\partial y}\overline{\overline{v}_i K_i'}] \; dxdy$	Mean flux of eddy K. E.
$\overline{K}_i \rightarrow D$	$H_i \int\int A_H \overline{\psi}_i^{\,*} \nabla^4 \overline{\psi}_i \; dxdy$	Frictional dissipation by mean field
$K_i' \rightarrow D$	$H_i \int\int A_H \overline{\psi_i^{\,*\,\prime} \nabla^4 \psi_i'} \; dxdy$	Frictional dissipation by eddy field
$\overline{K}_i \rightarrow f$	$H_i \int\int \beta \overline{\psi}_i^{\,*} \frac{\partial}{\partial x}\overline{\psi}_i \; dxdy$	Mean pressure work due to β effect
$K_i' \rightarrow f$	$H_i \int\int \beta \overline{\psi_i^{\,*\,\prime} \frac{\partial}{\partial x}\psi_i'} \; dxdy$	Eddy pressure work due to β effect
$\overline{K}_i \rightarrow W$	$H_i \int\int [\frac{\partial}{\partial x}(\overline{\psi}_i^{\,*} \frac{d}{dt}\overline{u}_i) + \frac{\partial}{\partial y}(\overline{\psi}_i^{\,*} \frac{d}{dt}\overline{v}_i)] \; dxdy$	Mean pressure work due to advection of mean field
$K_i' \rightarrow W_a$	$H_i \overline{\int\int [\frac{\partial}{\partial x}(\psi_i^{\,*\,\prime} \frac{\partial}{\partial t}u_i') + \frac{\partial}{\partial y}(\psi_i^{\,*\,\prime} \frac{\partial}{\partial t}v_i')]} \; dxdy$	Eddy pressure work due to accelaration of eddy field
$K_i' \rightarrow W$	$H_i \overline{\int\int [\frac{\partial}{\partial x}(\psi_i \frac{d}{dt}u_i) + \frac{\partial}{\partial y}(\psi_i \frac{d}{dt}v_i)]} \; dxdy$	Eddy pressure work due to advection
	$-(\overline{K}_i \rightarrow W) - (K_i' \rightarrow W_a)$	of mean and eddy field
$\overline{K}_i \rightarrow K_i'$	$-H_i \int\int \overline{u}_i [\frac{\partial}{\partial x}\overline{u_i'^2} + \frac{\partial}{\partial y}\overline{u_i' v_i'}]$	Flux and conversion of mean to eddy K. E.
	$+ \overline{v}_i [\frac{\partial}{\partial x}\overline{u_i' v_i'} + \frac{\partial}{\partial y}\overline{v_i'^2}] dxdy$	
$K_i' \rightarrow \overline{K}_i$	$-H_i \int\int [\overline{u_i'^2}\frac{\partial}{\partial y}\overline{u}_i + \overline{u_i' v_i'}(\frac{\partial}{\partial y}\overline{u}_i + \frac{\partial}{\partial x}\overline{v}_i)$	Flux and conversion of eddy to mean K. E.
	$+ \overline{v_i'^2}\frac{\partial}{\partial y}\overline{v}_i] dxdy$	
$\overline{K}_i \rightarrow \overline{K}_{i\pm 2}$	$+f_o \int\int \overline{\psi}_{i\pm 1}^{\,*} \overline{w}_{i\pm 1} \; dxdy$	Conversion of mean K. E. between two layers
$K_i' \rightarrow K_{i\pm 2}'$	$+f_o \int\int \overline{\psi_{i\pm 1}^{\,*\,\prime} w_{i\pm 1}'} \; dxdy$	Conversion of eddy K. E. between two layers
$\overline{K}_i \rightarrow \overline{P}_{i\pm 1}$	$\mp \frac{f_o}{H_i + H_{i\pm 2}} \int\int H_i (\overline{\psi}_i^{\,*} - \overline{\psi}_{i\pm 2}^{\,*}) \overline{w}_{i\pm 1} \; dxdy$	Conversion of mean K. E. to mean P. E.
$P_{i\pm 1}' \rightarrow K_i'$	$\pm \frac{f_o}{H_i + H_{i\pm 2}} \int\int H_i \overline{(\psi_i' - \psi_{i\pm 2}') w_{i\pm 1}'} dxdy$	Conversion of eddy P. E. to eddy K. E.
$\overline{P}_j \rightarrow \overline{u}_j \overline{P}_j$	$-\int\int [\frac{\partial}{\partial x}\overline{u}_j \overline{P}_j + \frac{\partial}{\partial y}\overline{v}_j \overline{P}_j] \; dxdy$	Mean flux of mean P. E.
$P_j' \rightarrow u_j' P_j'$	$-\int\int [\frac{\partial}{\partial x}\overline{u_j' P_j'} + \frac{\partial}{\partial y}\overline{v_j' P_j'}] \; dxdy$	Eddy flux of eddy P. E.
$P_j' \rightarrow \overline{u}_j P_j'$	$-\int\int [\frac{\partial}{\partial x}\overline{\overline{u}_j P_j'} + \frac{\partial}{\partial y}\overline{\overline{v}_j P_j'}] \; dxdy$	Mean flux of eddy P. E.
$\overline{P}_j \rightarrow P_j'$	$-\frac{f_o^2}{g'} \int\int (\overline{\psi}_{j-1}^{\,*} - \overline{\psi}_{j+1}^{\,*}) \mathrm{J}(\overline{\psi_{j-1}', \psi_{j+1}'}) \; dxdy$	Flux and conversion of mean to eddy P. E.
$P_j' \rightarrow \overline{P}_j$	$-\frac{f_o^2}{g'} \int\int \overline{(\psi_{j-1}' - \psi_{j+1}') \mathrm{J}(\overline{\psi}_{j-1} - \overline{\psi}_{j+1}, \psi_j')} \; dxdy$	Flux and conversion of eddy to mean P. E.

Table 3. Energy equation symbols and their terms as they are referred to in energy flux diagram. $\frac{d}{dt}$ is the total derivative with respect to time following individual fluid elements.

Experiment	Grid Size	Mean Current	Maximum Growth Rate	The First Most Unstable Wave		The Second Most Unstable Wave	
				Length	Period	Length	Period
I	300×150	0 - 2 cm/s	160 Days	175 Km	126 Days	342 Km	295 Days
II	300×150	0 - 4 cm/s	60 Days	192 Km	103 Days	324 Km	225 Days
III.1	250×40	0 - 3 cm/s	105 Days				
III.2	40×250	0 - 3 cm/s	90 Days				

Table 4. Summary of experiments discussed in this study. Note that all cases used $f_o = 1.0 \times 10^{-4}$ s^{-1}, $\beta = 2 \times 10^{-11}$ m^{-1} s^{-1}, $g'_2 = 0.014$ m s^{-2}, $g'_4 = 0.007$ m s^{-2}, $H_1 = 350$ m, $H_3 = 650$ m and $H_5 = 4000$ m.

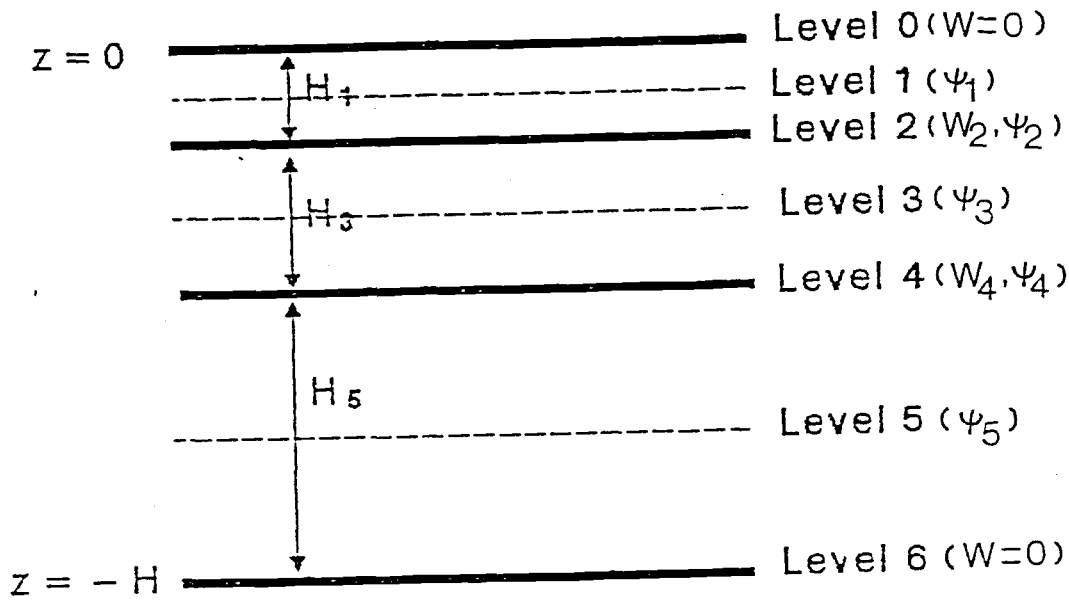

Fig. 16. A schematic diagram for the vertical structure of the three-layer quasi-geostrophic model.

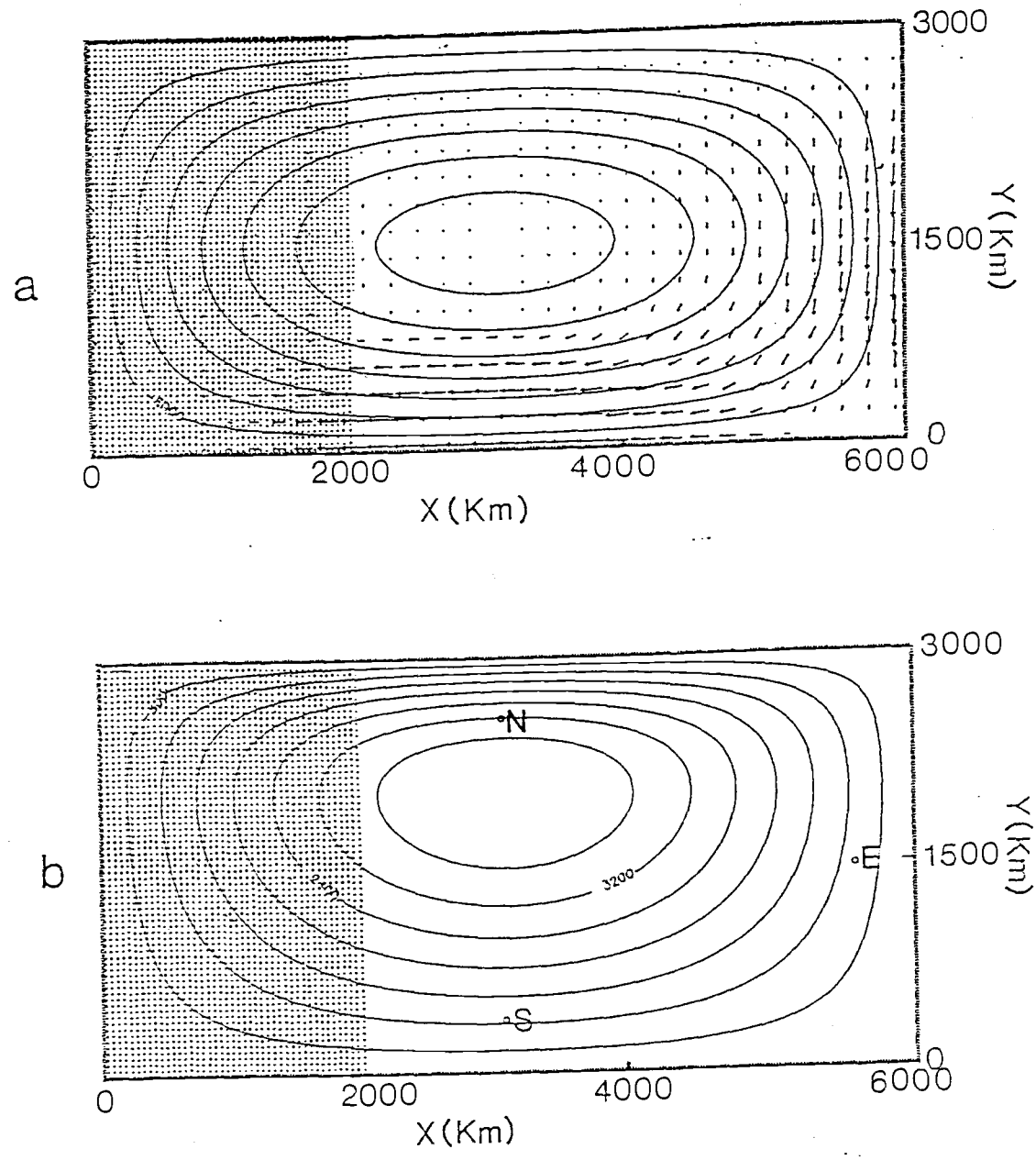

Fig. 17.a. Initial stream function of upper layer (contour interval, CI=3000) with the propagation direction and the growth rates of the most unstable waves from linear stability analysis. The dotted area represents the sponge layer.

Fig. 17.b. Initial stream function of the middle layer (CI=800). Two positions, S and E, are marked for various analyses.

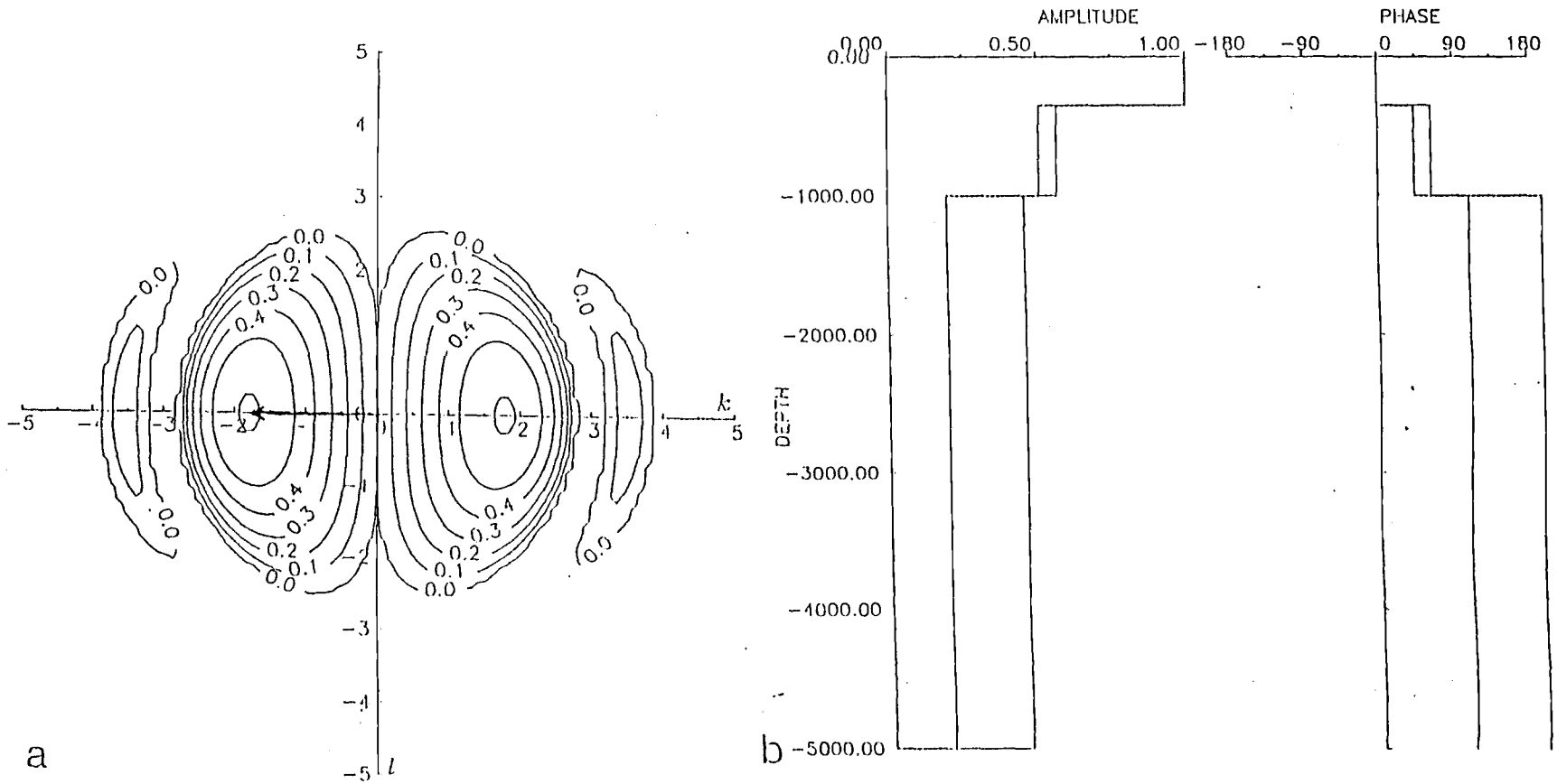

Fig. 18.a. Linear growth rate contours in unit of $10^{-7}s^{-1}$ of the unstable waves at Point S for Experiment I. The finally developed wave in the Experiment I is also presented. The wave number has a unit of $10^{-5}m^{-1}$.

Fig. 18.b. Amplitude and phase changes of the first most unstable wave (solid line, the local growth rate maximum in high wave number band) and the second most unstable wave (dotted line, the local growth rate maximum in low wave number band) for Experiment I.

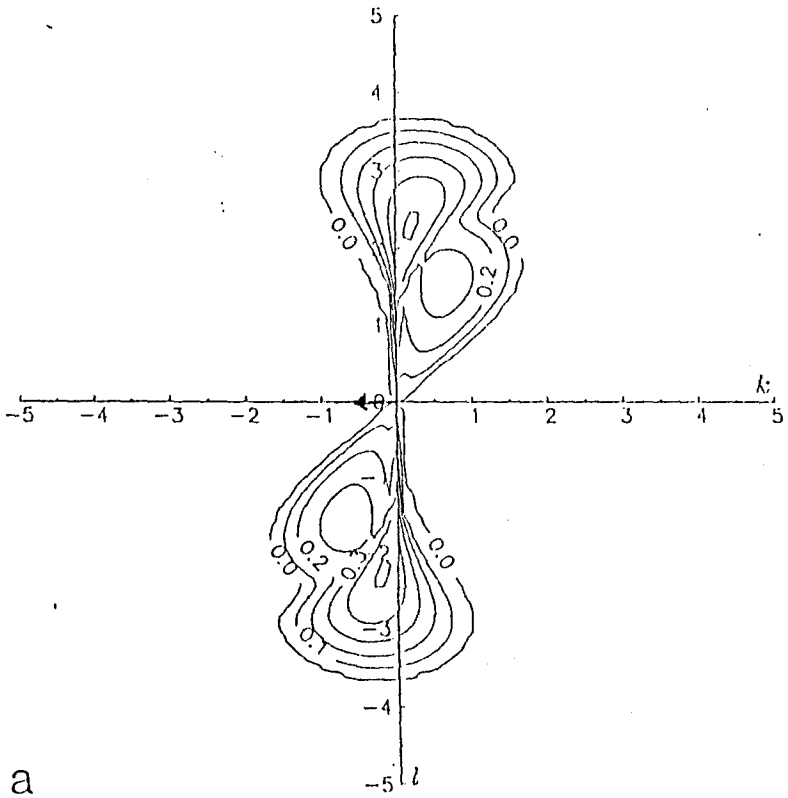

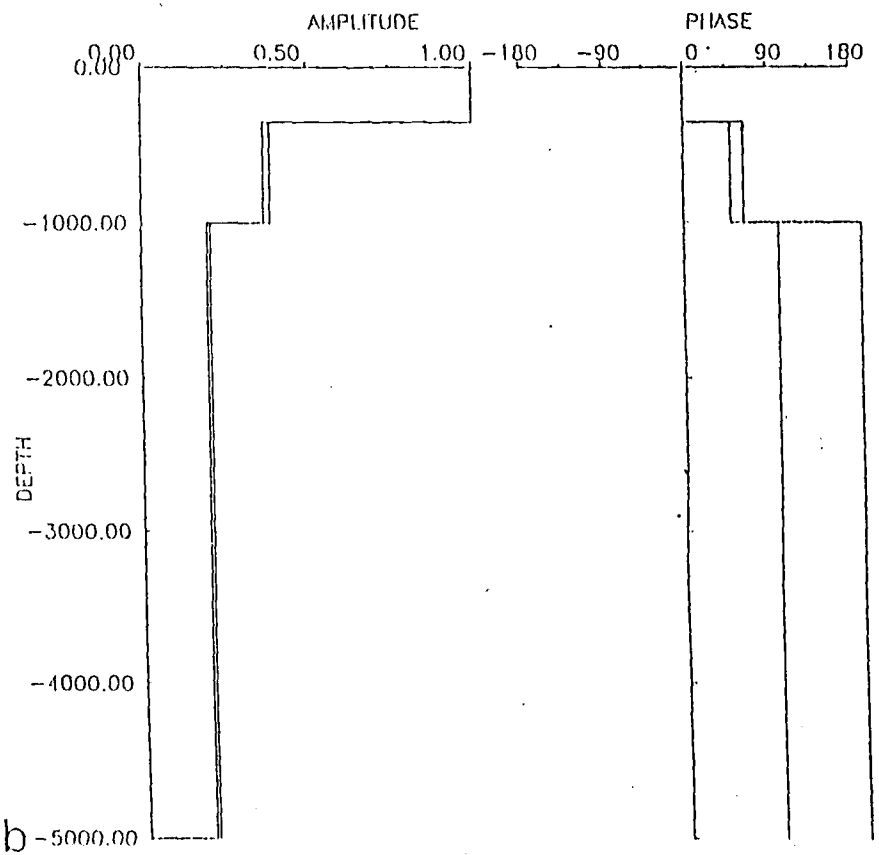

Fig. 19.a. Linear growth rate contours at Point E for Experiment I. the finally developed wave is also presented. The units are the same as Fig. 18.a.

Fig. 19.b. Amplitude and phase changes of the first most unstable wave (solid line) and the second most unstable wave (dotted line) for Experiment I.

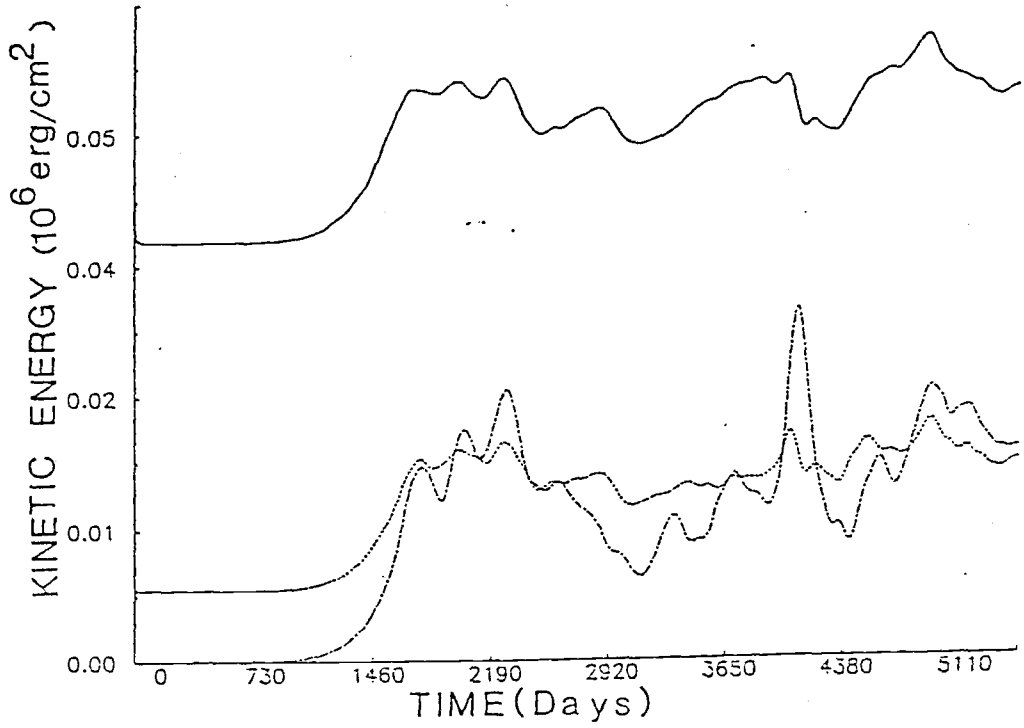

Fig. 20.a. Total kinetic energy per unit area of the surface layer (solid line), the middle layer (dotted line) and the bottom layer (dot-dashed line) as a function of time for Experiment I.

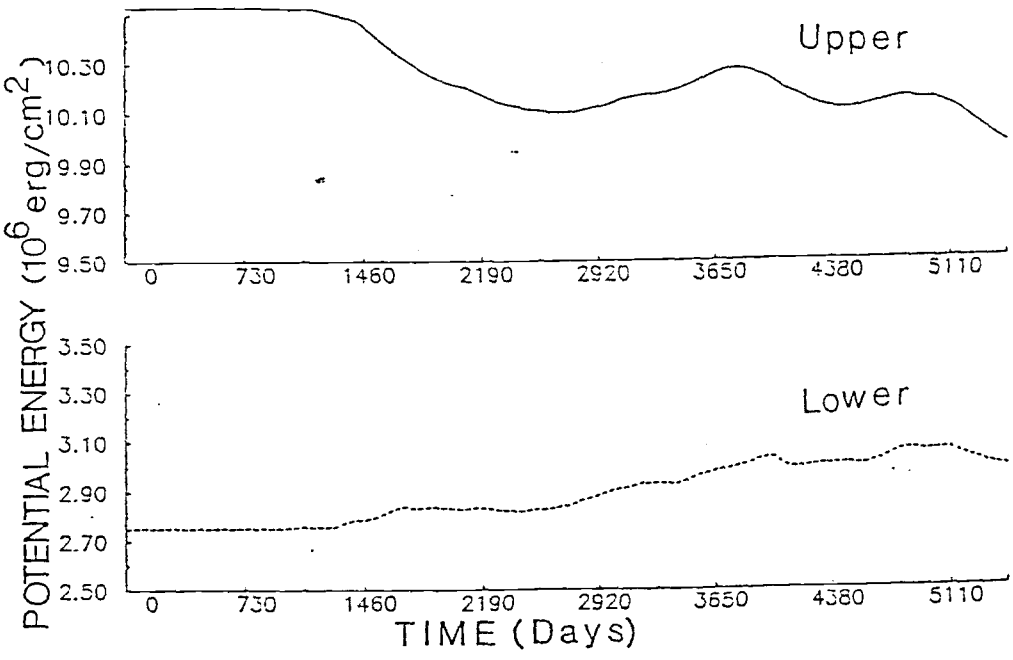

Fig. 20.b. Total potential energy per unit area at the upper interface (solid line) and at the lower interface (dotted line) as a function of time for Experiment I.

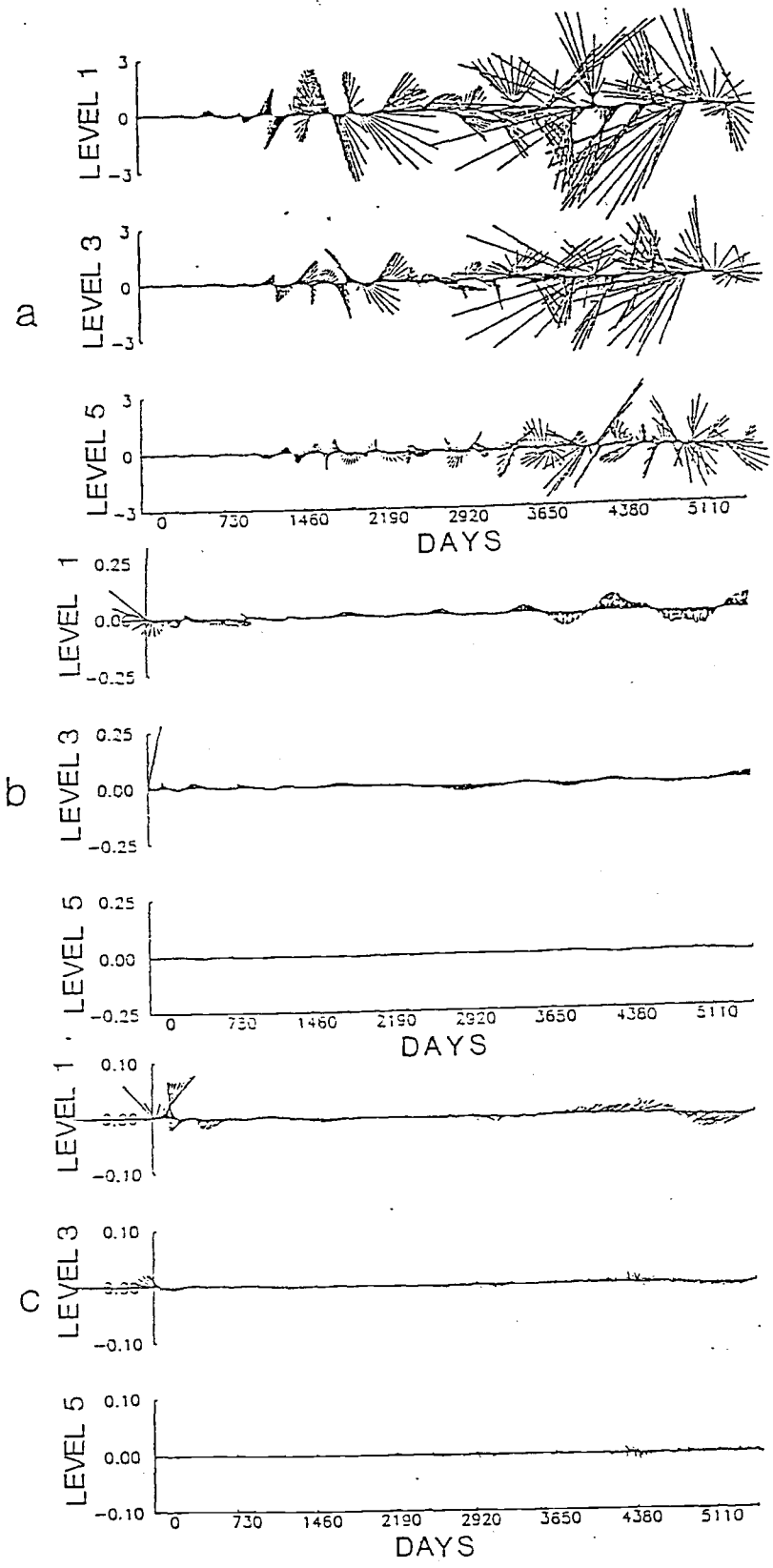

Fig. 21. Stick time plot of eddy currents (a) at Point S, (b) at Point S and (c) at Point N. The y-axes have units of cm/s.

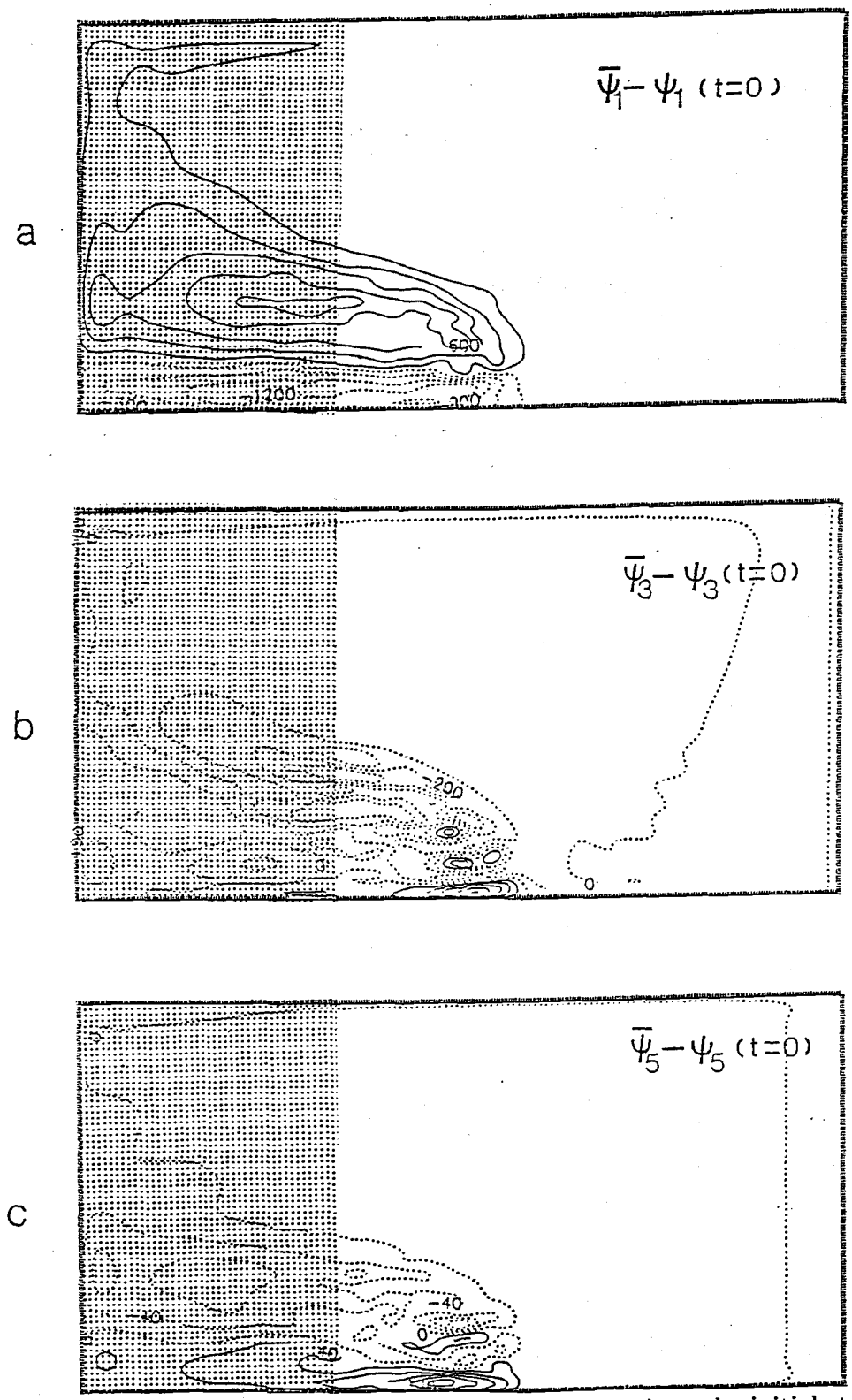

Fig. 22. The mean stream function of the last five years minus the initial stream function (a) for the surface layer (CI=300), (b) for the middle layer (CI=100) and (c) for the bottom layer (CI=40). The dotted lines have the negative contour values.

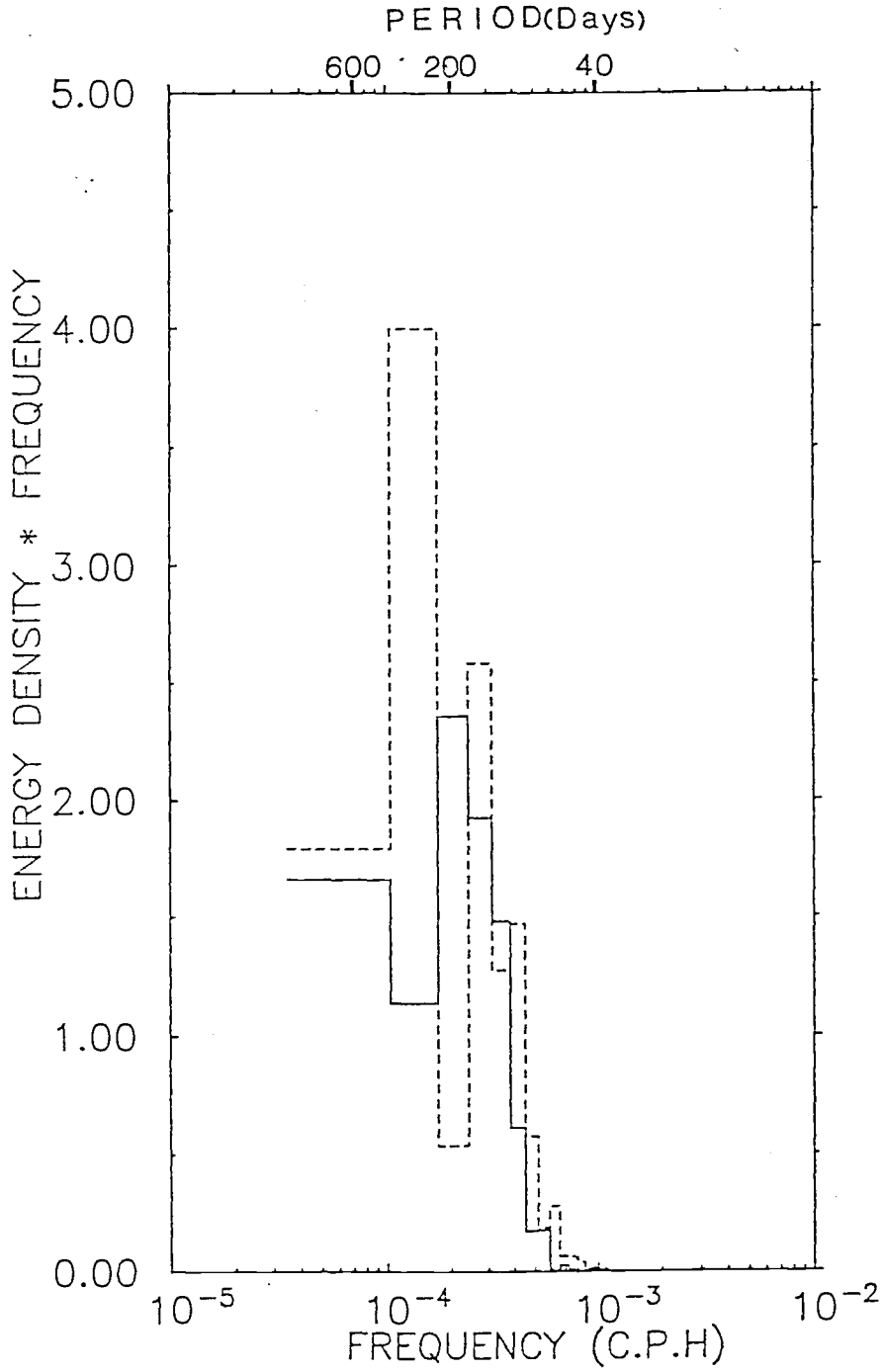

Fig. 23. Energy preserving spectra of the east-west component of the current (solid line) and the north-south component (dotted line) at Point S. The unit is $cm^2\ sec^{-2} \times$ C.P.H.

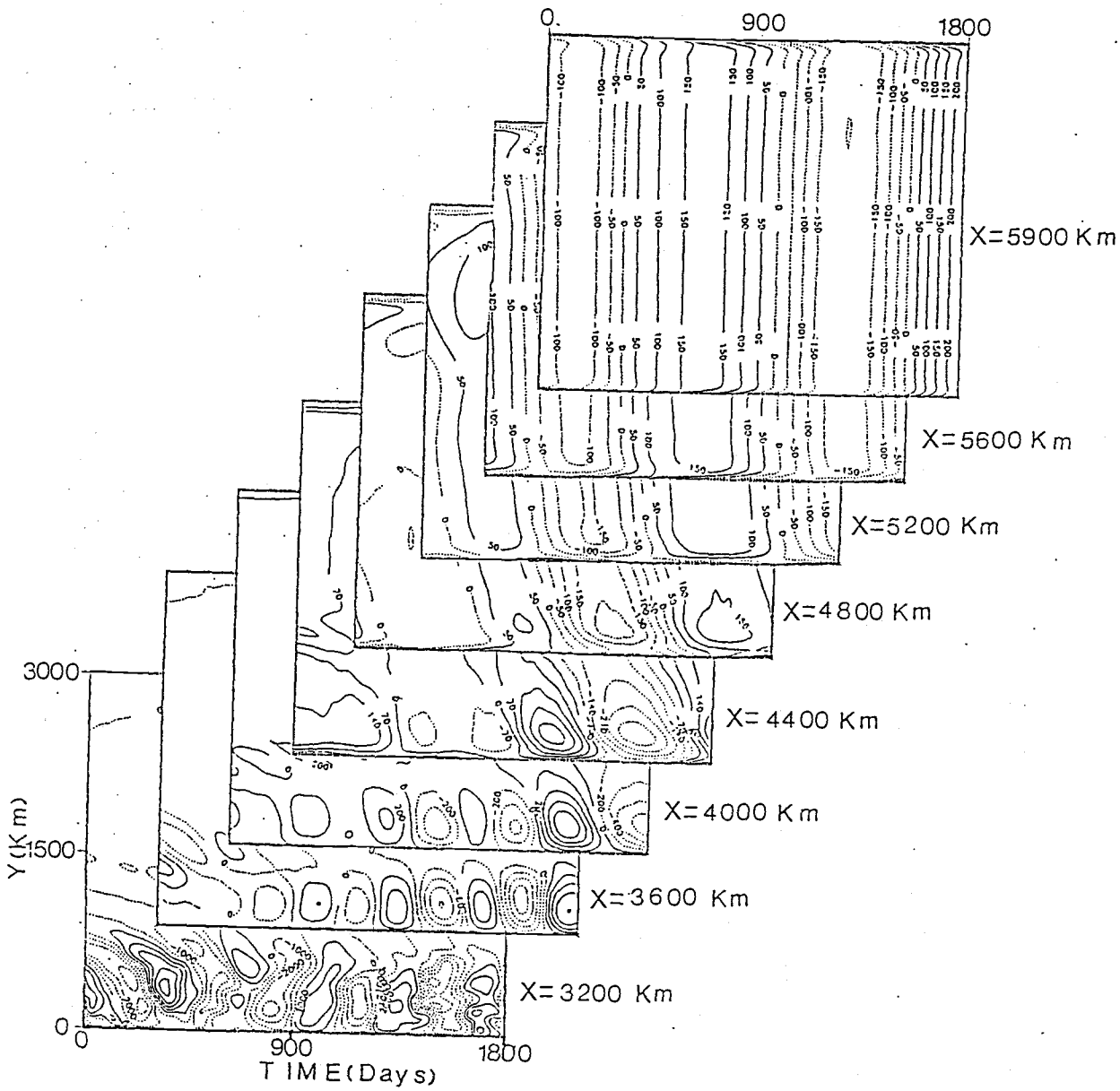

Fig. 24. Progressive phase diagram (y vs time) at various locations along the x-axis for the last five years in Experiment I.

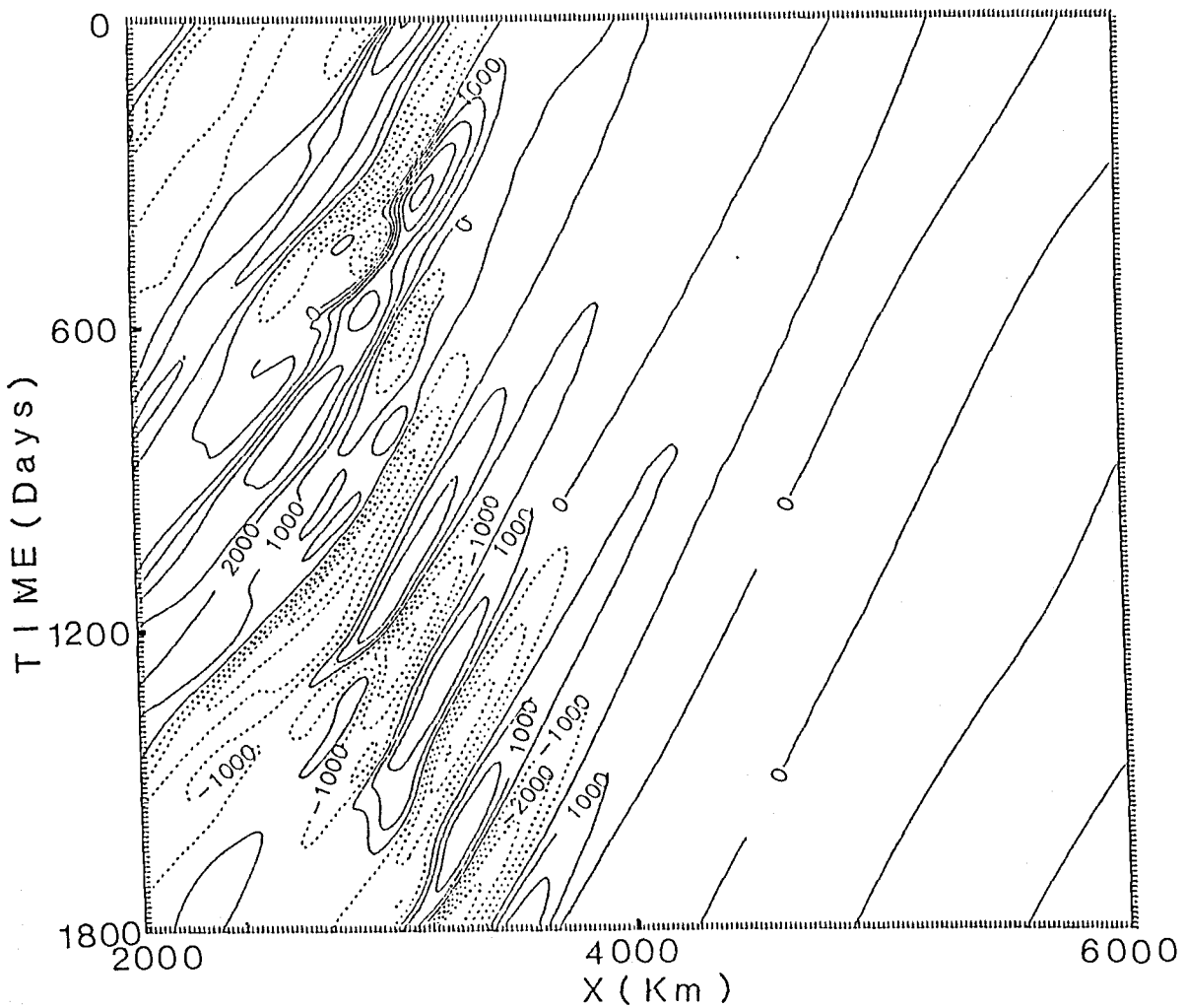

Fig. 25. The phase diagram (x vs time) at 400 Km from the southern boundary for Experiment I (CI=1000).

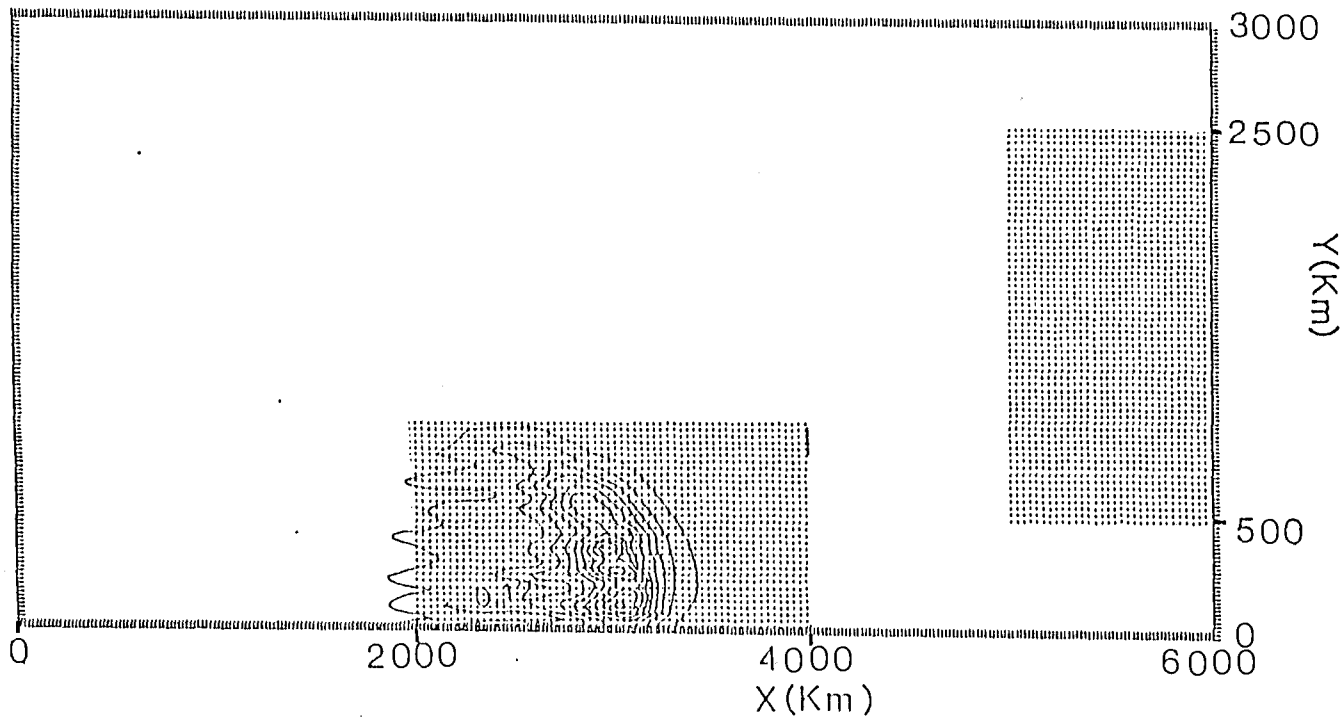

Fig. 26. The eddy kinetic energy per unit area distribution of the bottom layer for the last five years of Experiment I (CI=0.06 and maximum eddy kinetic energy = 0.6×10^{6} ergs cm^{-2}). The two dotted area represent two regions for local energy flux analysis.

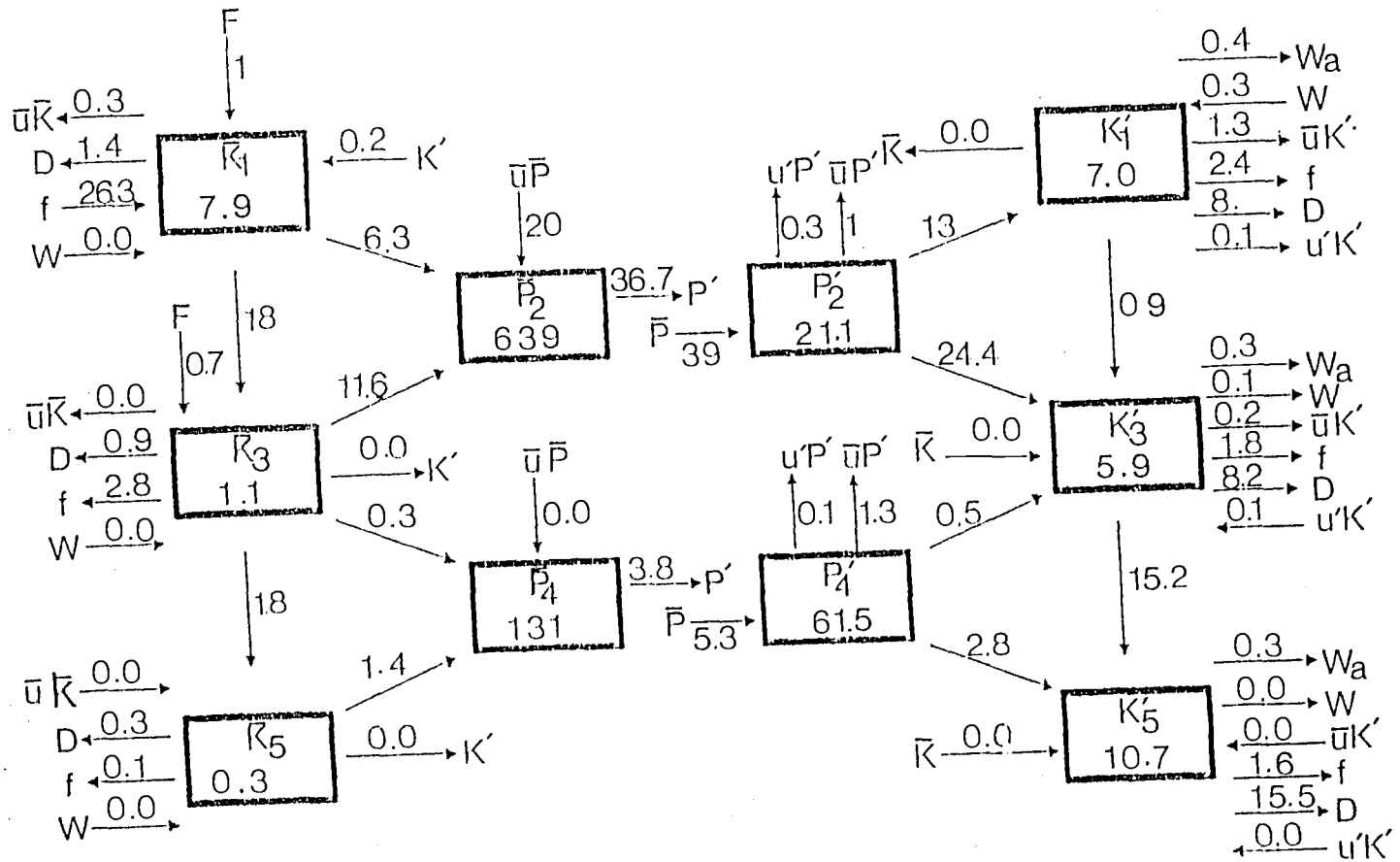

Fig. 27.a. The local energy flux diagram of the southern boundary region for Experiment I. The numbers within the boxes are the energy levels in units of 10^4 ergs cm^{-2} and the numbers on the arrows are the various energy fluxes in units of 10^{-3}cm^{-2}s^{-1} tabulated in Table 3.

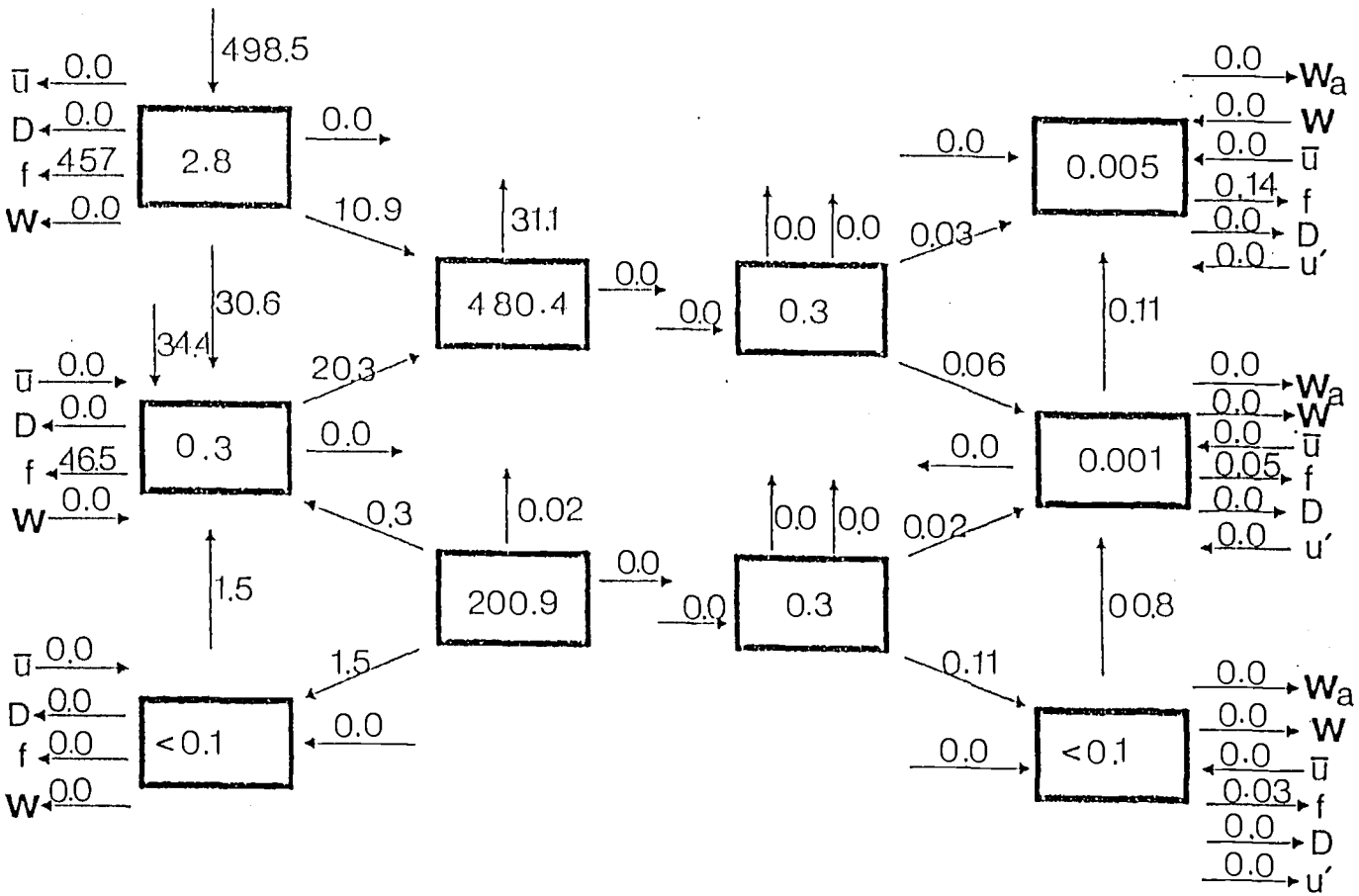

Fig. 27.b. The energy flux diagram of the eastern boundary region for Experiment II.

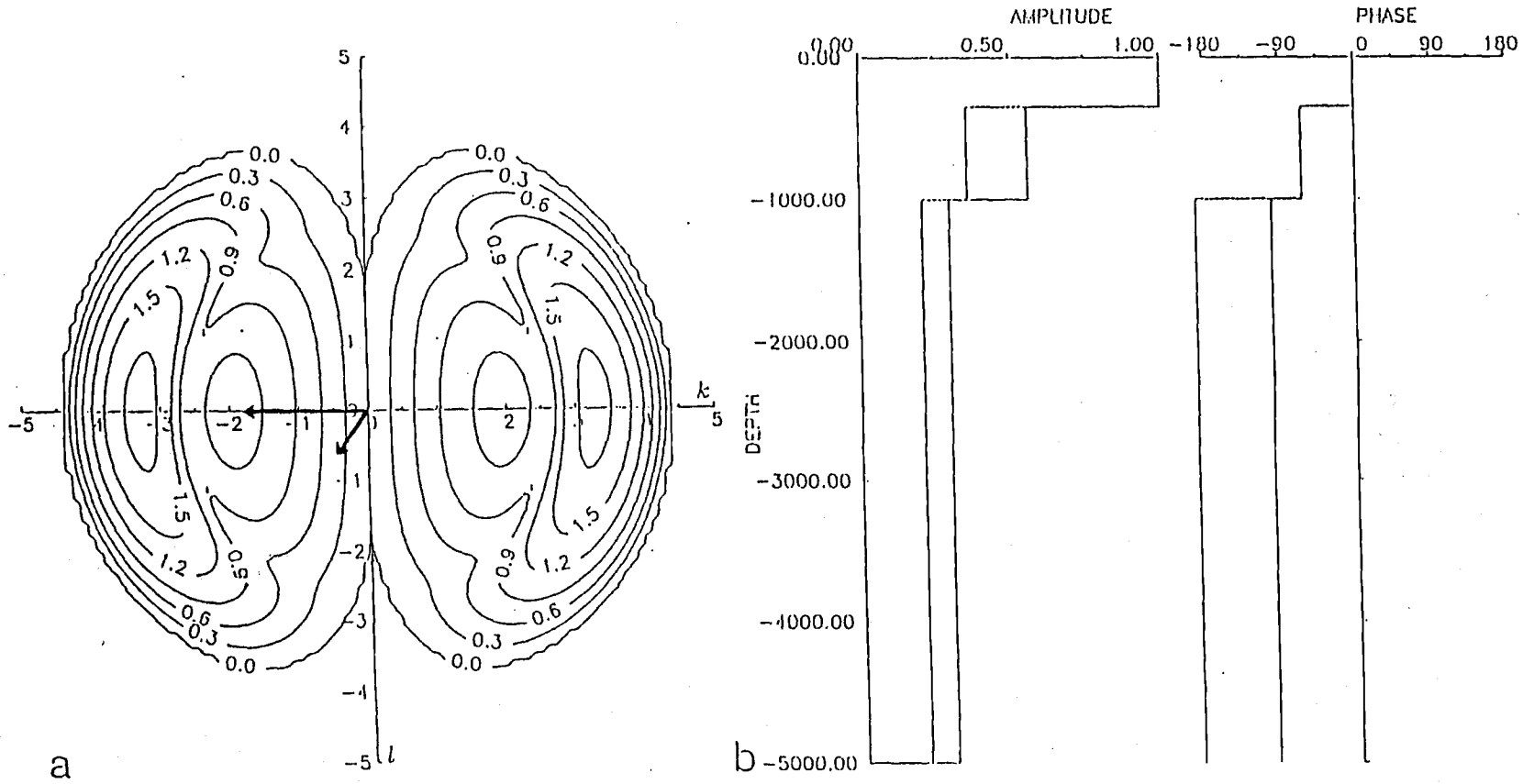

Fig. 28.a. Linear growth rate contours in unit of $10^{-7}s^{-1}$ of the unstable waves at Point S for Experiment II. The finally developed waves are also presented.

Fig. 28.b. Amplitude and phase changes of the first most unstable wave (solid line, the local growth rate maximum in high wave number band) and the second most unstable wave (dotted line, the local growth rate maximum in low wave number band) for Experiment II.

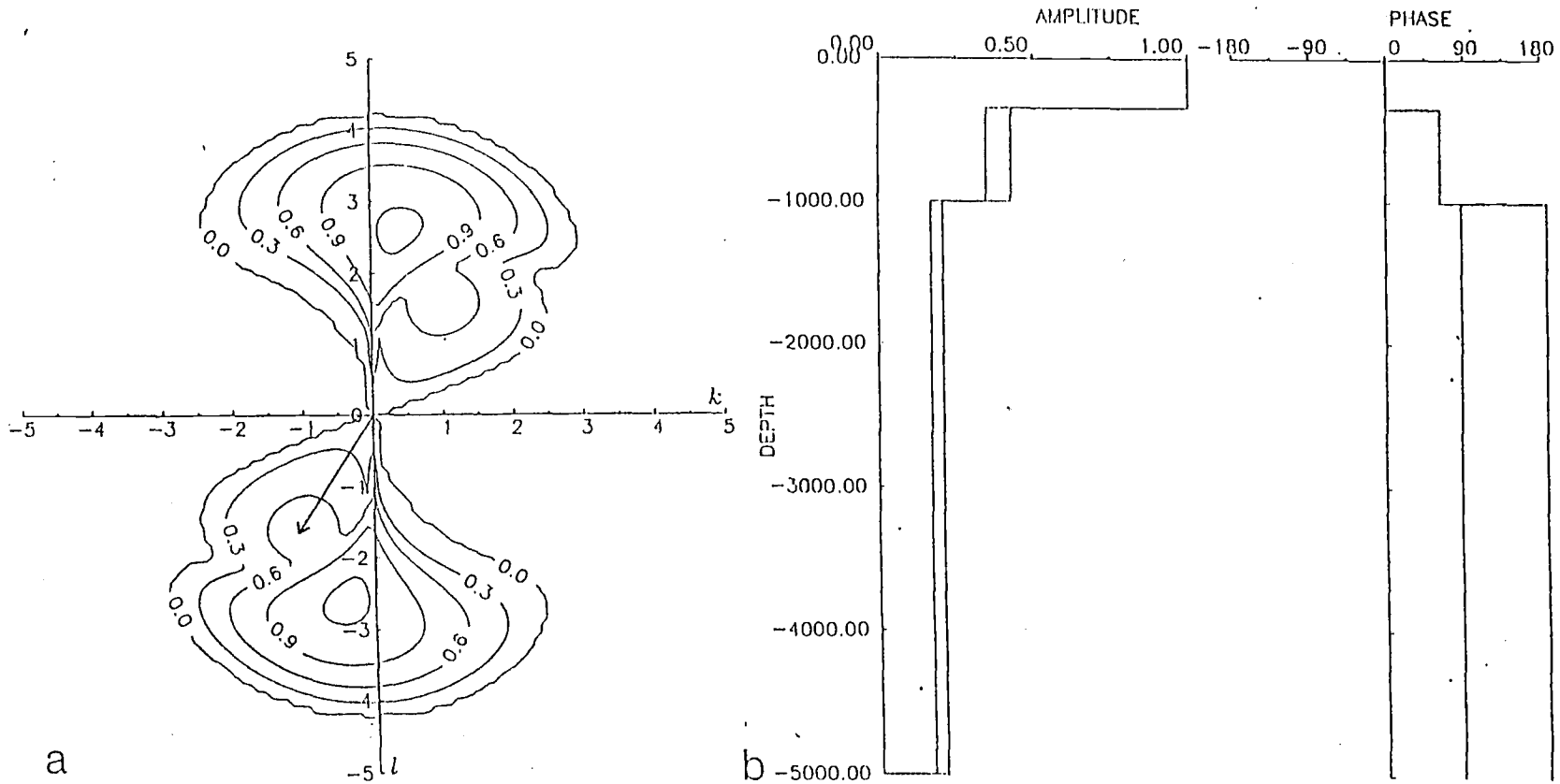

Fig. 29.a. Linear growth rate contours at Point E for Experiment II. The finally developed wave is also presented. The units are the same as Fig. 28.a.

Fig. 29.b. Amplitude and phase changes of the first most unstable wave (solid line) and the second most unstable wave (dotted line) for Experiment II.

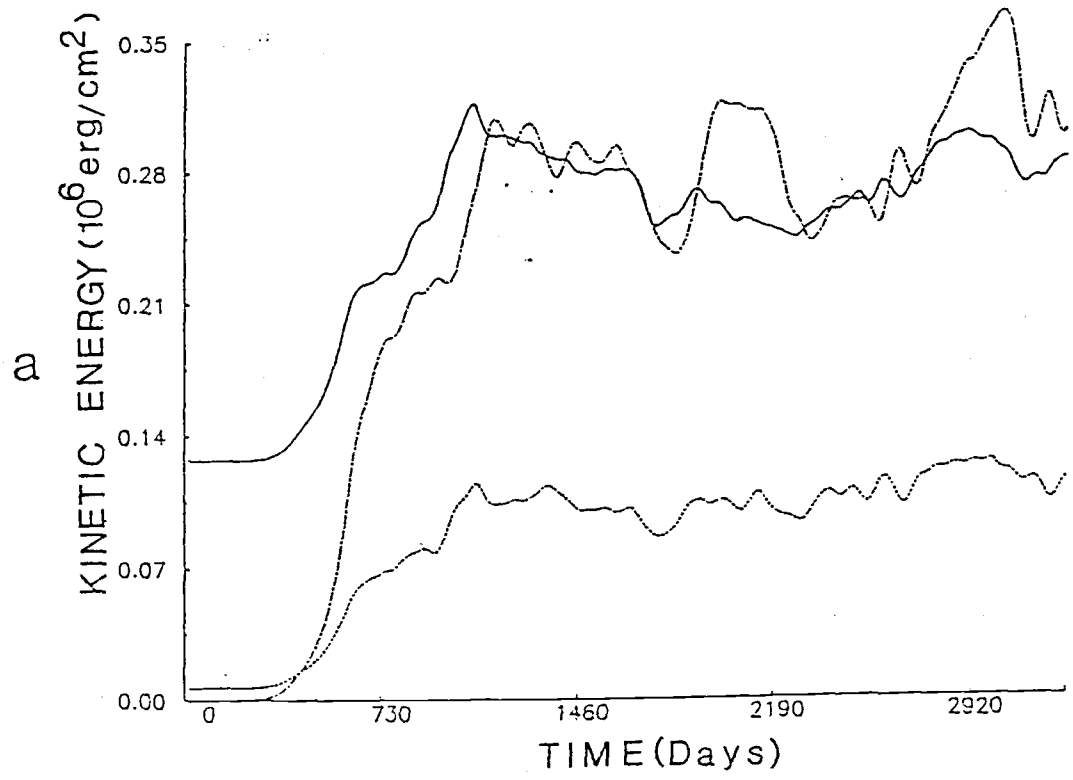

Fig. 30.a. Total kinetic energy per unit area of the surface layer (solid line), the middle layer (dotted line) and the bottom layer (dot-dashed line) as a function of time for Experiment II.

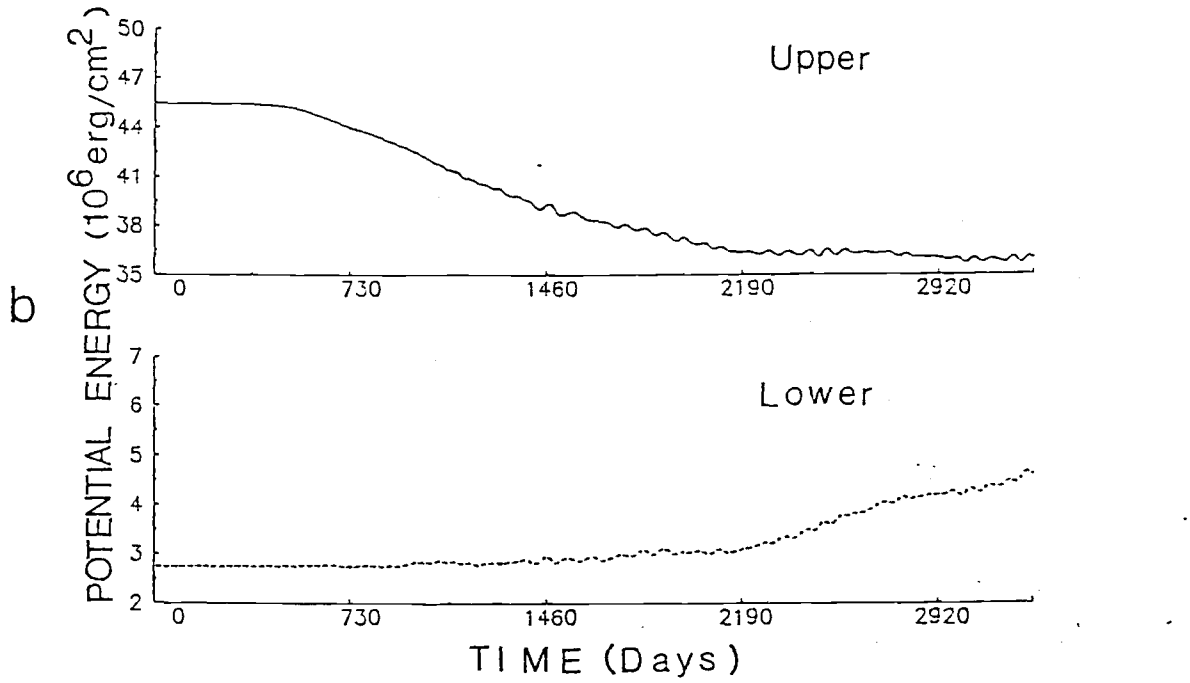

Fig. 30.b. Total potential energy per unit area at the upper interface (solid line) and at the lower interface (dotted line) as a function of time for Experiment II.

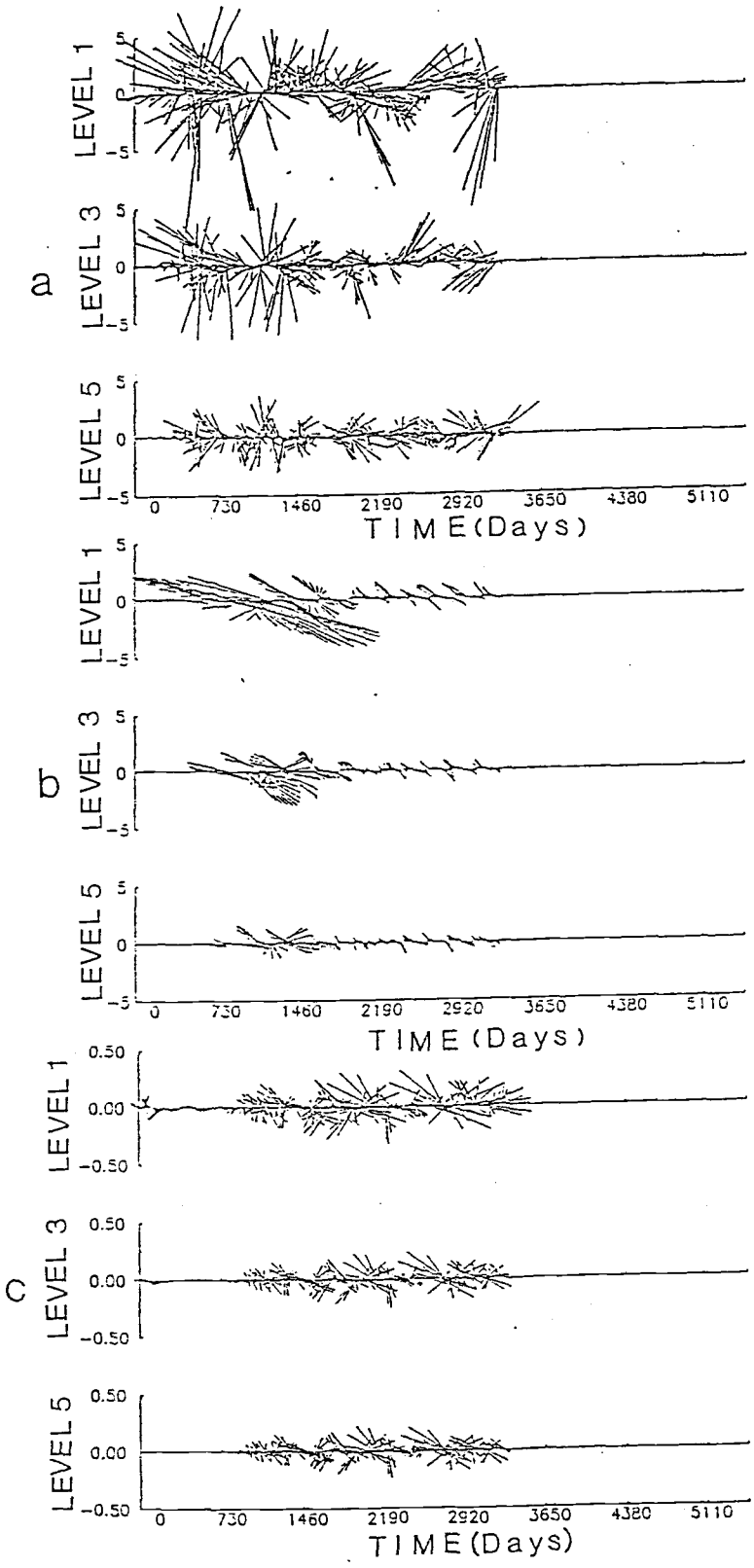

Fig. 31. Stick time plots of eddy currents (a) at Point S, (b) at Point S and (c) at Point N for Experiment II. The y-axes have the unit of cm/s.

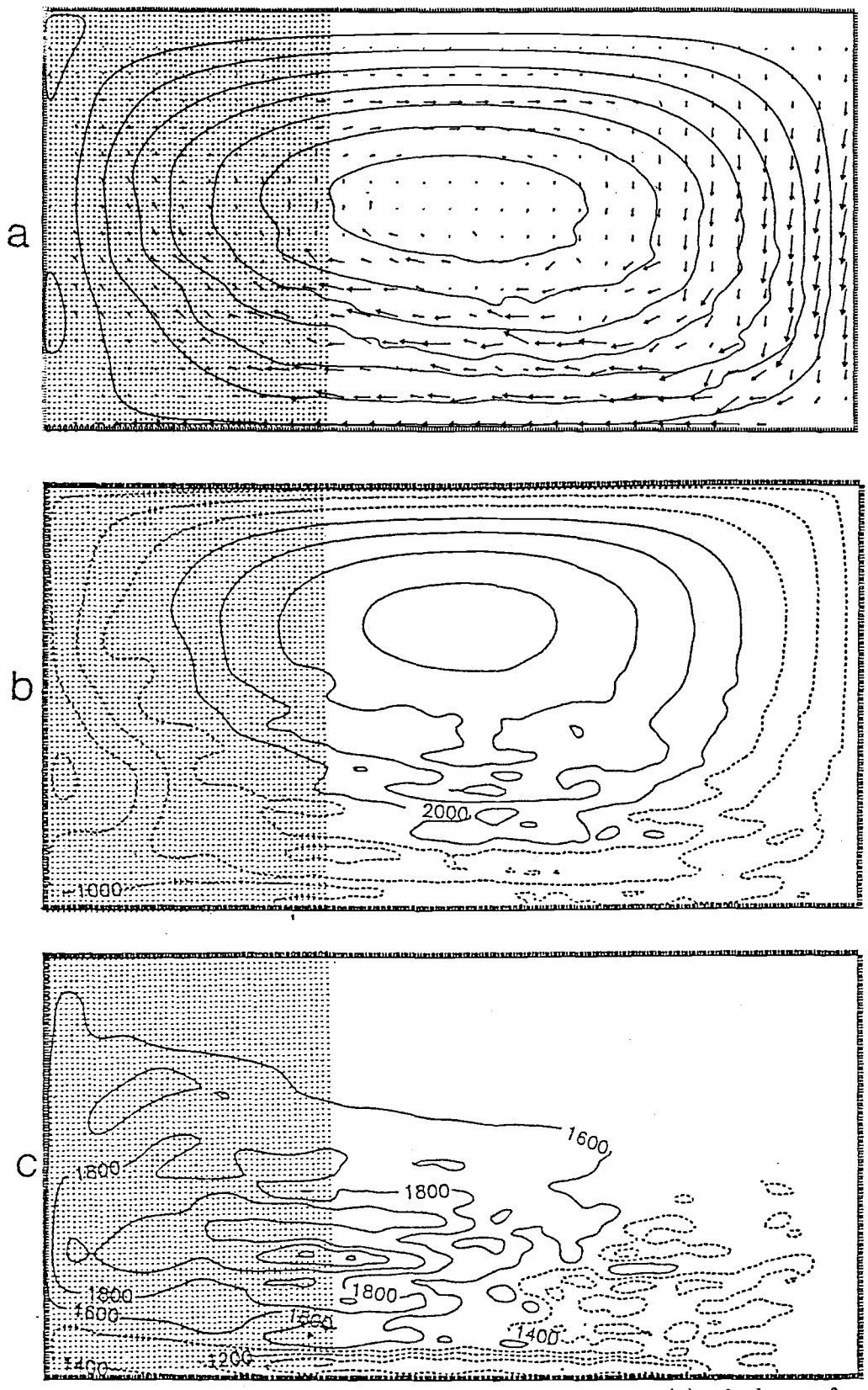

Fig. 32. The mean stream function of the last five years (a) of the surface layer (CI=5000), (b) of the middle layer (CI=1000) and (c) of the bottom layer (CI=200) for Experiment II. The properties of the most unstable waves computed from the mean flow are also shown in (a).

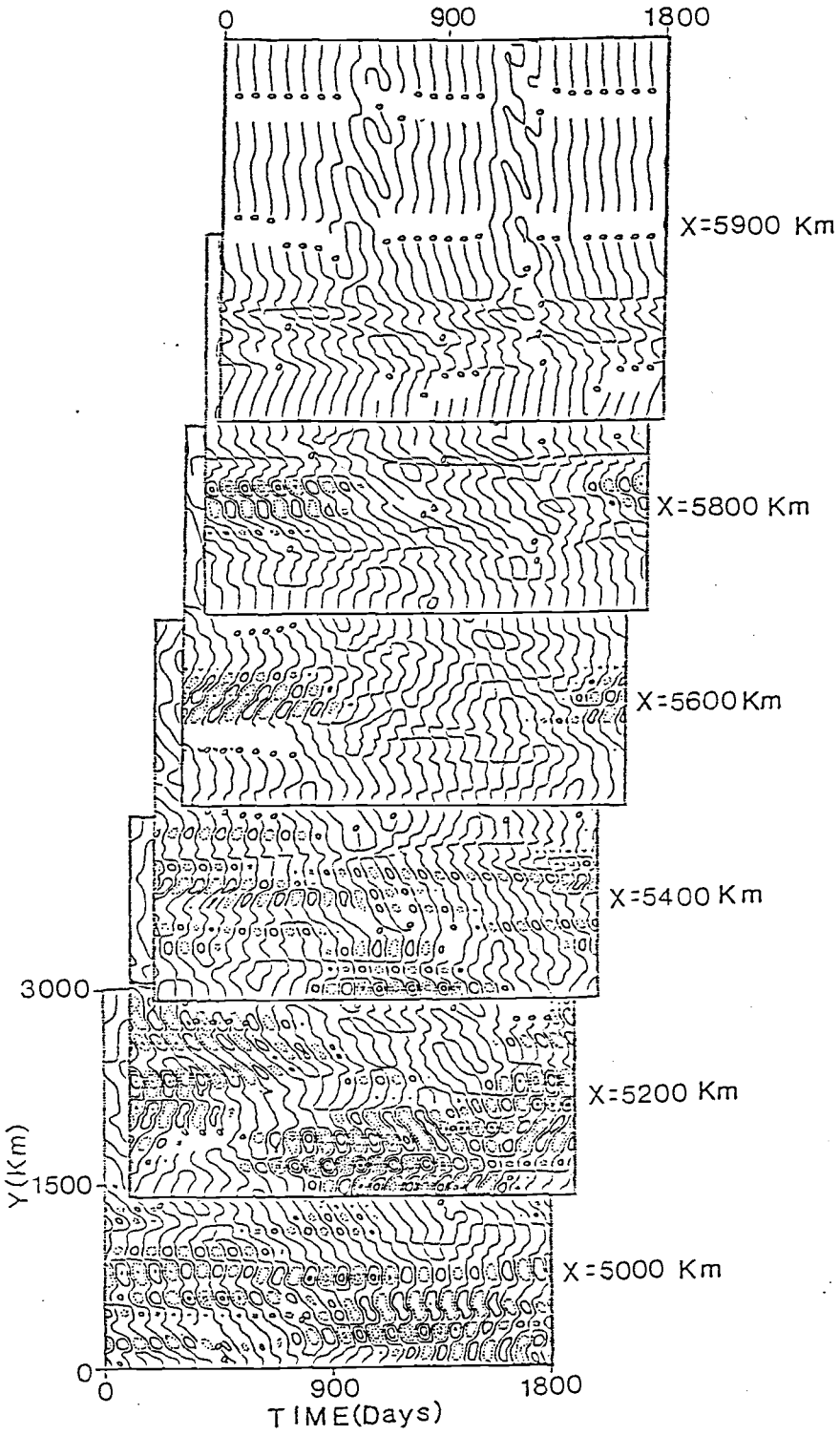

Fig. 33. Progressive phase (y vs time) diagram (CI=1000) for the waves of short periods (105 - 150 days) at various locations along the x-axis for the last five years in Experiment II. Note that all the waves do not propagate southward.

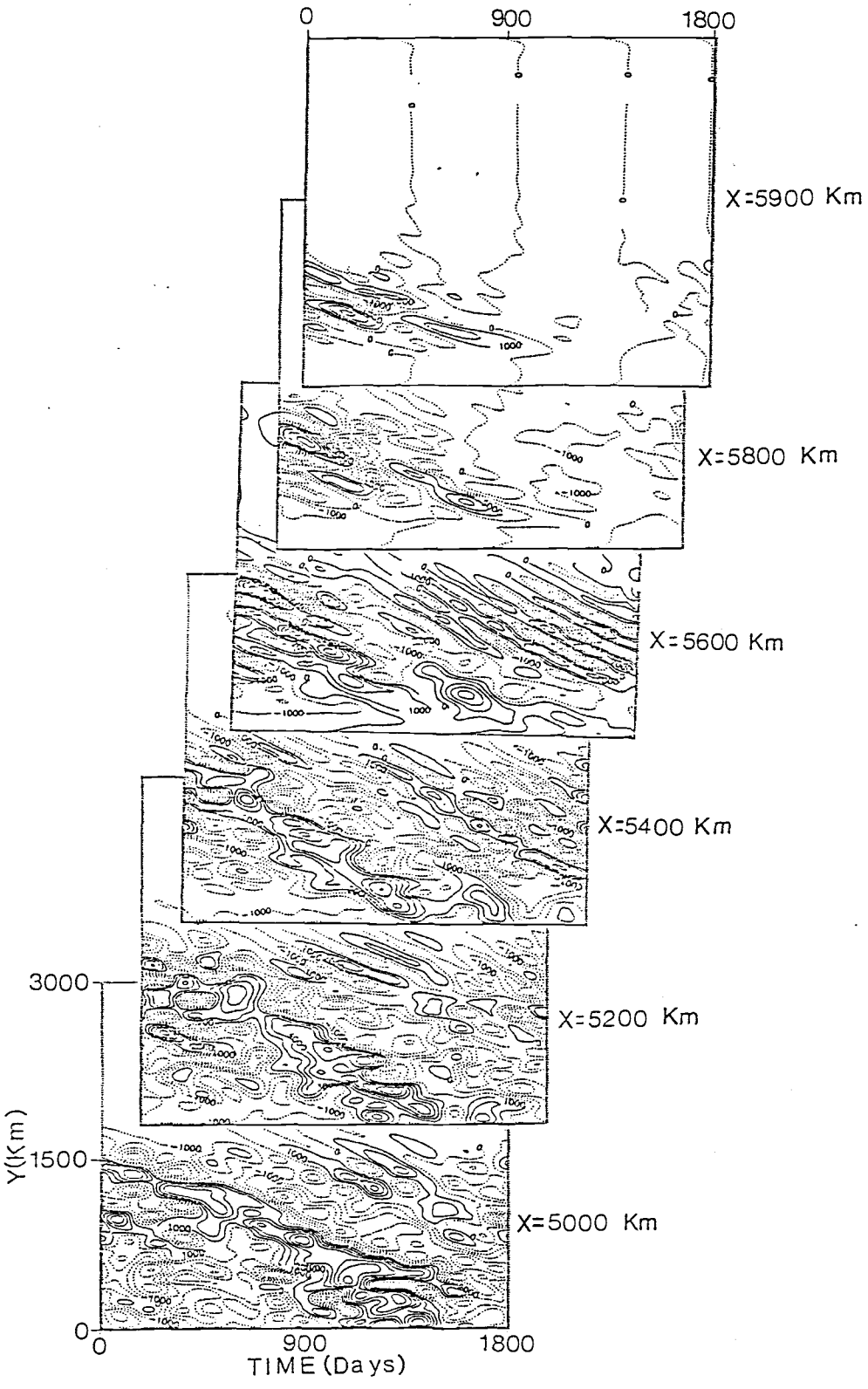

Fig. 34. Progressive phase (y vs time) diagram (CI=1000) for the waves of periods longer than 200 days at various locations along the x-axis for the last five years in Experiment II. Note that the waves propagate southward.

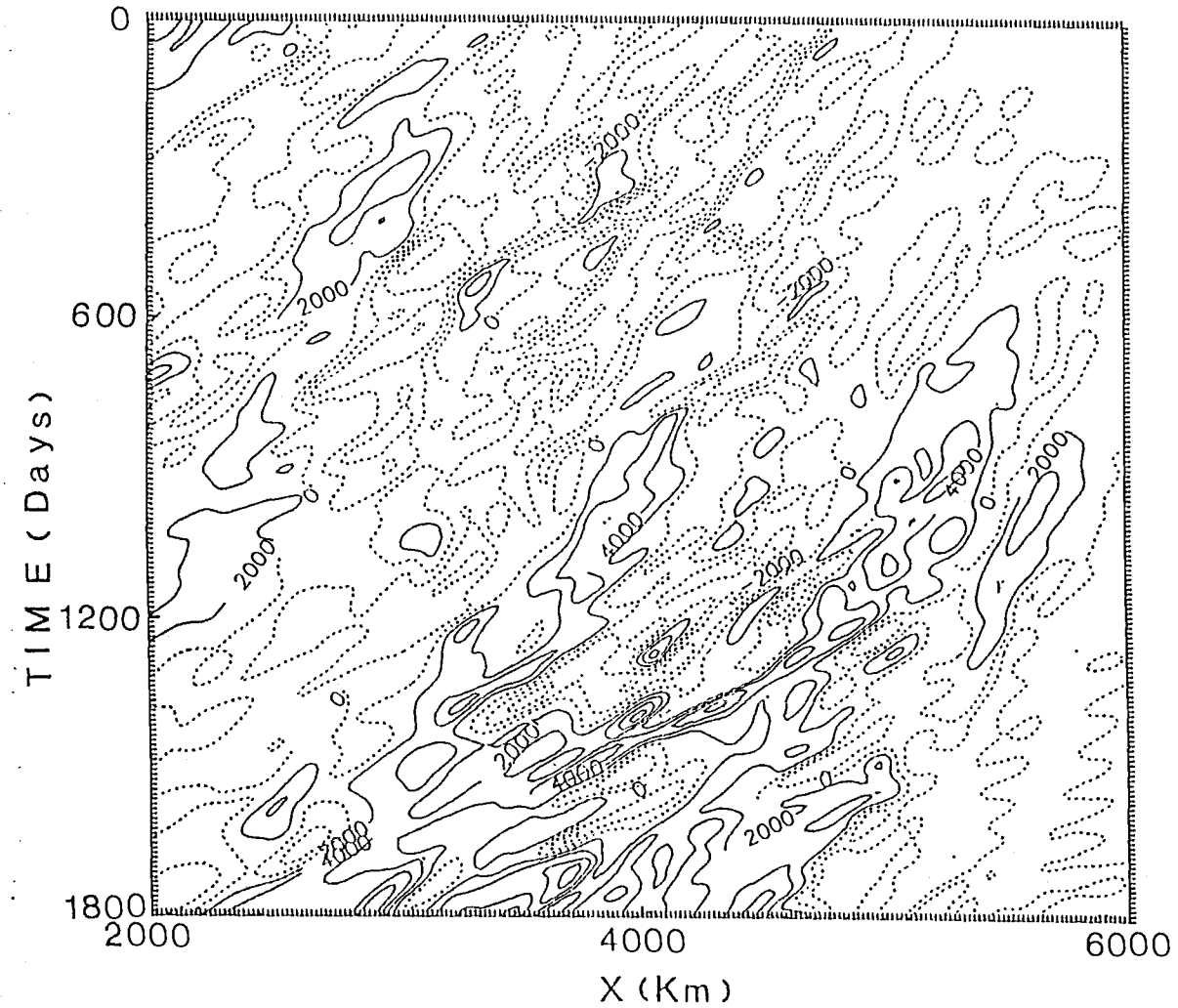

Fig. 35. Phase (x vs time) diagram (CI=2000) at 400 Km from the southern boundary for the last five years in Experiment II. The contours represent the eddy field.

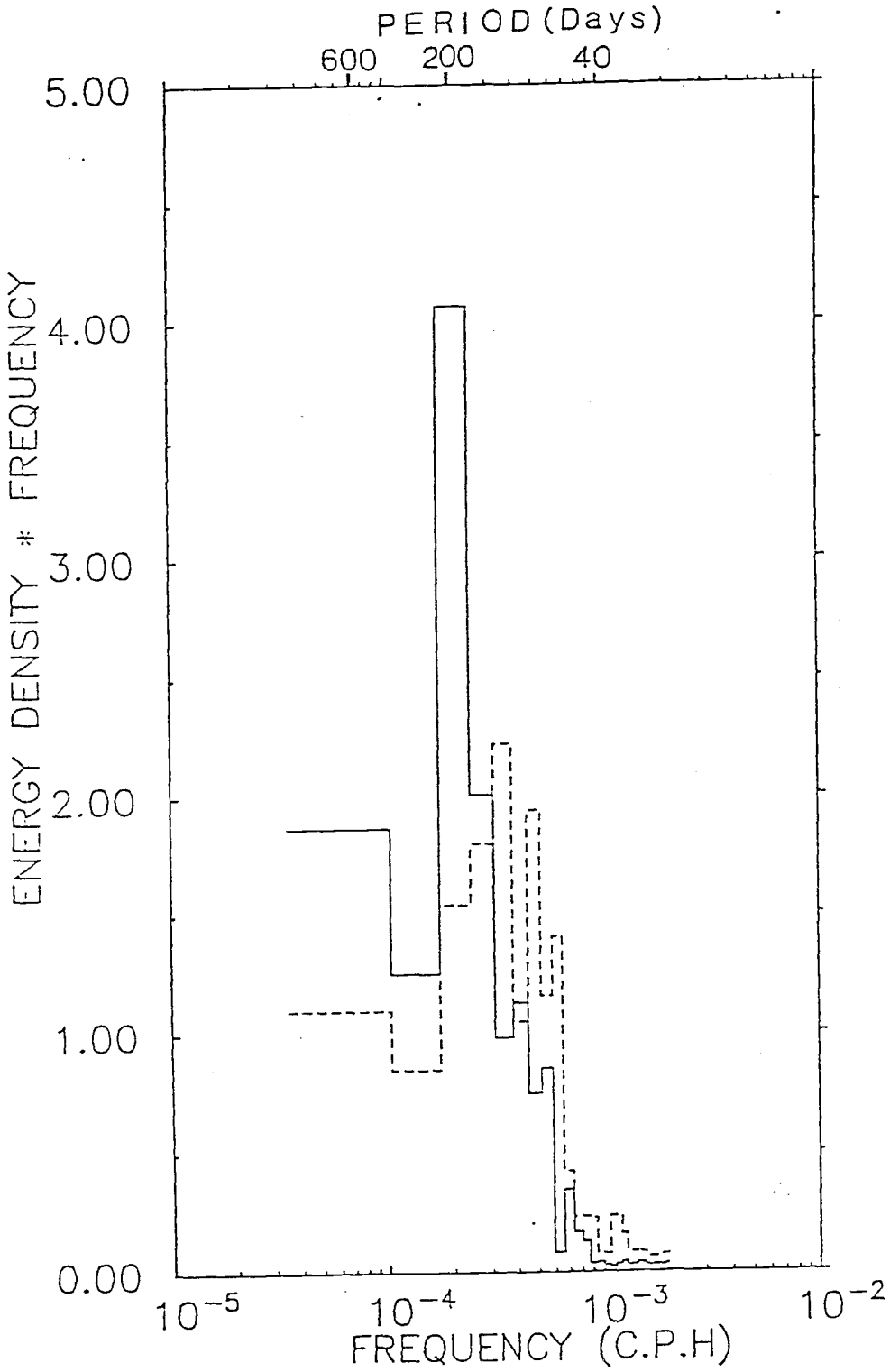

Fig. 36.a. Energy preserving spectra of the surface layer for the east-west component of the current (solid line) and the north-south component (dotted line) at Point S. The units and the notations are the same as Fig. 23.

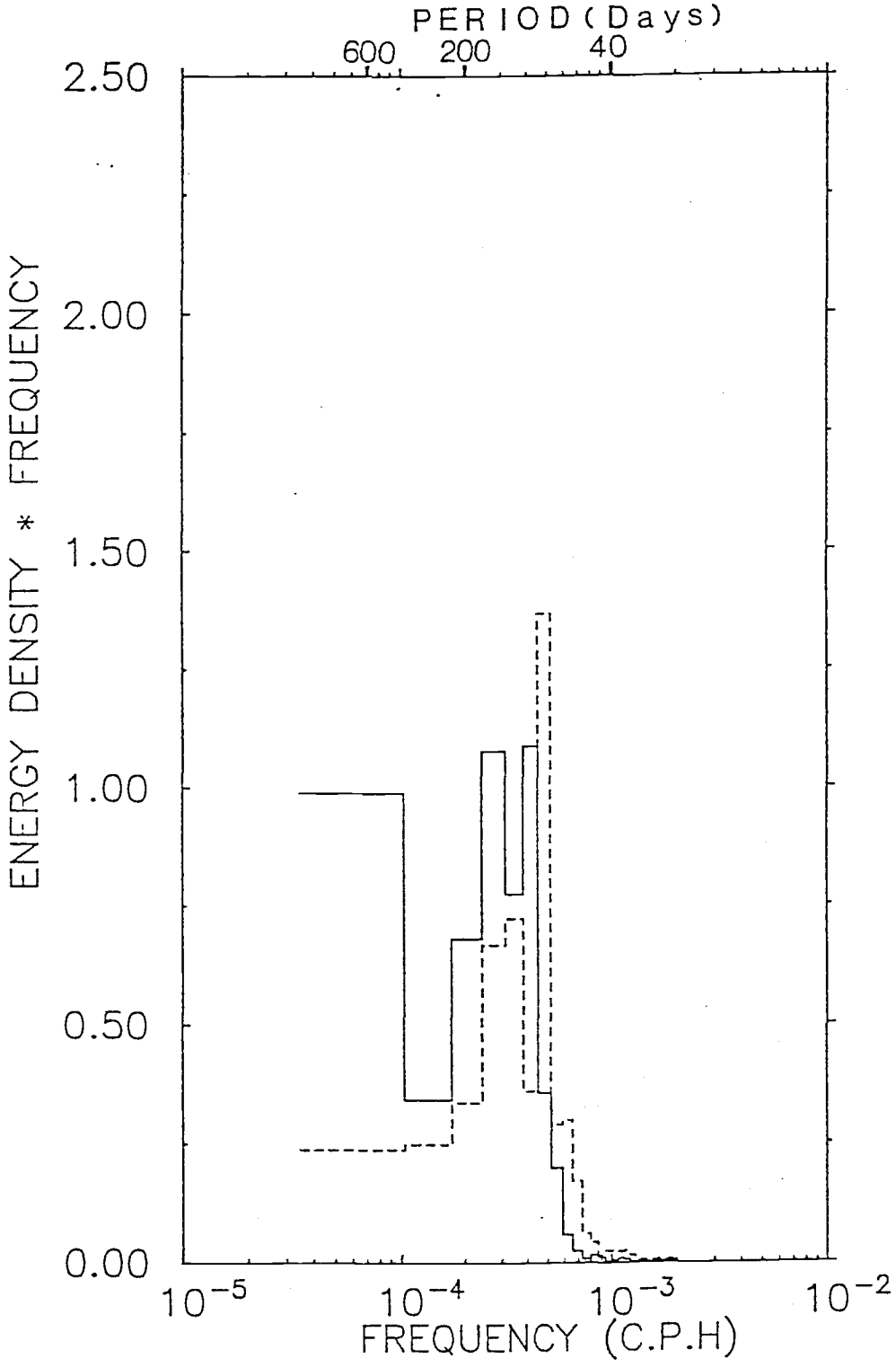

Fig. 36.b. Energy preserving spectra of the middle layer at Point S.

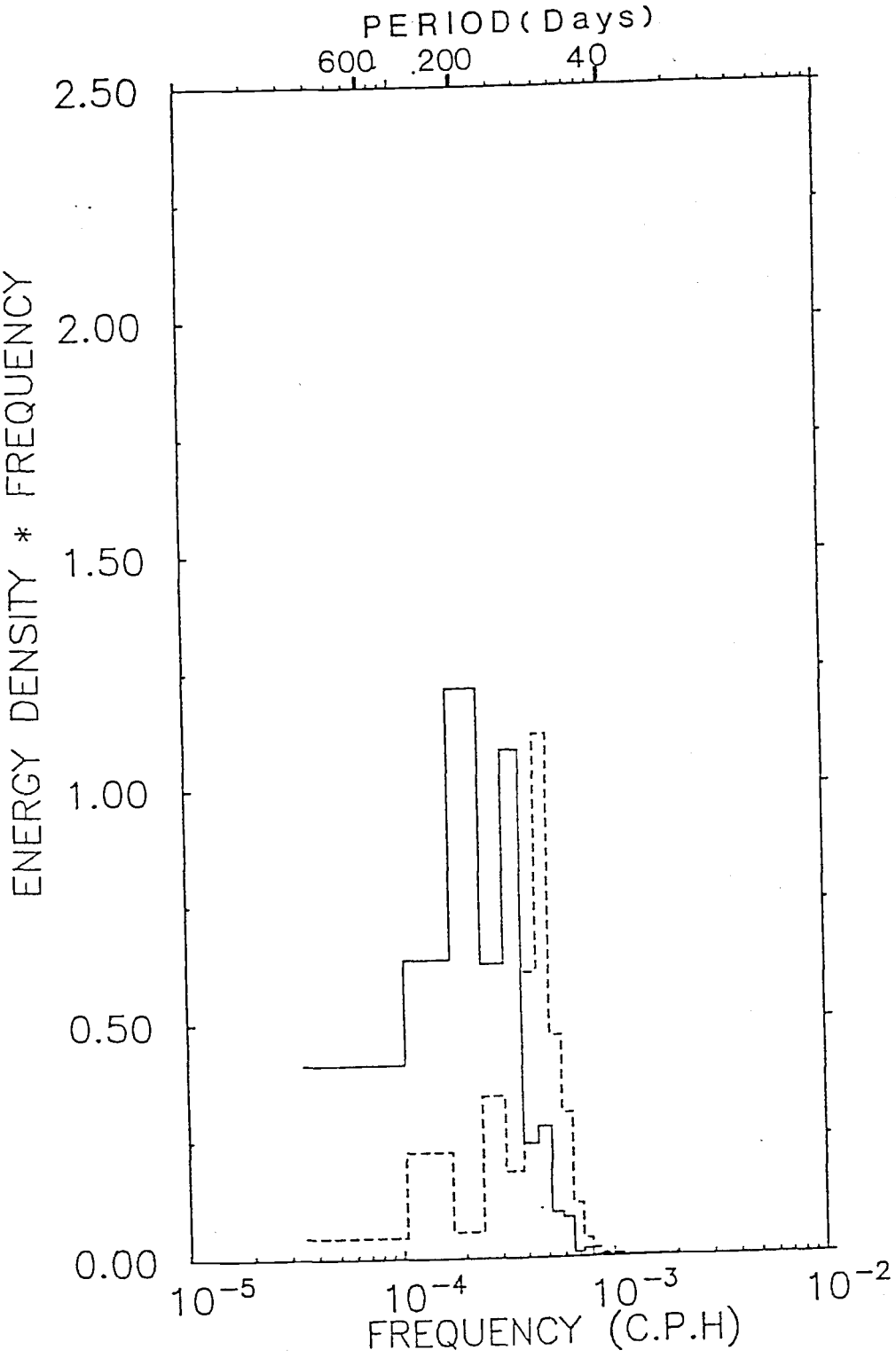

Fig. 36.c. Energy preserving spectra of the bottom layer at Point S.

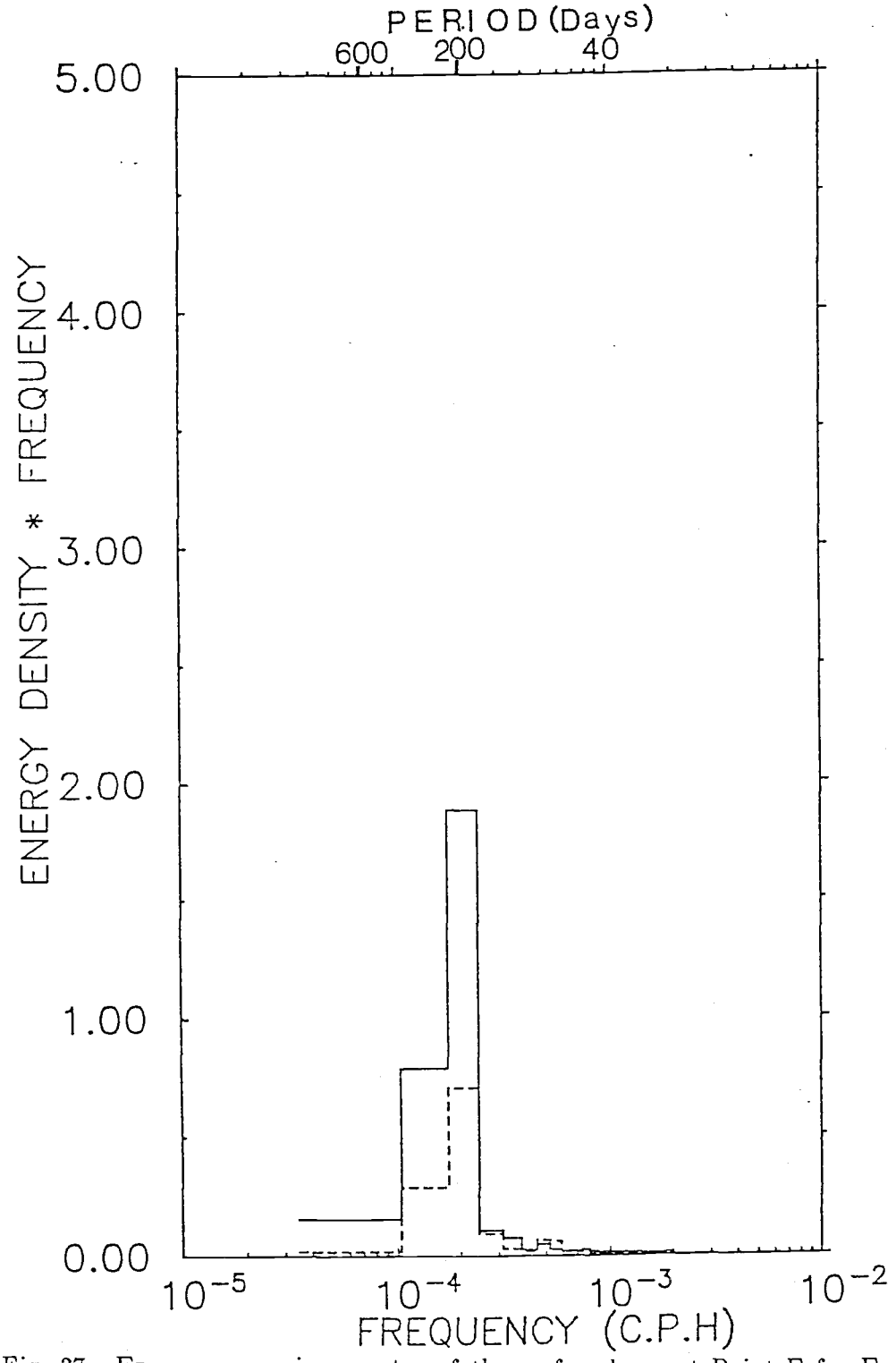

Fig. 37. Energy preserving spectra of the surface layer at Point E for Experiment II. The units and the notations are the same as Fig. 8.

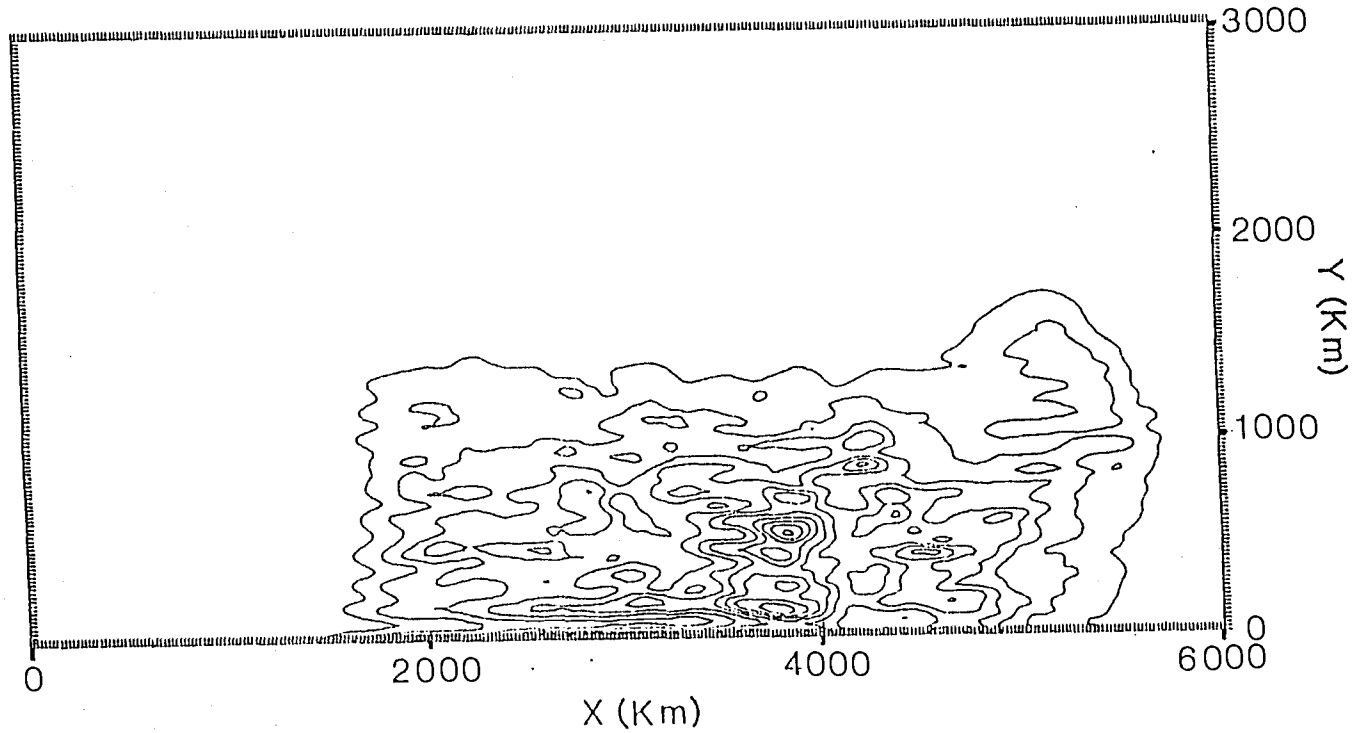

Fig. 38. The eddy kinetic energy per unit area distribution of the bottom layer for the last five years of Experiment II (Cl=0.2 and maximum eddy kinetic energy = 2.0×10^{6} ergs cm^{-2}).

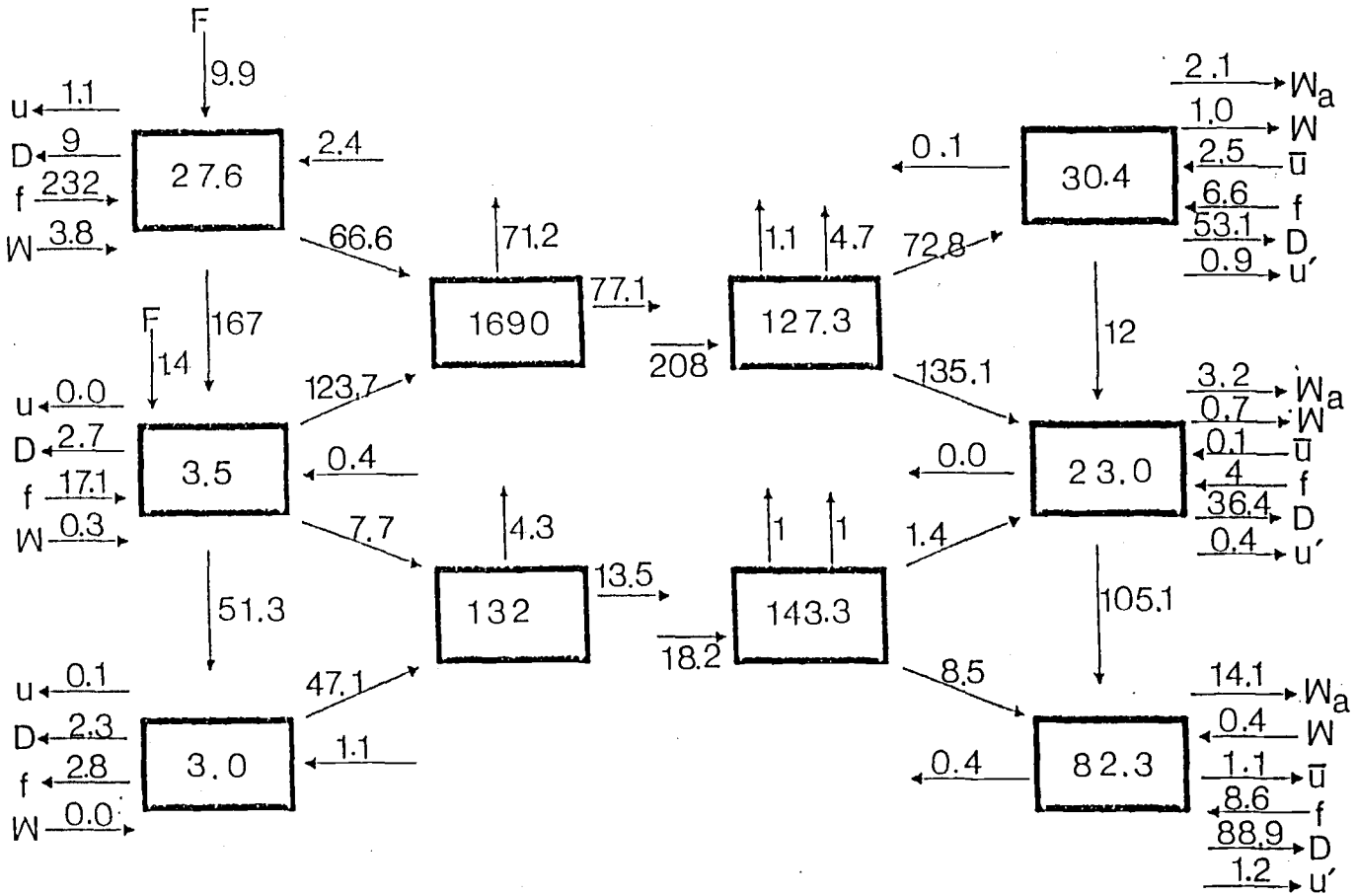

Fig. 39.a. The local energy flux diagram for the southern boundary region. The units and notations are the same as Fig. 27.

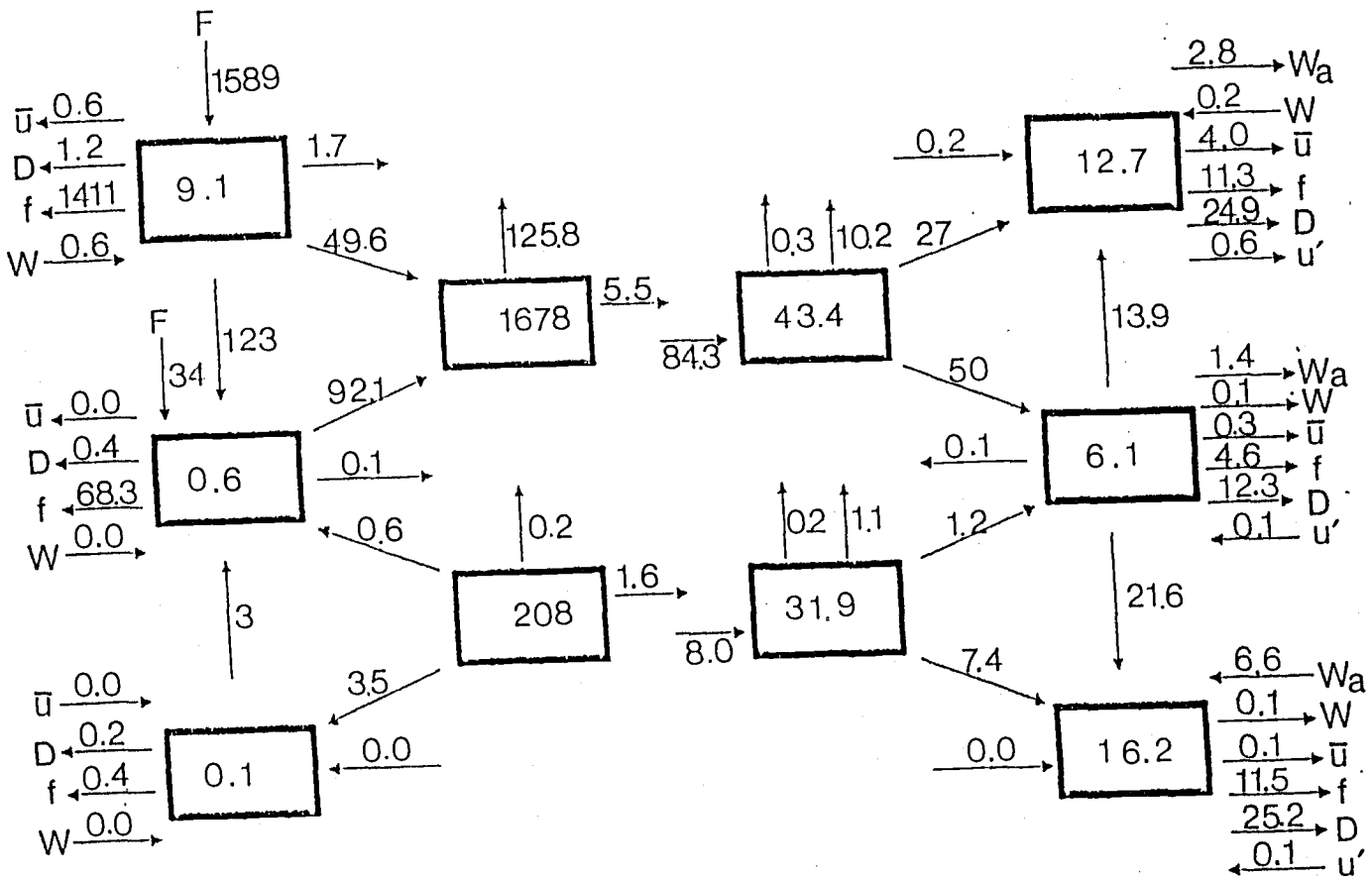

FIg. 39.b. The local energy flux diagram for the eastern boundary region.

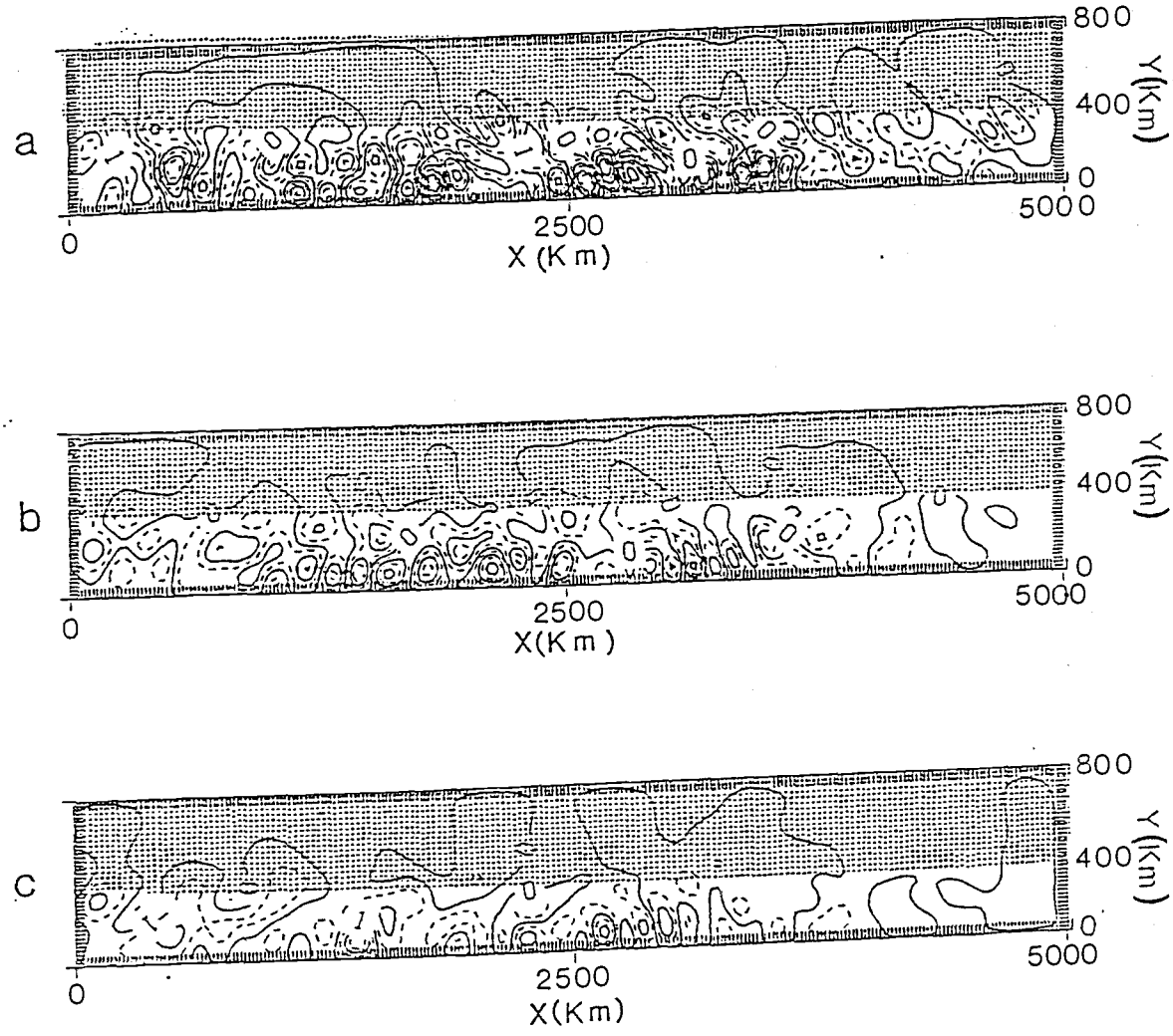

Fig. 40. The instantaneous stream function of the bottom layer (a) in the first year, (b) second year and (c) third year for the east-westward long box experiment (CI=0.5).

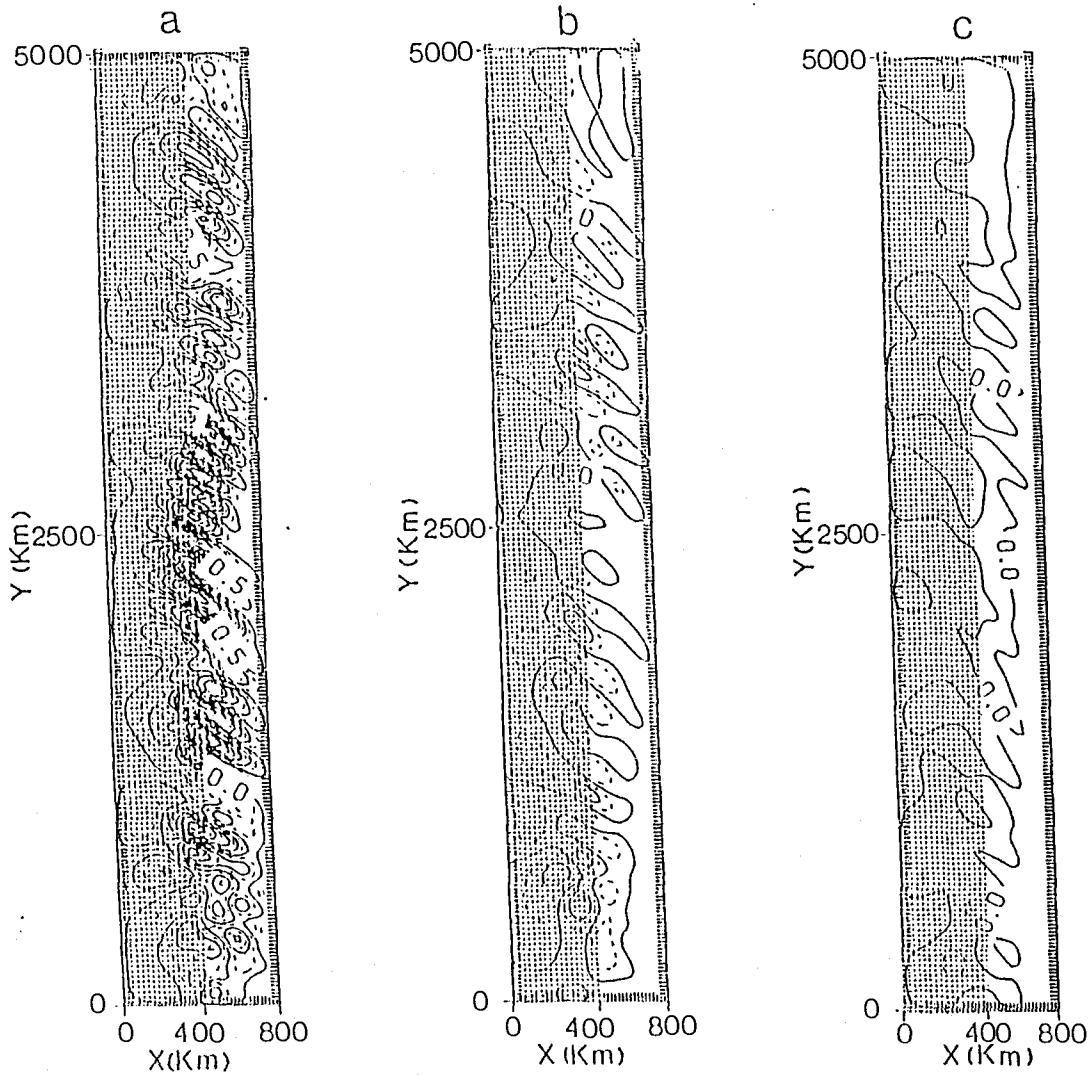

Fig. 41. The instantaneous stream function of the bottom layer (a) in the first year, (b) second year and (c) third year for the north-southward long box experiment (CI=0.3).

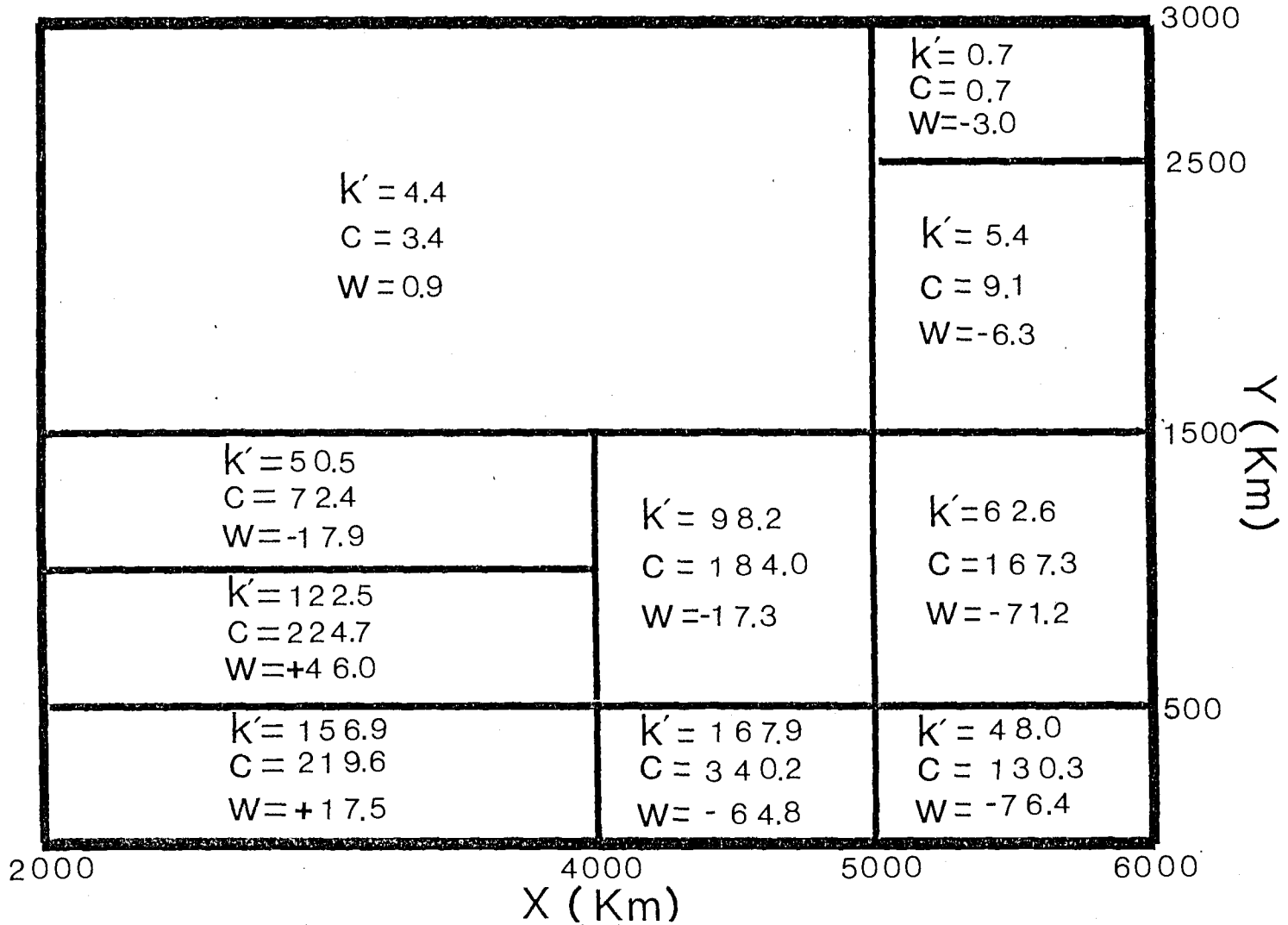

Fig. 42.a. The eddy kinetic energy (K′), the energy conversion from mean to eddy potential energy (C) and the pressure work along the boundary (W). The pressure work term consists of $K_i' \rightarrow W_a$, $K_i' \rightarrow W$ and $K_i' \rightarrow f$ which are expressed in Table 3. The units are the same as in Fig.27.

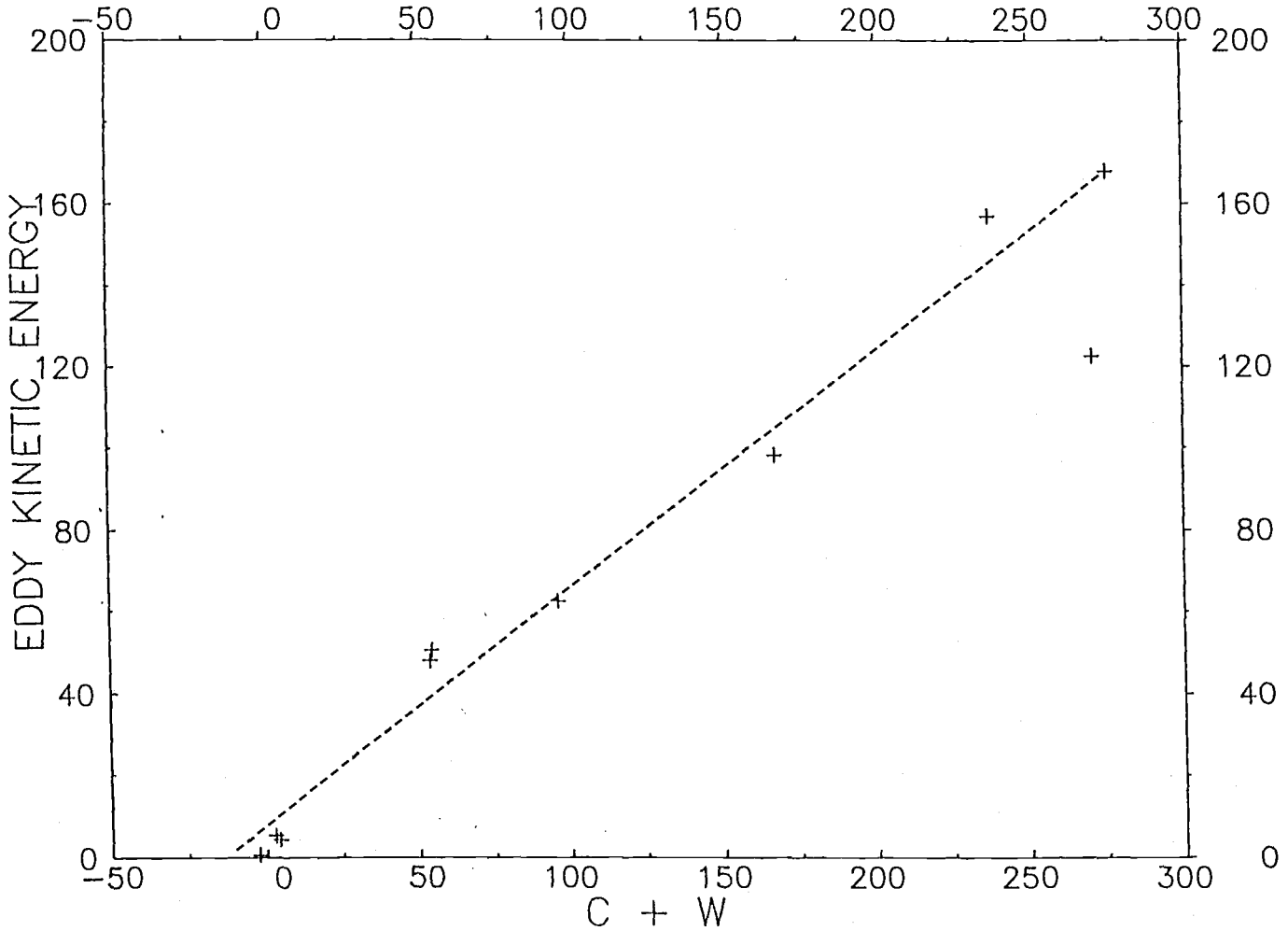

Fig. 42.b. The eddy kinetic energy as a function of net energy production (C + W). The units are the same as in Fig.27.

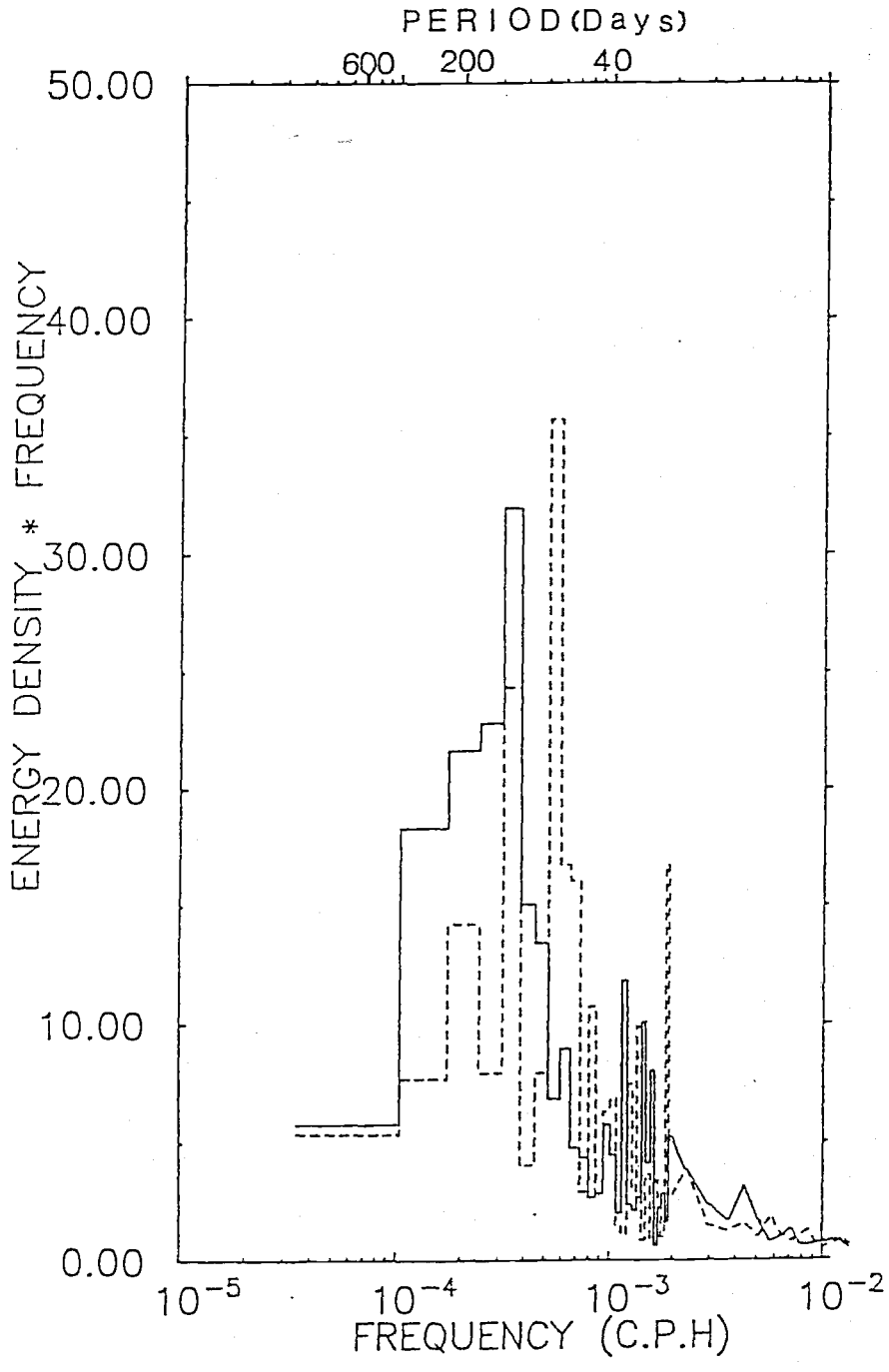

Fig. 43. Energy preserving spectra of eddy kinetic energy at depth of 179 m at 28° N, 152° W from Niiler and Hall (1987). The units and notations are the same as Fig. 23.

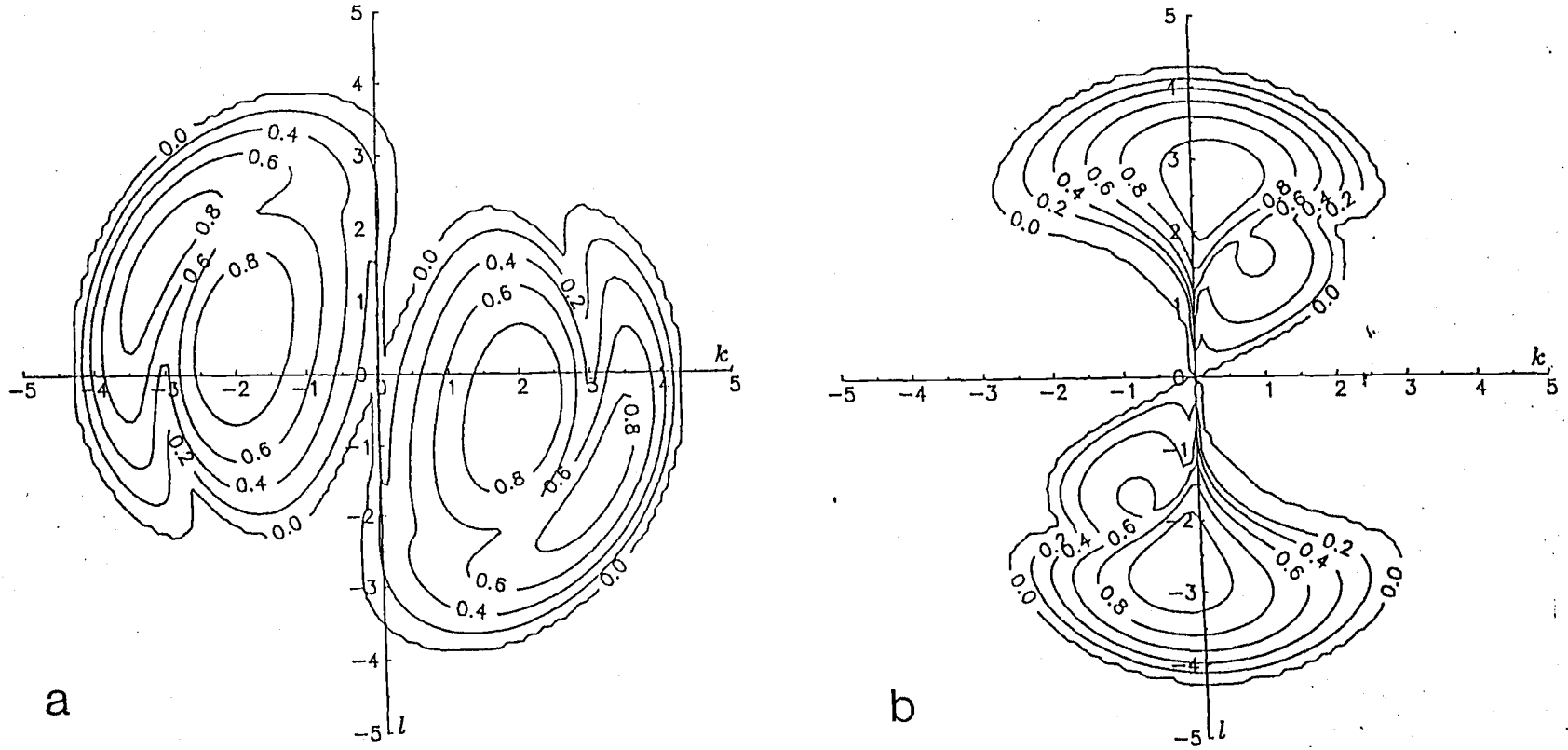

Fig. 44. Linear growth rate contours in unit of 10^{-7} s^{-1} of the unstable waves computed from the mean flow of the final five years (a) at Point S and (b) at Point E.

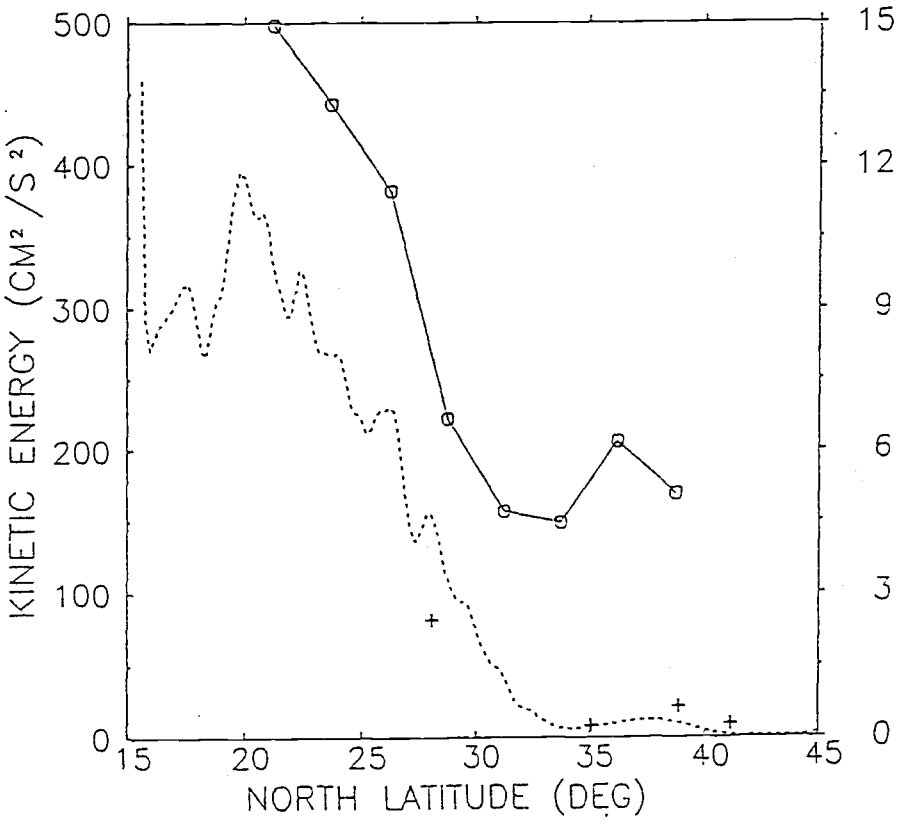

Fig. 45. The observed eddy kinetic energy per unit volume in the Northeast Pacific (130° – 170° W) with the zonally averaged eddy kinetic energy per unit volume from the numerical model as a function of latitude. Crosses are from current meter data at average depth of 179 m along 152°W (Niiler *et al.*, 1987) and solid line with squre is from Niiler and Reynolds (1984) using drifters. These obseved data use left side y axis. Dotted line is from model result and use right side y axis.

BIBLIOGRAPHY

Armi L. and H. Stommel, 1983: Four views of a portion of the North Atlantic subtropical gyre. *J. Phys. Oceanogr.*, **13**, *828-857.*

Barnier, B., 1986: Testing a sponge layer in a two layer quasi-geostrophic model. *Ocean Modelling*, **71**, 9-14. (Unpublished manuscript).

Chapman, D. C., 1985: Numerical treatment of cross-shelf boundaries in a barotropic coastal ocean model. *J. Phys. Oceanogr.*, **15**, 1060-1075.

Cox, M. D., 1985: An eddy resolving numerical model of the ventilated thermocline. *J. Phys. Oceanogr.*, **15**, 1312-1324.

Csanady, G. T., 1982: *Circulation in the coastal ocean.* D. Reidel Pub. Co., Highorn, MA.

Flierl, G. R., 1978: Models of vertical structure and the calibration of two-layer models. *Dyn. Atmos. Oceans*, **2**, 341-381.

Fu, L.-L., T. Keffer, P. P. Niiler and C. Wunsch, 1982: Observations of mesoscale variability in the western North Atalantic: A comparative study. *J. Mar. Res.*, **40**, 809-848.

Gill, A. E., J. S. Green and A. J. Simmons, 1974: Energy partition in the large-scale ocean circulation and the production of mid-ocean eddies. *Deep Sea Res.*, **21**, 499-528.

Haidvogel D. B. and W. R. Holland, 1978: The stability of ocean currents in eddy-resolving general circulation models. *J. Phys. Oceanogr.*, **8**, 393-413.

Hall, M. M., 1986: A diagnostic investigation of kinetic energy budgets in a numerical model. *J. Geophys. Res.*, **91**, 2555-2568.

Harrison, D. E. and A. J. Semtner, Jr., 1986: On the generation of deep mean flows: Some numerical experiments. *J. Geophys. Res.*, **91**, 2569-2573.

Holland, W. R., 1978: The role of mesoscale eddies in the general circulation of the ocean : Numerical experiments using a wind-driven quasi-geostrophic method. *J. Phys. Oceanogr.*,**8**, 363-392.

Holland, W. R. and D. B. Haidvogel, 1980: A parameter study of the mixed instability of idealized ocean currents. *Dyn. Atmos. Oceans.*,**4**, 185-215.

Holland, W. R. and L. B. Lin, 1975: On the origin of mesoscale eddies and their contribution to the general circulation of the ocean. I. A preliminary numerical experiment. *J. Phys. Oceanogr.*, **5**, 642-657.

Kang, Y. Q., L. Magaard, 1979: Stable and unstable Rossby waves in the North Pacific current as inferred from the mean stratification. *Dyn. Atmos. Oceans*, **3**, 1-14.

Kang, Y. Q., J. M. Price and L. Magaard, 1982: On stable and unstable Rossby waves in non-zonal oceanic shear flow. *J. Phys. Oceanogr.*, **12**, 528-537.

Keffer, T. and P. P. Niiler, 1982: Eddy convergence of heat, salt, density, and vorticity in the subtropical North Atlantic. *Deep-Sea Research*, **29**, 201-216.

Lee, D.-K. and P. P. Niiler, 1987: The local baroclinic instability of geostrophic spirals in the eastern North Pacific. *J. Phys. Oceanogr.* (In printing).

McNally, G. J., W. C. Patzert, A. D. Kirwan, Jr. and A. C. Vastano, 1983: The mean-surface circulation of the North Pacific using satellite tracked drifting buoys. *J. Geophys. Res.*, **88**, 7507-7518.

McWilliams, J. C., W. R. Holland and J. H.S. Chow, 1978: A description of numerical Antarctic Circumpolar Currents. *Dyn. Atmos. Oceans*, **2**, 213-291.

Niiler, P. P. and M. M. Hall, 1987: Low frequency eddy variability in the eastern North Pacific subtropical gyre. (In preparation).

Niiler, P. P., M. M. Hall and W. J. Schmitz, 1987: Long-term current meter measurements along 152°W in the North Pacific. (In preparation).

Niiler, P. P. and R. W. Reynolds, 1984: The three-dimensional circulation near the eastern North Pacific subtropical front. *J. Phys. Oceanogr.*, **14**, 217-230.

Orlanski, I., 1976: A simple boundary condition for unbounded hyperbolic conditions. *J. Comput. Phys.*, **21**, 251-269.

Pedlosky, J., 1979: *Geophysical Fluid Dynamics.* Springer-Verlag, New York.

Pinardi N. and A. R. Robinson, 1986: Quasigeostrophic energetics of open ocean regions. *Dyn. Atmos. Oceans,* **10**, 185-219.

Rhines, P. B., 1977: The dynamics of unsteady currents. *The Sea.* **6**, 189-318.

Robinson, A. R., D. E. Harrison, Y. Mintz and A. J. Semtner, 1977: Eddies and the general circulation of an idealized oceanic gyre: A wind and thermally driven primitive equation numerical experiment. *J. Phys. Oceanogr.*, **7**, 208-230.

Robinson, A. R. and J. C. McWilliams, 1974: The baroclinic instability of the open ocean. *J. Phys. Oceanogr.*, **4**, 281-294.

Schulman, E. E., 1967: The baroclinic instability of a mid-ocean circulation. *Tellus*, **19**, 292-305.

Schmitz, W. J. and W. Holland, 1982: A preliminary comparison of selected numerical eddy-resolving general circulation experiments with observations. *J. Mar. Res.*, **40**, 75-117.

Tennekes, J. and J. L. Lumley, 1972: *A First Course in Turbulence.* The MIT Press.